Investigation of Modulation Methods to Synthesize High Performance Resonator-Based RF MEMS Components

Submitted in partial fulfillment of the requirements for
the degree of
Doctor of Philosophy

in

Electrical and Computer Engineering

Changting Xu

B.E., Precision Instruments, Tsinghua University (2013)
M.S., Electrical and Electronics Engineering, Carnegie Mellon University (2017)

Carnegie Mellon University
Pittsburgh, PA

February, 2018

ABSTRACT

The growing demand for wireless communication systems is driving the integration of radio frequency (RF) front-ends on the same chip with multi-band functionality and higher spectral efficiency. Microelectromechanical systems (MEMS) have an overarching applicability to RF communications and are critical components in facilitating this integration process. Among a variety of RF MEMS devices, piezoelectric MEMS resonators have sparked significant research and commercial interest for use in oscillators, filters, and duplexers. Compared to their bulky quartz crystal and surface acoustic wave (SAW) counterparts, MEMS resonators exhibit impressive advantages of compact size, lower production cost, lower power consumption, and higher level of integration with CMOS fabrication processes. One of the promising piezoelectric MEMS resonator technologies is the aluminum nitride (AlN) contour mode resonator (CMR). On one hand, AlN is chemically stable and offers superior acoustic properties such as large stiffness and low loss. Furthermore, CMRs offer low motional resistance over a broad range of frequencies (few MHZ to GHz), which are lithographically-definable on the same silicon substrates. To date, RF MEMS resonators (include CMRs) have been extensively studied; however, one aspect that was not thoroughly investigated is how to modulate/tune their equivalent parameters to enhance their performance in oscillators and duplexers.

The goal of this thesis is to investigate various modulation methods to improve the thermal stability of the resonator, its "effective" quality factor when used in an oscillator, and build completely novel non-reciprocal components. Broadly defined, modulation refers to the exertion of a modifying or controlling influence on something, herein specifically, the resonator admittance. In this thesis, three categories of modulation methods are investigated: thermal modulation, force modulation, and external electronic modulation.

Firstly, the AlN CMR's center frequency can be tunned by the applied thermal power to the resonator body. The resonator temperature is kept constant (for example, 90 ℃) via a temperature

sensor and feedback control such that the center frequency is stable over the whole operation temperature range of interest (e.g. –35 to 85 ℃). The maximum power consumption to sustain the maximum temperature difference (120 ℃ in this thesis) between resonator and ambient is reduced to a value as low as 353 μW – the lowest ever reported for any MEMS device. These results were attained while simultaneously maintaining a high quality factor (up to 4450 at 220 MHz device). The feedback control was implemented by either analog circuits or via a microprocessor. The analog feedback control, which innovatively utilized a dummy resistor to compensate for temperature gradients, resulted in a total power consumption of 3.8 mW and a frequency stability of 100 ppm over 120 ℃. As for the digital compensation, artificial neural network algorithm was employed to facilitate faster calibration of look-up tables for multiple frequencies. This method attained a frequency stability of 14 ppm over 120 ℃.

The second modulation method explored in this thesis is based on the use of an effective external force to enhance the 3-dB quality factor of AlN CMRs and improve the phase noise performance of resonator-based oscillators. The force modulation method was embodied in a two-port device, where one of the two ports is used as a one-port resonator and the other is driven by an external signal to effectively apply an external force to the first port. Through this technique, the quality factor of the resonator was boosted by 140 times (up to 150,000) and the phase noise of the corresponding oscillator realized using the resonator was reduced by 10 dBc/Hz.

Lastly, a novel magnetic-free electrical circulator topology that facilitates the development of in-band full duplexers (IBFD) for simultaneous transmit and receive (STAR) is proposed and modeled. Fundamentally, a linear time-invariant (LTI) filter network parametrically modulated via a switching matrix is used to break the reciprocity of the filter. The developed model accurately predicts the circulator behavior and shows very good agreement with the experimental results for a 21.4 MHz circulators built with MiniCircuit filter and switch components. Furthermore, a high frequency (1.1 GHz) circulator was synthesized based on AlN MEMS bandpass filters and CMOS RF switches, hence showing a compact approach that can be used in handheld devices. The modulation frequency and duty cycle are optimized so that the circulator can provide up to 15 dB of isolation over the filter bandwidth while good power transfer between the other two ports is maintained. The demonstrated device is expected to intrinsically offer low noise and high linearity.

The combination of the first two modulation methods facilitates the implementation of monolithic, temperature-stable, ultra-low noise, multi-frequency oscillator banks. The third modulation technique that was investigated sets the path for the development of CMOS-compatible in-band full duplexers for simultaneous transmit and receive and thus facilitates the efficient utilization of the electromagnetic spectrum. With the aid of all these three modulation approaches, the author believes that a fully integrated, multi-frequency, spectrum-efficient transceiver is enabled for next-generation wireless communications.

To my parents

ACKNOWLEDGEMENTS

First and foremost, I would like to express my sincere gratitude to my advisor, Prof. Gianluca Piazza, for his professional guidance, heartfelt encouragement, and continued support throughout the 4.5 years of my Ph.D. degree. Before I started as a Ph.D. student, I anticipated that a typical advisor only provided financial support and rough guidance, but left all technical details for his/her students. However, my advisor amazes me by his broad knowledge of MEMS and great passion about research. He is also brilliant at the penetration into the nature of the problems and challenges. Moreover, he shows full respect to his students and encouraged me when my research didn’t go well. More importantly, he is flexible and open-minded so that he gave me enough freedom to try out seemingly insane ideas. Last, I always admire his magic power to explain new concepts with a few words, and I had learned many presentation and writing skills from him via his patient and exhaustive edits of my slides and papers.

I would also like to thank Prof. Rick Carley, Prof. Tamal Mukherjee, and Prof. Songbin Gong, who agreed to be my Ph.D. thesis committee members and spent their precious time on attending my thesis defense, reviewing this thesis, and providing me with their valuable technical and professional feedback. Special thanks go to Prof. Songbin Gong, who flew from Champaign to Pittsburgh to be personally present at my defense.

I am also thankful to my previous and current labmates, colleagues, and friends for their assistance in my work and companion in my life: Abhay Kochhar, Ashraf Mahmoud, Abhishek Sharma, Cristian Casella, Zhuo Chen, Emad Mehdizadeh, Erdinc Tatar, Gabriel Vidal Alvarez, Hoe Joon Kim, James Best, Jitendra Pal, Jinglin Xu, Lutong Cai, Lisha Shi, Mary Beth Galanko, Metin Guney, Mohamed Mahmoud, Min Xu, Nicolo Oliva, Nancy Saldanha, Pietro Simeoni, Senbo Fu, Shaolong Liu, Suresh Santhanam, Sean Yen, Shihui Yin, Usama Zaghloul Heiba, Wei Gong, Xuanle Ren, Xiaolan Zhou, and Zachary Schaffer. In particular, Enes Calayir, my first great officemate, friendly provided me with useful information and tips at the beginning of my Ph.D. journey; Jeronimo Segovia Fernandez, an intelligent senior student to me, patiently trained me to use fabrication tools, measurement instruments, and probe stations, which were critical for my research; Luca Colombo had worked with me in the clean room continuously for two months in 2016 and taught me funny Italian phrases.

I also want to extend my sincere thanks to CMU Nanofacility staff members, Matthew Moneck, Norman Gottron, and especially, James Rosvanis, whom I have bothered many times to dice wafers and recharge helium gas, as well as CMU ECE administrative officers, Samantha Goldstein and Nathan Snizaski, for answering my questions on the university policies.

I am obliged to my parents who raised me under difficult conditions and unconditionally support me over the last two decades. I also feel indebted to my girlfriend and her family. My girlfriend graduated from National Tsing Hua University, initially worked in Shanghai, and later decided to come to USA, primarily because of me. Her family, especially her mother, welcomed me and made me feel at home for my several visits to Wuhan.

Half of this work was funded by the Dynamic-Enabled Frequency Sources (DEFYS) Defense Advanced Research Projects Agency (DARPA) through the Microsystem Technology Office (MTO) under contract No. FA86501217624. The author also received Neil and Jo Bushnell fellowship toward completing this thesis.

TABLE OF CONTENTS

LIST OF TABLES

LIST OF FIGURES

CHAPTER 1: INTRODUCTION

Wireless communication technologies allow establishing links between mobile devices, for example, smartphones, laptops, and tablets, via the propagation of invisible and intangible electromagnetic (EM) waves. The growth and innovation of wireless communication technologies expands the way human beings process information and interact with their environment. Currently, 4G (short for “the fourth-generation wireless cellular service”) supersedes the earlier generations and enables various functionalities by supporting high-speed data exchange up to 100 megabits per second (Mbps) as well as high capacity for simultaneous access by many users [1, 2]. Therefore, with a single smartphone in hand, one can not only talk to others by voice, but also surf the Internet, check emails, watch videos, play games, plan travels, share his/her daily activities, and navigate through unfamiliar cities.

One aspect of the evolution of wireless communication technologies is the integration of transceivers (transmitters + receivers), which went from vacuum tubes plus high quality factor (Q) LC tanks to fully integrated complementary metal oxide semiconductor (CMOS) chips [3]. The ultimate future trend is a software-defined radio (SDR), in which the weak signals from antenna are amplified and converted to digital bits directly in the receiver path (similar architecture in the transmitter path but in the opposite direction) [4, 5]. The channel selectivity and demodulation are realized by pure digital signal processing. Such idea is very attractive because it allows ultimate flexibility and overcomes the limited capacity of the EM spectrum [6]. However, it is not feasible not only today but also in the foreseeable future, as it demands high-speed, high-resolution, thus power-hungry, expensive analog-to-digital converters (ADC) to accommodate a large input dynamic range from 1 μV to 1 V and a several-GHz-wide band [5]. Hence, current receivers down-convert radio frequency (RF) signals by mixers to either intermediate frequencies (IF) in the superheterodyne receivers or baseband in the direct-conversion receivers, in which ADC are more feasible and power-efficient [7]. In either one of the cases, low-noise local oscillators and high frequency-selectivity band-pass filters (BPF) are necessary, both dictating the use of high-Q building elements, for example, LC tanks. Unfortunately, a high-Q inductor is impossible for CMOS technologies due to the high resistive loss [8]. What makes inductor even more undesirable is that the area of a single coil might be as much as an entire microprocessor. In practice, the high-Q LC tanks are replaced by quartz crystal and surface acoustic wave (SAW) resonators. Nevertheless, these components are still bulky and incompatible with CMOS electronics, which impedes achieving the vision of fully integrated transceivers.

Another aspect of the evolution of wireless communication technologies is the increasing demand for speed and capacity of data exchange to accommodate the ever-growing number of wireless devices. Statistics shows that mobile data usage grows at over 50% annually. In 2021, it is expected that there will be 8.3 billion mobile users and 49 exabytes (EB) mobile data per month [9]. Both speed and capacity are closely related to the usage of the EM spectrum. Nonetheless, the available EM spectrum is a limited resource. There are two possible solutions. The first one is to extend the usage of EM spectrum to much higher frequencies. The current 4G-LTE (short for Long-Term Evolution) in USA occupies the EM spectrum up to 5 GHz, while the fifth-generation (5G) standard (which is under active research and development) aims at spreading the data transmission over a much wider frequency spectrum beyond 70 GHz [10, 11]. However, managing higher frequency signals tends to become more challenging [12, 13]. The second method is to improve the spectral efficiency. Conventionally, most contemporary communication equipment operates in half-duplex or out-of-band full-duplex, *i.e.* they transmit and receive either at different times (time-division duplexing, aka TDD) or over different frequency bands (frequency-division duplexing, aka FDD). Therefore, in-band full-duplex (IFBD), which allows simultaneous transmit and receive (STAR) over the same frequency band, becomes attractive because it potentially doubles the spectral efficiency [14]. A key block in enabling this vision is a 3-port circulator connecting antenna, receiver, and transmitter. The circulator would allow unidirectional (or non-reciprocal) signal power transmission and thus offers transmitter suppression (>15 dB) at the receiver (see Figure 1.1) [15]. Despite this promise, the intrinsic physics behind the principle of operation of existing circulators (either passives or actives) impedes them from withstanding large amounts of power and exhibit low loss and intermodulation distortion when packed in a very small form factor (< 3 mm in any direction) in the frequency range of most wireless communication standards.

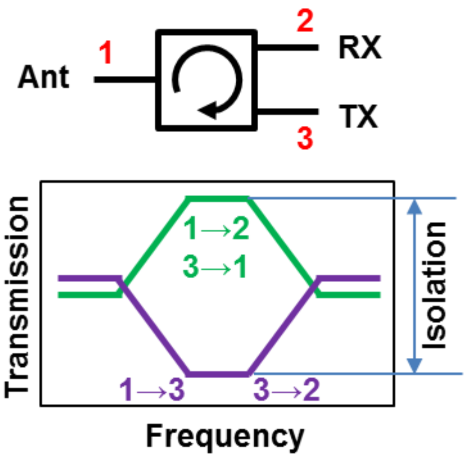

Figure 1.1: Schematic diagram of circulator in RF front-end and typical response.

There is clearly a need for integrated components that can overcome the limitations of existing devices, namely integrable and high performance resonator-based oscillators and on-chip miniaturized non-reciprocal components.

1.1. MEMS Resonators in RF Front-Ends

The development of 4G (and even the coming 5G) inevitably drives the quest for multi-band receivers, which includes WCDMA, GSM, GPS, WiFi (IEEE 802.11), WiMax (IEEE 802.16), BlueTooth (IEEE 802.15.1), etc [16]. This has led to the exploded demand of oscillators and filters not only for the whole market, but also in a single mobile handset. It is predicted that the number of filters in a smartphone will skyrocket to more than 100 in the future from fewer than 10 ten years ago [17]. However, the current quartz and SAW resonators won't be able to satisfy the trend of miniaturization and integration. Instead, MEMS resonators can potentially play significant roles and fulfill the requirement of many oscillators and filters on a single chip, reducing size, power, and assembly costs [18].

There are two main types of MEMS resonators: capacitive and piezoelectric. The first type is driven by electrostatic forces generated in the electrode-to-resonator gaps. Capacitive resonators typically exhibit high Q over 10,000 (even at frequencies well beyond 1 GHz) [19, 20], but suffer from small coupling coefficient, k_t^2 (<0.1%), and large motion resistance (R_M) in the 1 kΩ – 10 MΩ range [19, 21], which makes their use impossible in filter applications. Therefore, they are primarily used for oscillator applications and are commercially available [22, 23]. The second class of resonators is transduced by the piezoelectric effect, which refers to the direct conversion between electric polarization and mechanical strain. This phenomenon only occurs in some specific materials (*e.g.* ZnO, AlN, $LiNbO_3$) [24]. Among these piezoelectric materials, AlN has been widely used due to its high acoustic velocity and low instrinc material loss. In contrast to capacitive resonators, piezoelectric resonators offer low motional resistance (1–200 Ω) while maintaining high quality factors (1000–5000) [19], such that they can be used to build filters and duplexers. In piezoelectric resonators, thickness modes and longitudinal modes are generally excited, namely to synthesize what are known as film bulk acoustic resonators (FBAR) and contour-mode resonators (CMR). FBAR has become a commercial success in the application of duplexers and band filters for 4G-LTE frequency band with the advantage of large coupling coefficient, k_t^2 (around 5.5–7%), and high quality factor [25, 26]. However, it is neither easy nor cheap to implement multi-band and multi-frequency operations for FBAR, whose frequency is mainly determined by film thickness. Although the metal thickness can be employed to alter FBAR frequency with additional masks [27], metal electrodes would become too thick and degrade resonator performance, hence limiting the frequency tuning range. Compared to FBAR, the frequency of CMR is determined by the lateral dimensions, thus enabling monolithic solution of multiple-frequency ranging from 10 MHz to 10 GHz [28-31]. Moreover, CMR also show high quality factor and reasonably high k_t^2 (around 1–2.5%) [32], suitable for narrow band applications. Although smaller than FBAR, the coupling coefficient of CMR can be improved by 3~5 times with scandium-doped AlN (Sc-AlN) [33, 34]. Therefore, CMR have gained attention and is a promising candidate for replacing bulky quartz and SAW in the next generation of RF front-end.

To date, RF MEMS resonators (include CMRs) have been extensively studied; however, one aspect that was not thoroughly investigated is how to modulate/tune their equivalent parameters to enhance their performance in oscillators and duplexers. Therefore, the goal of this thesis is to investigate various modulation methods to improve the thermal stability of the resonator, boost its "effective" quality factor in an oscillator circuit, and build completely new non-reciprocal components. Broadly defined, modulation refers to the exertion of a modifying or controlling influence on something, specifically, the resonator admittance in this thesis. The thesis will present three categories of modulation methods: thermal modulation to attain resonator temperature stability of 14 ppm over 120 ℃ and consuming only 390 μW, force modulation to enhance the effective quality factor of a resonator by 140 times and improve the phase noise performance of an oscillator by as much as 10 dBc/Hz, and external electronic modulation to synthesize one of the first magnetic-free integratable acoustic-based circulator at 1.1 GHz.

Ultimately, the author believes that a fully integrated, multi-frequency, spectrum-efficient transceiver, for example, a direct-conversion version as shown in Figure 1.2, would become possible by following the pathway set in this thesis. Thus, this work potentially has a dramatic impact in the wireless industry by offering a small form factor, power efficient, cost effective, high speed, and larger capacity solution.

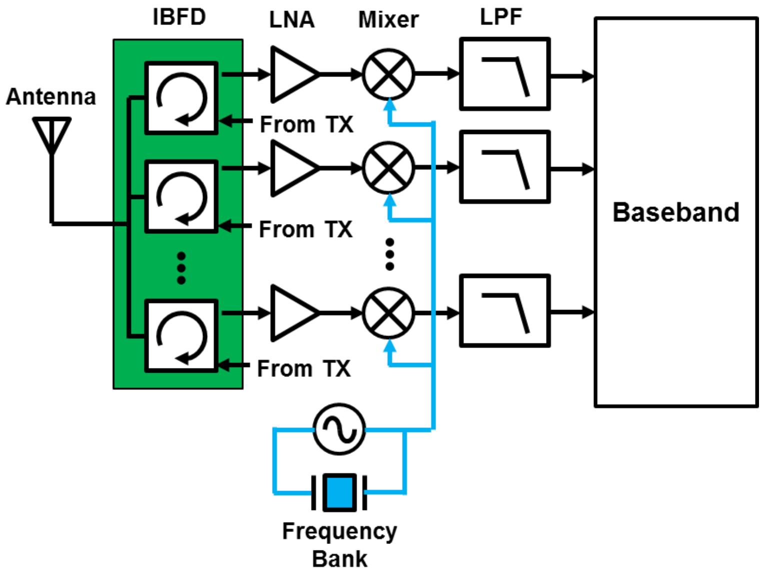

Figure 1.2: Schematic overview of a single-chip solution that is envisioned by using CMOS and CMOS-compatible AlN MEMS technologies. The IBFD also functions as band-selection. Green and blue colored elements are the focus of this thesis.

1.2. Outline of Thesis

The dissertation is organized in the following chapters.

In Chapter 2, the operation principle of AlN CMR is briefly explained, followed by the derivation of mechanical and electrical models, an overview of their typical CMOS-compatible fabrication process, and the methods available for device characterization and parameter extraction. Then, their primary application in local oscillators and front-end filters is described. Emphasis is placed on how the resonator figure-of-merit (*FoM*) affects the performance of oscillators and filters. Lastly, the temperature coefficient of frequency (TCF) is defined and various compensation methods implemented to date are reviewed.

In Chapter 3, the underlying trade-off between ovenization power and quality factor (Q) for conventional piezoelectric resonator design is formulated. The first sub-milliwatt (as low as 353 μW over 120 °C) ovenized resonator design is presented to mitigate the aforementioned trade-off (Q as high as 4450). Two temperature compensation methods, analog and digital, are developed and demonstrated using these low power ovenized resonators. These implementations are focused on showcasing how a full control loop can be implemented and addresses some of the challenges generally associated with power consumption, degradation of sensor accuracy due to routings, and slow calibration process.

In Chapter 4, a novel method to boost the quality factor of AlN CMR by means of "force" modulation is presented. Theory of a simpler but analogous system is used to explain the principle of operation of this technique. Q boosting up to 150,000 is experimentally demonstrated and its use to reduce oscillator phase noise by at least 10 dBc/Hz is verified.

In Chapter 5, a CMOS-compatible magnetic-free circulator that combines linear-time-invariant (LTI) networks and RF switches is proposed and demonstrated. A generalized model is derived to accurately predict the proposed circulator's behavior, *i.e.* the reflection, insertion loss, and isolation for different modulation frequencies and ratios (related to the duty cycle of square waves). These models are experimentally verified. Most interestingly, an integratable circulator based on AlN MEMS CMRs and ADI RF switches is demonstrated to provide 15 dB isolation between the transmit and receive paths.

In Chapter 6, the entire body of the Ph.D. work is summarized and some future directions are presented.

CHAPTER 2: INTRODUCTION TO ALUMINUM NITRIDE CONTOUR MODE RESONATORS

A possible vision for future consumer electronics for wireless communications is a monolithic, multi-band, high-performance, power-efficient, and cost-saving solution for radio frequency (RF) front-ends. A bottleneck to the implementation of this vision is the fact that components such as surface acoustic wave (SAW) and quartz crystals, which are not CMOS compatible, are vital to the synthesis of high performance RF front-ends. MEMS resonators are promising replacements for these legacy technologies, as they offer small form factor, low production cost, low power consumption, and high level of integration with CMOS electronics.

MEMS resonators are classified into two dominant classes according to the transduction mechanisms: electrostatic and piezoelectric. Both classes show 100–10,000 times higher quality factor than CMOS LC tanks. However, piezoelectric resonators are superior to the electrostatically transduced ones, in terms of simple operation without bias voltage, large electromechanical coupling, and low motional resistance, R_M, which permits direct interfacing with 50 Ω RF networks. Moreover, it is easier to fabricate a piezoelectric resonator, while nano-gaps, key elements of an electrostatic resonator, require much more complex fabrication efforts [35].

Among piezoelectric resonators, the frequencies of film bulk acoustic resonators (FBARs) and shear-mode resonators are mainly determined by the thickness of piezoelectric films, therefore they are not suitable for monolithic multi-band solutions. However, AlN contour-mode resonator (CMR), utilizing the S_0 mode and belonging to the class of Lamb wave resonators offer a more promising solution for multi-frequency operation since its resonant frequency is defined by in-plane dimensions. This chapter introduces the operation principles of AlN CMRs, and the associated methods for modeling, fabrication, characterization, and temperature compensation of the same. The use of these devices in oscillators and filters is also described.

2.1. Operation Principle of AlN CMRs

AlN is a popular piezoelectric material. Piezoelectricity relates the change in electric polarization to a mechanical strain in the crystal. The reverse piezoelectricity is the generation of a mechanical strain resulting from an applied electric field. Piezoelectricity is described by the constitutive equations of a material by using the IEEE standard notation (ANSI/IEEE Std 176-1987) in the two most commonly used forms: strain-charge form and stress-charge form. The strain-charge form is

$$\begin{aligned} \mathbf{S} &= \mathbf{s_E T} + \mathbf{d}^T \mathbf{E} \\ \mathbf{D} &= \mathbf{d_E T} + \boldsymbol{\varepsilon}_\mathbf{T} \mathbf{E} \end{aligned} \tag{2.1}$$

where $\mathbf{S}$ represents the strain (6 by 1 vector), $\mathbf{T}$ the stress (6 by 1 vector), $\mathbf{D}$ the electric displacement (3 by 1 vector), and $\mathbf{E}$ the electric field (3 by 1vector); $\mathbf{s_E}$ is the compliance matrix (6 by 6) in a constant electric field, $\mathbf{d}$ the piezoelectric charge coefficient matrix (6 by 3), $\mathbf{d}^T$ the transpose of $\mathbf{d}$ (3 by 6), and $\boldsymbol{\varepsilon}_\mathbf{T}$ is the dielectric constant matrix (3 by 3) under a constant stress. The stress-charge form is

$$\begin{aligned} \mathbf{T} &= \mathbf{c_E S} - \mathbf{e}^T \mathbf{E} \\ \mathbf{D} &= \mathbf{d_E S} + \boldsymbol{\varepsilon}_\mathbf{S} \mathbf{E} \end{aligned} \tag{2.2}$$

where $\mathbf{c_E}$ is the stiffness matrix (6 by 6) in a constant electric field, the $\mathbf{e}$ the piezoelectric stress coefficient matrix (6 by 3), and $\boldsymbol{\varepsilon}_\mathbf{S}$ is the dielectric constant matrix (3 by 3) under a constant strain. The transform relationship between these two forms is

$$\begin{aligned} &\mathbf{s_E} = \mathbf{c_E}^{-1} \\ &\mathbf{e} = \mathbf{d} \cdot \mathbf{c_E} \\ &\boldsymbol{\varepsilon}_\mathbf{T} - \boldsymbol{\varepsilon}_\mathbf{S} = \mathbf{d} \cdot \mathbf{c_E} \cdot \mathbf{d}^T \end{aligned} \tag{2.3}$$

For AlN material, the stiffness matrix, the piezoelectric charge coefficient matrix, and dielectric constant matrix are [36, 37]

$$\mathbf{c_E} = \begin{bmatrix} c_{11} & c_{12} & c_{13} & & & \\ c_{12} & c_{11} & c_{13} & & & \\ c_{13} & c_{13} & c_{33} & & & \\ & & & c_{44} & & \\ & & & & c_{44} & \\ & & & & & \frac{c_{11}-c_{12}}{2} \end{bmatrix} = \begin{bmatrix} 3.45 & 1.25 & 1.20 & & & \\ 1.25 & 3.45 & 1.20 & & & \\ 1.20 & 1.20 & 3.95 & & & \\ & & & 1.18 & & \\ & & & & 1.18 & \\ & & & & & 1.10 \end{bmatrix} \left(10^{11} N/m^2\right) \tag{2.4}$$

$$\mathbf{d}^T = \begin{bmatrix} 0 & 0 & 0 & 0 & d_{15} & 0 \\ 0 & 0 & 0 & d_{15} & 0 & 0 \\ d_{31} & d_{31} & d_{33} & 0 & 0 & 0 \end{bmatrix} = \begin{bmatrix} 0 & 0 & 0 & 0 & -4 & 0 \\ 0 & 0 & 0 & -4 & 0 & 0 \\ -1.98 & -1.98 & 4.98 & 0 & 0 & 0 \end{bmatrix} \left(10^{-12} C/N\right) \tag{2.5}$$

$$\boldsymbol{\varepsilon}_\mathbf{T} = \begin{bmatrix} \varepsilon_{11} & & \\ & \varepsilon_{11} & \\ & & \varepsilon_{33} \end{bmatrix} = \begin{bmatrix} 9.2 & & \\ & 9.2 & \\ & & 11.9 \end{bmatrix} \varepsilon_0 \tag{2.6}$$

$$\boldsymbol{\varepsilon}_\mathbf{S} = \begin{bmatrix} \varepsilon_{11} & & \\ & \varepsilon_{11} & \\ & & \varepsilon_{33} \end{bmatrix} = \begin{bmatrix} 9.0 & & \\ & 9.0 & \\ & & 10.7 \end{bmatrix} \varepsilon_0 \tag{2.7}$$

where $\varepsilon_0 = 8.85 \times 10^{-11}$ F/m is the dielectric constant of vacuum. The matrix features indicate c-axis oriented AlN is laterally isotropic. Fundamentally, this is because the lattice structure of AlN belongs to the hexagonal system. Therefore, the device orientation doesn't matter to the performance [38].

To excite contour-extensional vibrations in a rectangular AlN body, the film is sandwiched between two metals, usually top aluminum (Al) interdigitated (IDT) electrodes and a bottom platinum (Pt) plate. Depending on how the excitation signal is applied, the device can be classified as either one-port or two-port resonator, as shown in Figure 2.1. In one-port AlN CMR, the bottom metal is floating but used to confine the electric field, while it is grounded in the two-port counterpart, in which one of the two ports is used as input and the other as output. The detailed working principle of AlN CMR can be found in [28, 29, 39]. Essentially, in either case, the lateral vibration is excited through d_{31}, when a vertical electrical field is exerted on the AlN body. The interdigitated electrodes are used to excite higher order vibrations in the AlN body. Critical resonator dimensions are: length, L, film thickness, T, finger pitch, P, finger width, W_e, and finger number, n. The resonant frequency of vibration, f_s, can be mainly defined by the finger pitch, P, as

$$f_s = \frac{1}{2P}\sqrt{\frac{E_{eq}}{\rho_{eq}}} \tag{2.8}$$

where E_{eq} and ρ_{eq} represent the equivalent Young's modulus and mass density of the stacked layers, respectively. Other geometrical parameters impose second-order effect on f_s , which could be taken into account for by two- or three-dimensional finite element analysis (2D/3D FEA).

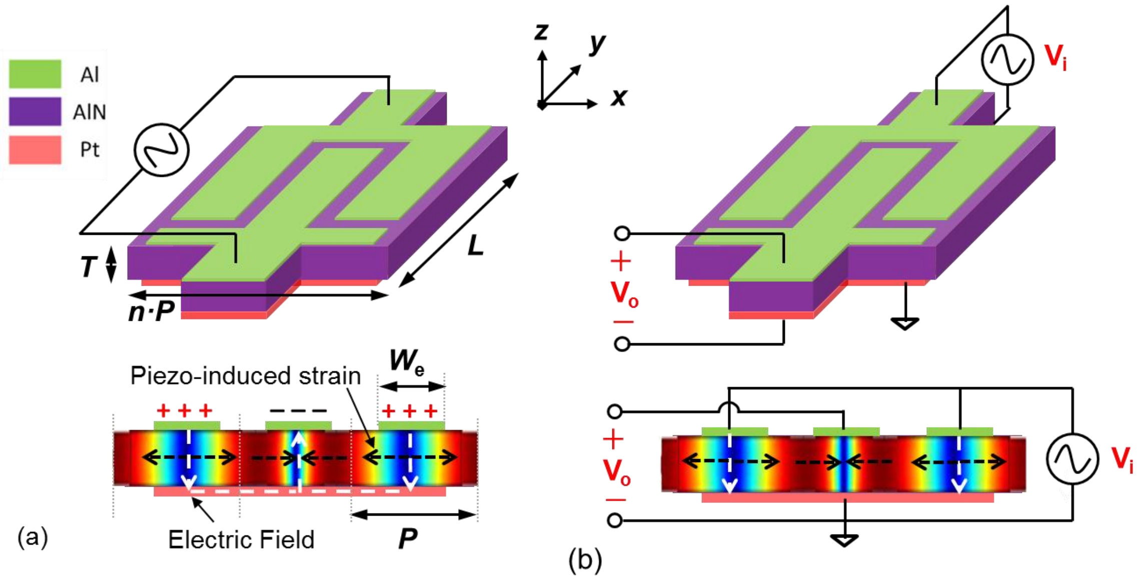

Figure 2.1: 3D view and cross-sectional representation of 3-finger (a) one-port and (b) two-port AlN CMR.

From the acoustic wave perspective, the vibration is formed by a standing S_0 Lamb wave in the resonator body. The wavelength, λ, is twice the finger pitch, 2*P*. The governing equations can be simplified to the one of an isotropic homogeneous 1D resonator without damping:

$$\frac{\partial^2 u(x,t)}{\partial t^2} = c^2 \frac{\partial^2 u(x,t)}{\partial x^2} \tag{2.9}$$

where $u(x,t)$ is the displacement field in the x-axis varying over time, t, and c is the acoustic velocity, which is equal to the square root of the ratio of Young's modulus to mass density, as shown in Eq. (2.8). The solution reads as:

$$u(x,t) = U_0 \phi(x) \varphi(t) = U_0 \sin(kx) \exp(\omega_s t) \tag{2.10}$$

where ϕ (x) is the mode shape (in space), $\varphi(t)$ describes the vibration (in time), $k = \frac{2\pi}{\lambda} = \frac{\pi}{P}$ is the wave number, $\omega_s = 2\pi f_s$, and U_0 is the maximum lateral displacement.

2.2. Mechanical and electrical models

The AlN CMR can be lumped into a single degree-of-freedom (SDOF) spring-damper-mass system (Figure 2.2a) by equating total kinetic and potential energy of the resonator to the energy of the point of the maximum displacement at the resonant frequency, ω_s=2πf_s. The equivalent mass, M_{eq}, damping coefficient, D_{eq}, and spring constant, K_{eq}, are expressed as

$$M_{eq} = \frac{\frac{1}{2}\int\left[\omega_s U_0 \phi(x)\right]^2 dV}{\frac{1}{2}(\omega_s U_0)^2}, K_{eq} = \omega_s^2 M_{eq}, D_{eq} = \frac{\omega_s M_{eq}}{Q} \tag{2.11}$$

where Q is the quality factor of the resonator at resonant frequency, which is given by

$$Q = 2\pi \frac{\text{Average energy stored}}{\text{Energy lost per cycle}} \tag{2.12}$$

and is equal to the ratio of resonant frequency to 3-dB bandwidth for second-order systems. Although Eq. (2.11) is formulated for a 1D resonator, it also is valid for 2D and 3D. The spring-damper-mass system shows as a natural analogy to a series L-C-R circuit (Figure 2.2b). Comparing their second-order differential equations,

$$M_{eq}\ddot{x}(t)+D_{eq}\dot{x}(t)+K_{eq}x(t)=F(t)$$
$$L_M\ddot{q}(t)+R_M\dot{q}(t)+\frac{1}{C_M}q(t)=V(t) \tag{2.13}$$

By defining a transduction coefficient, $\eta=\frac{F}{V}=\frac{q}{x}=\frac{i}{\dot{x}}$ where i is the motional current, the AlN CMR can be transformed from mechanical domain to electrical domain by the following relations

$$L_M=\frac{M_{eq}}{\eta^2},R_M=\frac{D_{eq}}{\eta^2},C_M=\frac{\eta^2}{K_{eq}} \tag{2.14}$$

By its definition, η describes how the vertical electrical field is converted into lateral stress as well as how the lateral motion is related to the surface charge of the AlN film. For the AlN CMR of interest, η can be approximated as

$$\eta=2d_{31}E_{eq}L \tag{2.15}$$

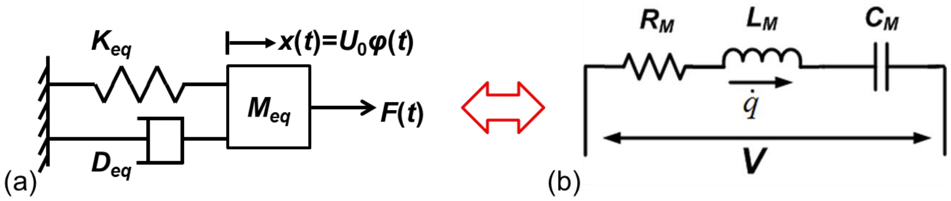

Figure 2.2: Equivalent a) mechanical and b) electrical lumped models of AlN CMRs.

By adding a capacitor, C_0, in parallel with the equivalent LCR circuit, the Butterworth Van Dyke (BVD) model that represents a one-port resonator can be obtained, as shown in Figure 2.3a. By defining an electromechanical coupling coefficient, k_t^2, as

$$k_t^2=\frac{\text{Output mechanical energy}}{\text{Input electrical energy}}\approx\frac{\pi^2}{8}\frac{C_M}{C_0} \tag{2.16}$$

the equivalent electrical parameters can be calculated in a more insightful way:

$$R_M=\frac{\pi^2}{8}\frac{1}{\omega_s C_0}\frac{1}{k_t^2 Q},C_M=\frac{8}{\pi^2}k_t^2C_0,L_M=\frac{\pi^2}{8}\frac{1}{\omega_s^2k_t^2C_0} \tag{2.17}$$

To more accurately model the resonator and account for the parasitic parameters via a series resistor, R_S, and a parallel resistor, R_0, a modified BVD model (mBVD) is introduced as shown in Figure 2.3b. Since R_S degrades the resonator's quality factor, a loaded quality factor, Q_{load}, is employed to refer to the degraded Q and is differentiated from the original Q used in Eq. (2.17), which is called the unloaded quality factor, Q_{un}. They both can be calculated by Eq. (2.12) and are given by:

$$Q_{un} = \frac{\omega_s L_M}{R_M}, Q_{load} = \frac{\omega_s L_M}{R_S + R_M} \tag{2.18}$$

The typical admittance response of an AlN CMR is shown in Figure 2.4. Beside the series resonant frequency, f_s, there is a parallel resonant frequency, f_p, at which L_M and C_M together resonate with C_0 generating an equivalent large impedance. The relationship between the two frequencies is given by

$$f_p = f_s \sqrt{1 + \frac{C_M}{C_0}} \tag{2.19}$$

which offers another way of directly extracting k_t^2:

$$k_t^2 = \frac{\pi^2}{8} \frac{f_p^2 - f_s^2}{f_s^2} \tag{2.20}$$

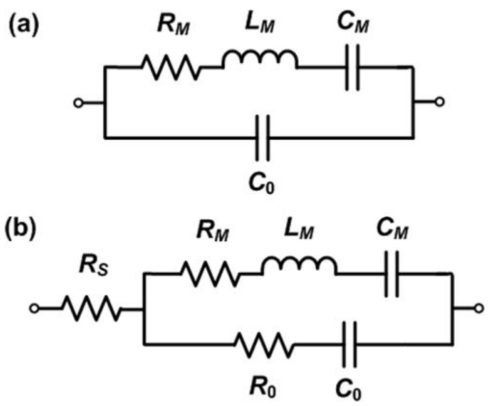

Figure 2.3: (a) BVD and (b) mBVD model.

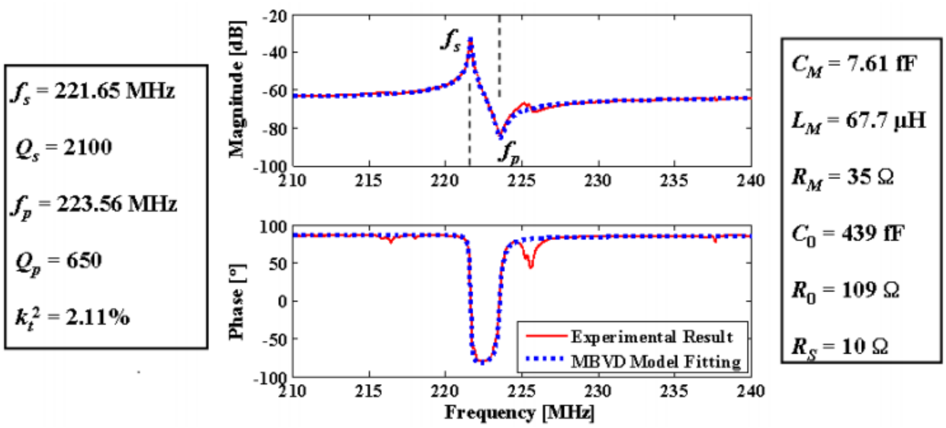

Figure 2.4: An example admittance plot and mBVD model fitting for a 221.6 MHz AlN CMR reprinted from [39]. Resonator dimensions are: *n* = 3, *L* = 200 μm, *T* = 2 μm, and *P* = 20 μm. The fitting procedure will be discussed in Section 2.4.

The electrical model for two-port resonators (Figure 2.5) can be obtained in a similar way. More details can be found in [29, 39]. The transform ratio, N, is determined by the ratio of input finger number to the output finger number (and any change in electrode covereage if that is present). Its sign depends on the resonator configuration and is positive for Figure 2.1. It should be also noted that, compared to one-port resonator, the electromechanical coupling coefficient of two-port resonator stays the same (because it is rather intrinsic to the piezoelectric material rather than dependent of the geometry of the transducer) while the $C_0 = (C_i + C_o)/2$ approximately doubles. Hence, k_t^2 is estimated as

$$k_t^2 = \frac{\text{Output mechanical energy}}{\text{Input electrical energy}} \approx \frac{\pi^2}{4}\frac{C_M}{C_0} \tag{2.21}$$

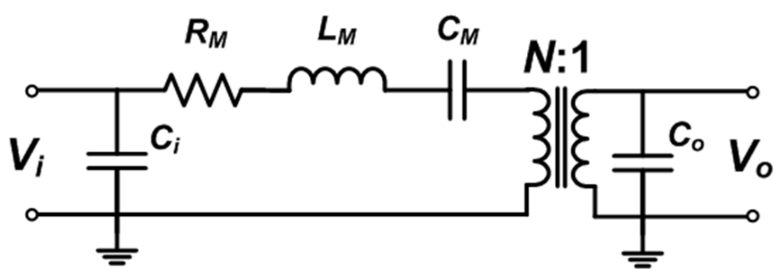

Figure 2.5: Electrical lumped model of a two-port AlN CMR.

2.3. Fabrication process

The method developed in our laboratory to rapidly prototype AlN CMRs is based on a 4-mask process as shown in Figure 2.6. It starts with the deposition and patterning of 100 nm Pt by DC sputtering and lift-off, respectively. The second step is the deposition of 1 μm AlN film in a Tegal AMS system. The deposition process is controlled so that the residual in-plane stress can be set to be less than 100 MPa and the full width at half maximum (FWHM) of the rocking curve is below 2 °(important to attain high quality factor films). Before the final patterning of top 100 nm metal electrodes (the third layer), via openings with gradual slope are etched in the AlN film (this is required only for two-port resonators). The via slope is attained by post-backing of photoresist and the reflowing of the resist side-wall [40]. The resonator boundaries are defined by the etching of the release windows. Contrary to via openings, a vertical slope in the AlN film is preferred so as to mitigate the deviation from the desired frequency, the emergence of spurious modes [41], and the adverse degradation of *Q* [42]. Steeper sidewall is usually achieved by hard marks (e.g. SiO_2). In the end, the resonator is released by an isotropic etch of Si substrate using XeF_2. The detailed processing steps can be found in [43]. As can be seen, the fabrication process is compatible with CMOS technologies and could be manufactured in the back-end-of-the-line (BEOL) of a CMOS line. Since the total release region has a second-order effect on the resonant frequency, it would be better to control the amount of silicon undercut. A more complex fabrication process aiming at better control of the release region will be briefly discussed in Chapter 4.

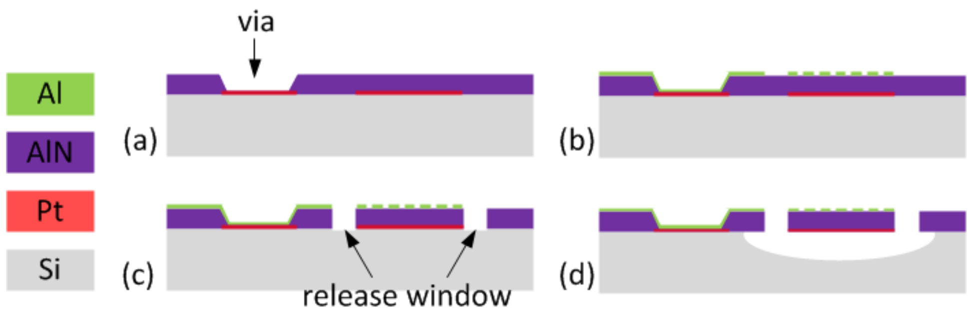

Figure 2.6: Schematic representation of the 4-mask fabrication process for making AlN CMR: a) sputtering and patterning of the bottom metal plate (first layer), deposition of the AlN thin film (second layer) and via opening in Cl_2-based reactive ion etching (RIE); (b) sputtering and patterning of the top electrode (third layer); c) dry etching of AlN in Cl_2-based RIE; d) isotropic release of the AlN resonator in XeF_2 atmosphere.

2.4. Resonator Characterization

The AlN resonators are commonly tested in an RF probe station. S-parameters are generally measured for these devices. The brief introduction of S-parameters can be found in [8]. For a one-port resonator, S_{11} is enough to characterize its performance, while a 2×2 S-parameter matrix ($\begin{pmatrix} S_{11} & S_{12} \\ S_{21} & S_{22} \end{pmatrix}$) is needed to fully describe a two-port resonator. S-parameters are obtained through a Vector Network Analyzer (VNA) (Agilent N5230A in this work) after performing a short-open-load (SOL) or short-open-load-through (SOLT) calibration to remove the loss and delay effect of cables and probes. With S-parameters available, other parameters, e.g. admittance matrix, **Y**, impedance matrix, **Z**, and **ABCD** matrix, can be calculated [44] and the resonator equivalent electrical model extracted accordingly. In this thesis, the admittance matrix is more frequently used to represent the resonator.

For one-port resonator, the series resonant frequency, ω_s, parallel resonant frequency, ω_p, series 3-dB quality factor, Q_s, admittance at low frequency (ω_l) far from resonance, Y_l, are directly observed from the measured data. Then the BVD model parameters are readily extracted:

$$C_0 = \frac{|Y_l|}{\omega_l}, C_M = C_0\left[\left(\frac{\omega_p}{\omega_s}\right)^2 - 1\right], L_M = \frac{1}{\omega_s^2 C_M}, R_M = \frac{\omega_s L_M}{Q_s} \tag{2.22}$$

In practice, C_0 is extracted by interpolating the admittance response at low frequencies (the value of slope is the C_0) to alleviate the effect of noise in the measurement.

To extract the MBVD model, additional parallel 3-dB quality factor, Q_p, is needed. The parameters can be obtained by solving the following six equations simultaneously [45]

$$\begin{gathered} \mathrm{Re}[1/Y_l] = R_S + R_0, \mathrm{Im}[1/Y_l] = -\frac{1}{\omega_l C_0} \\ \omega_s^2 = \frac{1}{L_M C_M}, \left(\frac{\omega_p}{\omega_s}\right)^2 = 1 + \frac{C_M}{C_0} \\ Q_s = \frac{1}{\omega_s (R_M + R_S) C_M}, Q_p = \frac{1}{\omega_p (R_M + R_0) C_M} \end{gathered} \tag{2.23}$$

The example fitting has been shown in in Figure 2.4.

For two-port resonator (Figure 2.5), the admittance matrix is formulated in the following way:

$$\begin{aligned} Y_{LCR} &= \left(R_M + j\omega L_M + \frac{1}{j\omega C_M}\right)^{-1} \\ Y_{11} &= j\omega C_i + Y_{LCR} \\ Y_{22} &= j\omega C_o + N^2 Y_{LCR} \\ Y_{12} &= Y_{21} = Y_{LCR}/N \end{aligned} \tag{2.24}$$

As can be easily seen, Y_{11} acts like a one-port resonator in Figure 2.3a, except C_0 is replaced with C_i. Therefore, we can easily extract C_i, R_M, L_M, and C_M, and then obtain N and C_o from Y_{12} and Y_{22}, respectively.

2.5. Resonator-Based Oscillators

One of the common way to build an oscillator is to attach a resonator to an active circuit that cancels the loss in the resonator, as shown in Figure 2.7a. The active circuit can be seen as a negative resistance R_N in series with a load capacitance C_L, which are expressed as [8]

$$R_N = -\frac{g_m}{\omega^2 C_1 C_2}, C_L = \frac{C_1 C_2}{C_1 + C_2} \tag{2.25}$$

where ω is the operating frequency, g_m is the small-signal transconductance of the NMOS transistor, C_1 and C_2 are two capacitors tied from the gate and drain of the transistor to its source. Separating the circuit into mechanical and electrical parts (Figure 2.7b), the oscillator circuit can be further simplified to Figure 2.7c, with the values of four components being expressed as [46]

$$\begin{gathered} L_E = \frac{2(\omega - \omega_s)}{\omega^2 \omega_s C_M} = \frac{2p}{\omega^2 C_M}, p = \frac{\omega - \omega_s}{\omega_s} << 1 \\ Z_{ET} = \left[R_N + R_S + 1/(j\omega C_L)\right] \| \left[R_0 + 1/(j\omega C_0)\right] \\ R_{EN} = \mathrm{Re}(Z_{ET}), C_{EL} = -1/\left[\omega \cdot \mathrm{Im}(Z_{ET})\right] \end{gathered} \tag{2.26}$$

where p is the frequency pulling factor which indicates the relative amount of frequency pulling above the series resonant frequency, ω_s, and Z_{ET} is the total impedance of the electrical part. For oscillation to occur, the sum of R_{EN} and R_M should be negative. Thus, the critical transconductance, g_{mc}, is the value of g_m that satisfies $R_{EN} + R_M = 0$, at the operating frequency, ω_c, that is the solution of $\omega^2 L_E C_{EL} = 1$.

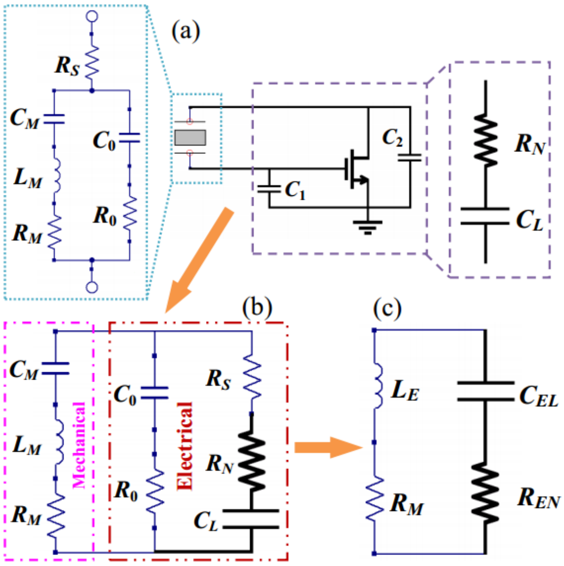

Figure 2.7: (a) Equivalent circuits of the Pierce oscillator based on one-port AlN CMR. (b) Separation of the motional (mechanical) and electrical parts of the circuit. (c) Rearrangement of components. [46]

Another common and equivalent way to build an oscillator is to form a loop by using an amplifier, a phase shifter, and a resonator, as shown in Figure 2.8a. For oscillation to occur at frequency, ω_c, the loop gain, $L_G(\omega)$, must satisfy the following condition:

$$\left|L_G(\omega_c)\right| \geq 1 \tag{2.27a}$$

$$\angle L_G(\omega_c) = 360° \tag{2.27b}$$

which are called Barkhausen's criteria [8]. The loop gain can be calculated by breaking the oscillator loop (Figure 2.8b) as

$$L_G(\omega) = \frac{V_{out}}{V_{in}} = A(\omega)e^{j\Phi(\omega)}Z_{res}(\omega) \tag{2.28}$$

Compared to the first method, this method offers more flexibility in building off-chip oscillators when a programmable phase shifter is available. At the same time, it is possible that Eq. (2.24) is satisfied for many frequencies that can be far away from the resonator's center frequency because of other parasitic resonances. Therefore, band-pass filter or low-pass filter (not shown in the figure) need be introduced in the loop to ensure the oscillator operates at the desired frequency.

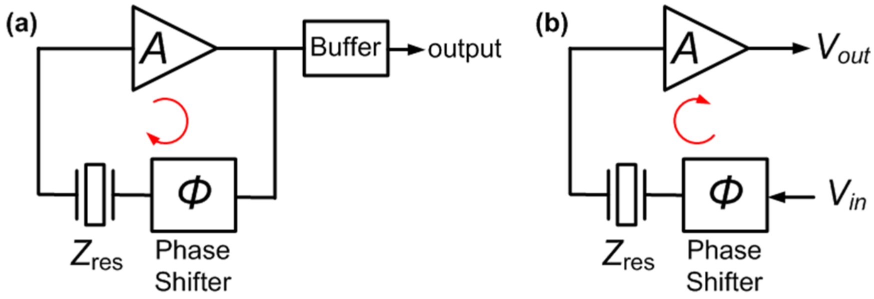

Figure 2.8: (a) Oscillator loop formed by amplifier, phase shifter, and resonator. (b) Open loop of the oscillator.

2.6. Resonator-Based Filters

There are two main topologies that have been used to build filters using exclusively MEMS resonators, mostly based on a ladder network topology. There are two different ways to implement it and couple resonators to each other. The first topology is shown in Figure 2.9. The basic building block is formed by two resonators arranged in a series/shunt configuration. The shunt resonator has a certain amount of frequency down shift with respect to the series resonator so that its f_p overlaps with the f_s of the series resonator. The filter center frequency, f_c, is very close to the resonator series resonant frequency. In this way, one can build a band pass filter with a bandwidth, BW, related to k_t^2:

$$\frac{BW}{f_c} \approx \frac{8}{\pi^2} k_t^2 \tag{2.29}$$

The maximum out-of-band rejection is

$$S21_{out}^{\max} = \frac{1}{1 + \frac{1}{2}\frac{C_0^p}{C_0^s}} \tag{2.30}$$

where C_0^s and C_0^p are the parallel capacitor of series and shunt resonators, respectively. In order to minimize the insertion loss, IL, at f_c, the termination resistance, R_{term}, is set to

$$R_{term} \approx \frac{1}{2\pi f_c \sqrt{C_0^s C_0^p}} \tag{2.31}$$

which results in minimum IL of

$$IL = 1 - \frac{n}{2\pi f_c C_0^s R_{term} k_t^2 Q} \tag{2.32}$$

where n refers to the number of series resonators. In depth investigations of these filters using MEMS devices can be found in [47-51].

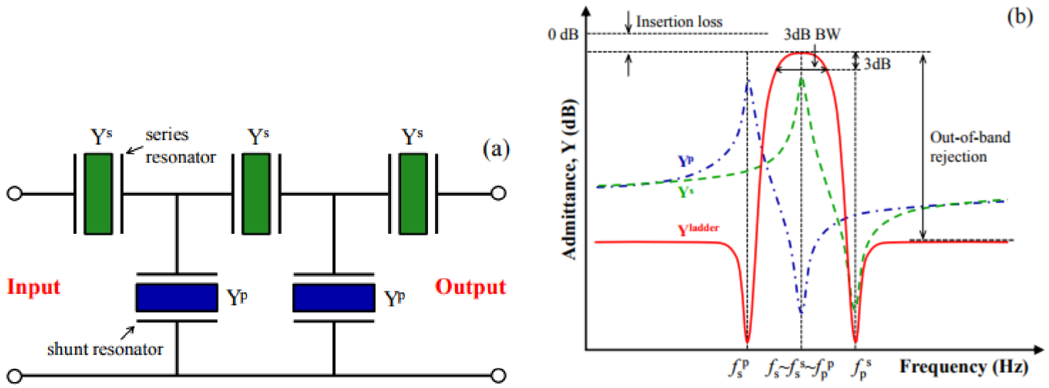

Figure 2.9: (a) Ladder filter with AlN CMR. (b) The typical frequency spectrum and common parameters for evaluation. Reprinted from [52].

In the second topology, two-port resonators are coupled to the adjacent ones. As shown in Figure 2.10, three resonators together create three basic resonant modes [53], and the bandwidth is less than half of what can be attained in the first configuration:

$$\frac{BW}{f_c} \approx \frac{3}{\pi^2} k_t^2 \tag{2.33}$$

The termination resistance is selected as

$$R_{term} = \left| \frac{1}{j\omega_s C_0} \right| \tag{2.34}$$

to maximize power transmission from input to output port. Correspondingly, the minimum insertion loss is

$$IL \approx \frac{R_{term}}{R_{term} + nR_M} = \frac{4}{4 + n\pi^2 / k_t^2 Q} \tag{2.35}$$

The out-of-band rejection is limited by the feedthrough capacitance, C_f (which is not modeled in Figure 2.5)

$$Rej \approx \frac{C_f}{C_0} \tag{2.36}$$

From Eq. (2.32) and (2.35), the *IL* of both topologies is dictated by k_t^2Q, which is used as a figure of merit (*FoM*) for resonators. Although exhibiting smaller bandwidth, the second topology is simpler to implement. Furthermore, it readily offers better out-of-band rejection up to 60 dB, while it would be harder to attain same levels or rejection in the first topology without any additional external component.

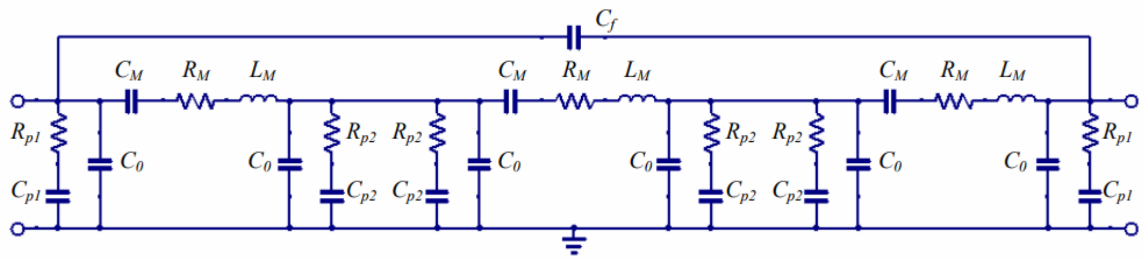

Figure 2.10: Overall equivalent circuit model of a 3rd order channel-select filter based on self-coupled AlN CMRs. Reprinted from [53].

2.7. Temperature Coefficient of Frequency

The resonant frequency of AlN CMR shows linear temperature dependence. The resonator frequency is determined by finger pitch, equivalent Young's modulus and mass density, which all vary when they are subjected to a temperature change. The temperature dependence of the resonator center frequency is characterized by the temperature coefficient of frequency, *TCF*, which is given by [28]

$$\begin{aligned} TCF &= \frac{1}{f_s}\frac{\partial f_s}{\partial T_e} = \frac{1}{P}\frac{\partial P}{\partial T_e} + \frac{1}{2}\frac{1}{E_{eq}}\frac{\partial E_{eq}}{\partial T_e} - \frac{1}{2}\frac{1}{\rho_{eq}}\frac{\partial \rho_{eq}}{\partial T_e} \\ &= -\alpha_1 + \frac{1}{2}\frac{\partial}{\partial T_e}\left(\ln E_{eq}\right) + \frac{1}{2}\left(2\alpha_1 + \alpha_3\right) \end{aligned} \tag{2.37}$$

where T_e stands for temperature, α_1 and α_3 are the linear coefficient of thermo-expansion for AlN in the 1 and 3 directions, respectively; $\frac{\partial}{\partial T_e}\left(\ln E_{eq}\right)$ is temperature coefficient of equivalent Young's modulus (*TCE*). AlN *TCE* contributes the most to the resonator *TCF* [54]. The theoretical value calculated from Eq. (2.37) is –16 ppm/ ℃ [28]. The typical experimental value of *TCF* varies between –22 and –33 ppm/ ℃ [55, 56], which results in over 3000 ppm shift across the temperature range of –40 to +80 ℃. Filters can generally tolerate these variations as they operate over relatively wide bandwidths and no nearby channels are present. However, for development timing references the requirements are much more stringent and, in general, the frequency variations over temperature (–25 ℃ to 80 ℃) are set to be the well below 50 ppm. Therefore, temperature compensation is necessary to facilitate the use of AlN CMRs as timing references.

2.7.1. Temperature Compensation

All temperature compensation methods for MEMS resonators can be categorized as either passive or active based on whether any power is consumed in controlling the resonator temperature. Generally, the passive methods take advantage of material or other physical properties that affect the resonant frequency and thus consume no power. For capacitive resonators, Si degenerate doping [57], charge carrier depletion [58] , substrate stress [59], and addition of oxide in the device stack [60, 61] have been demonstrated to effectively reduce the resonator *TCF*. However, for piezoelectric resonators, these methods are not applicable except for the use of silicon dioxide in the film stack [62]. Oxide compensation is pretty straightforward. An oxide layer exhibits positive *TCE* and cancels the negative *TCE* of the AlN layer. This compensation method is effective over a very wide temperature range, but the oxide thickness has to be comparable to the device thickness, hence degrading the resonator k_t^2.

Active methods generally combine frequency tuning mechanisms with a temperature sensor and use a feedback loop to set the device temperature/operating frequency, hence consuming power in doing so. The frequency tuning mechanism can be implemented at the device or circuit level. Electrostatic tuning is a common device-level method for capacitive resonators, in which the device stiffness can be softened via DC voltage [63]. However, the same technique is not effective for piezoelectric resonators, as the frequency shift due to an applied DC voltage is less than 5 ppm/V [28]. Another common device-level tuning technology is ovenization, in which thermal power is applied to change the resonator temperature via a micro-heater integrated with the resonator. The embodiment of this method in electrostatic resonators can be found in [64, 65]. The ovenized piezoelectric resonator design will be discussed in greater details in Section 2.7.2 and Chapter 3. In contrast, circuit-level tuning requires the addition of tunable electrical impedances and phase-shiters to the resonator-based oscillator [66-69]. As for the thermometer, simple resistive sensors have been used. Alternatively, the quality factor [70, 71] and the phase difference between two oscillators (one compensated while the other uncompensated) [72] have been employed as an indicator of the ambient temperature.

2.7.2. Ovenization and Power Consumption

Ovenization is based on the integration of a micro-heater within the resonator body so as to apply a controlled amount of thermal power to the resonator and raise its temperature to a specific constant value regardless of the ambient temperature fluctuation. The heater can be tightly integrated within the resonator body or placed around it (Figure 2.11). In both cases, the heater is shaped in the form of a serpentine in order to attain a large heater resistance within a limited area.

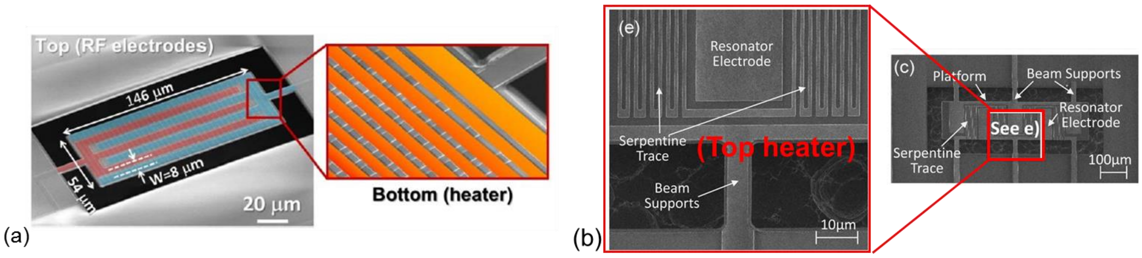

Figure 2.11: SEM images of ovenized resonators. The heater is placed (a) at the bottom layer [73] and (b) on the top layer [74].

Ovenization is especially suitable for MEMS resonators due to their small form factor, whereby power consumption can be dramatically reduced when compared to quartz crystal devices. The power consumption, P_{TH}, due to heat conduction is mostly due to heat flow escaping from hot area to cold area through the anchors (Figure 2.12) and is primarily determined by the anchors' thermal resistance, R_{TH}. P_{TH} can be calculated as,

$$P_{TH} = \frac{2\Delta T}{R_{TH}} \tag{2.38}$$

where ΔT is the maximum temperature change of the resonator with respect to ambient temperature. The factor of 2 is because two anchors are accounted for. The thermal resistance of the anchor is a function of the anchor geometry:

$$R_{TH} = \frac{l}{\sum_{i=1}^{3} k_i t_i w} \tag{2.39}$$

where l and w are the length and width of the beams, while k_i and t_i are the thermal conductivity and the thickness of the i-th layer (in this thesis: i = 1 for Al, i = 2 for AlN and i = 3 for Pt) in the stack. Since each layer's thickness is fixed for a specific fabrication process, in order to minimize the power consumption, the anchor is designed to be long and narrow and to have large thermal resistance. A few mW of power consumption are generally consumed for ovenization [64, 65, 73, 74]. This thesis will show that this 1 mW barrier can be reduced by properly engineering the anchor geometry and heater location.

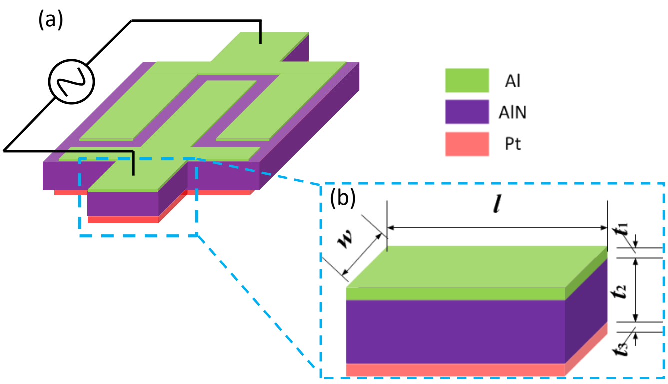

Figure 2.12: (a) A schematic representation of a 3-finger resonator where a piezoelectric layer is sandwiched between two metal layers. (b) A schematic representation of the supporting beam for piezoelectric MEMS resonators formed by a stack of two metals and a piezoelectric film.

2.7.3. Oven-based Feedback Control

The feedback control used to set the resonator temperature in ovenized devices has been implemented either through analog or digital techniques. One of the common analog feedback techniques is called constant-resistance-based control method (CRCM) [75-79], which uses a resistive temperature sensor to detect ambient temperature fluctuations and controls thermal power to set the sensor resistance to a constant value. However, this technique attains good compensation results only when an accurate knowledge of the sources of temperature fluctuations is available. Effectively, the designer should have clearly characterized temperature fluctuations in the resonator due to, for example, heat convention and radiation, non-uniform temperature distribution within the vibrating area of the resonator, nonlinear temperature sensitivity of the electronic circuitry, temperature difference between thermometers and resonators. Another analog feedback technique is the phase-lock-loop (PLL) based control method [72, 80]. The principle of PLL-based compensation method is to leverage the frequency difference between two oscillators (one passively compensated while the other uncompensated) as a feedback signal and control the thermal power to lock the frequency difference to a constant value. PLL-based feedback circuits can realize accurate temperature stability but its implementation is complicated and power-hungry. Finally, the digital feedback control loop utilizes a lookup table that contains the required thermal power values to maintain a target frequency for some sampled ambient temperatures [77, 79, 81]. For any given temperature, the digital temperature compensation method (DTCM) interpolates the lookup table and applies the calculated thermal power to the resonator. The advantage of DTCM over CRCM is that it agnostic of the source of temperature fluctuations and its implementation is straightforward.

CHAPTER 3: THERMAL MODULATION AND ITS APPLICATION IN FREQUENCY CONTROL

Micromachined aluminum nitride (AlN) contour-mode resonators (CMRs) are one of the MEMS resonator candidates which could overcome the drawbacks of bulky and non-integratable quartz crystal and surface acoustic wave (SAW) resonators. Because of their compact size, low cost, high frequency, compatibility with CMOS processes, and capability of spanning multiple frequencies on the same chip, AlN CMRs offer a promising path to the synthesis of reconfigurable local oscillators for radio frequency (RF) front-ends of next-generation.

The center frequency of uncompensated MEMS resonators is temperature dependent because material properties such as stiffness coefficients and density vary with temperature. Typically, AlN CMRs exhibit a temperature coefficient of frequency (*TCF*) of –25 ppm/℃ (which is equivalent to 3,000 ppm frequency shift over 120℃ temperature change) [48]. On one hand, this temperature dependency offers availability of a thermal-based frequency modulation method, which can be used to compensate unavoidable fabrication-induced frequency variations and facilitates their usage in timing references where frequency accuracy is rigidly required [82]. On the other hand, uncompensated MEMS resonators are vulnerable to temperature fluctuations and fail to meet the frequency stability requirement for modern wireless communication systems (< 50 ppm over a typical temperature range of −25℃ ~ 80℃ is demanded) [48] unless they are compensated.

.

Fortunately, surface micro-machining fabrication processes allow for direct integration of heaters adjacent to the resonators for highly efficient ovenization. Ovenization can be used to keep the resonator center frequency constant by modulating/tuning it via heat as the ambient temperature changes. This method is quite popular for implementing temperature compensation of resonators. The goal for ovenization is to minimize power consumption while keeping resonator performance unaffected. Research activities on ovenized MEMS resonators have shown that device heating from –40 to +80 ℃ requires only few mW of power. To enable the use of miniaturized frequency sources in truly disruptive applications such as in sensor nodes, pico-satellites or unmanned nano-air vehicles, sub-mW power consumption is required.

In this chapter, we first derive the trade-off between ovenization power and quality factor for piezoelectric MEMS resonators. Then we mitigate this trade-off and achieve sub-mW power by decoupling RF power delivery from the resonator supporting beams while maintaining high quality factor and ensuring uniform temperature distribution. Using these low-power resonators, we develop both analog and digital temperature compensation methods to address challenging issues that are faced by existing compensation methods and obtain high frequency stability for AlN CMRs.

3.1. Sub-mW Ovenization

The amount of power required for ovenization is mainly set by the thermal resistance of the suspensions that connect the resonators to the substrate. Efficient ovenization requires the use of support structures with high thermal resistance. In piezoelectric MEMS resonators, the supporting beams are generally formed by stacked layers of a piezoelectric material and metals used to apply an electric field across the device (Figure 2.12a and b). Without changing layer thickness, any increase in the thermal resistance (by using larger ratio of length to width) of the support structures shown in Figure 2.12b comes with an increase in the resistance in series, R_S, with the resonator motional resistance, R_M, ultimately causing a reduction in the loaded quality factor of the device, Q_{load}. This is formulated as:

$$Q_{load} = \frac{Q_{un}}{\left(R_S / R_M + 1\right)} \tag{3.1}$$

where Q_{un} is the unloaded quality factor of the resonator. For the support (anchor) configuration of Figure 2.12b, there is an inevitable trade-off between the power (P_{TH}) dissipated to ovenize the resonator and series resistance. Recall the expressions of P_{TH} and R_{TH} in Section 2.7.2:

$$P_{TH} = \frac{2\Delta T}{R_{TH}} \tag{2.38}$$

$$R_{TH} \approx \frac{l}{\sum_{i=1}^{3} k_i t_i w} \tag{2.39}$$

Since the series resistance is dominated by the routing of the top metal layer in the case of very low power of ovenization, R_S is given by

$$R_S \approx \frac{2l}{\sigma_1 t_1 w} \tag{3.2}$$

where σ_1 is the electrical conductivity of aluminum (top metal layer). Therefore, the product of P_{TH} and R_s is

$$P_{TH} \cdot R_s \approx \left(1+\alpha\right)\frac{4k_1}{\sigma_1}\Delta T \tag{3.3}$$

where $\alpha = \frac{k_2 t_2 + k_3 t_3}{k_1 t_1}$. It is interesting to note that, given a set of materials and thickness ratios, the right expression in Eq. (3.3) is constant. This leads to a trade-off between power consumption and series resistance (thus Q_{load}).

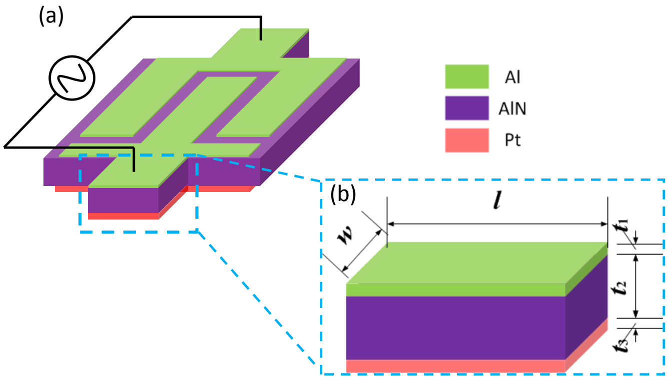

Figure 2.12: (a) A schematic representation of a 3-finger resonator where a piezoelectric layer is sandwiched between two metal layers. (b) A schematic representation of the supporting beam for piezoelectric MEMS resonators formed by a stack of two metals and a piezoelectric film.

To acquire a quantitative sense of the constant product, we substitute typical material thickness ($t_1 = t_3 = 100$ nm, $t_2 = 1$ μm) and material properties in Table 3.1 and obtain $\alpha = 9.3$. Furthermore, the Wiedemann-Franz law states that the ratio of thermal conductivity k to electrical conductivity σ is proportional to absolute temperature T_a, that is $k/\sigma = L_oT_a$, where L_o is *Lorentz number*. For aluminum, it is 2.09×10^{-8} WΩ/K^2. For the operation temperature range of interest, $\Delta T = 120$ K and $T_a \approx [80 - (-40)]/2 + 273 = 333$ K in the extreme case where the ambient temperature is –40 ℃. Therefore, we have

$$P_{TH} \cdot R_S \approx 34.4\,[\text{mW}\cdot\Omega] \tag{3.4}$$

The amount of degradation in Q_{load} depends on the target P_{TH} and the ratio of R_S/R_M, while R_M is estimated by

$$R_M = \frac{\pi^2}{8}\frac{1}{\omega_s C_0}\frac{1}{k_t^2 Q_{un}} \tag{2.17}$$

For the same resonator size (C_0) and figure of merit ($k_t^2 \cdot Q_{un}$), higher frequency resonators are more subject to the trade-off. As a rough idea, considering to ovenize the 221.6 MHz resonator presented in Figure 2.4 by 0.5 mW, the quality factor would be degraded by a factor of 1.81 (from

2100 to 1160), which is unacceptable. Even worse, the degradation factor is up to 8.25 (from 2100 to 255) for a 1 GHz device using the same configuration. Furthermore, to minimize power consumption in the oscillator circuit shown in Figure 2.7, it is desired to have small $R_S + R_M$.

Table 3.1: Material Properties used in the calculations [6], [18]-[19].

Material	Al	AlN	Pt
Thermal Conductivity [W/m·K]	94	80	71.4

It was also suggested to increase the thermal resistance by reducing the AlN layer thickness while maintaining similar ratio of anchor length to width and thus similar R_S [74]. However, thinner AlN layer tends to result in lower quality resonator and degrade Q_{un}. Sandia National Laboratories had explored such idea. It was found that, for each design, if the power is reduced, the Q is also degraded significantly. For example, for the data reported in Table 3.2, the design 1 with stack 1 (AlN layer thickness is 250 nm), consumes only 1.5mW to be ovenized but results in a Q of 183, which prevents it from being a useful resonator.

Table 3.2: Measured power consumption and quality factor at room temperature.

P = power required for 120 °C temp. change	Design1		Design2		Design3	
	P [mW]	*Q*	*P* [mW]	*Q*	*P* [mW]	*Q*
Stack1	1.47	183	5.62	527	8.44	239
Stack2	2.39	467	9.55	2241	14.62	1226
Stack3	2.53	591	16.40	3119	18.96	2336

3.1.1. Device Design and Fabrication

To eliminate the trade-off between power and quality factor, we decouple RF power delivery from the resonator's supporting beams, as shown in Figure 3.1-2. By doing this, we were able to independently design the geometry of the mechanical supporting structures (long but stiff serpentines) and RF paths (formed exclusively by a thin metal layer). The geometries of the suspensions of tested resonator are reported in Table 3.4, where *t*, *w*, and *l* are thickness, width, and estimated equivalent length of RF paths or supporting beams, respectively. Corresponding resonator body geometries are reported in Table 3.3.

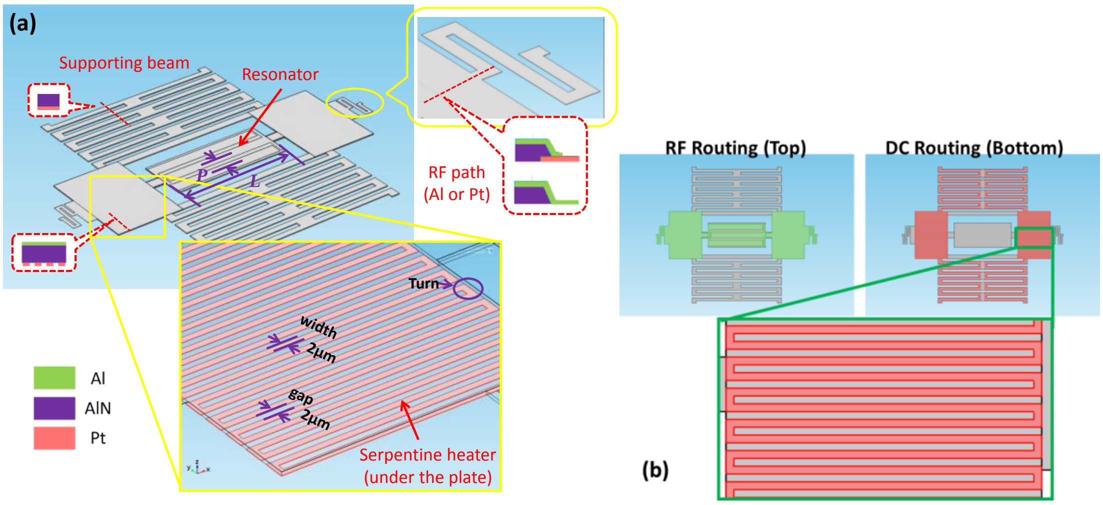

Figure 3.1: (a) Schematic representation of a low power ovenized resonator. Supporting beams are composed of AlN and Pt while the RF paths are composed of only a thin metal layer (AlN is completely removed). Pt serpentine heaters are placed under the rectangular plates. *L* is the length of the resonator and *P* is the electrode pitch. (b) RF and DC routing (green and red) are orthogonal and separated by an AlN layer where they cross (*i.e.* RF routing occurs in the top metal layer, whereas DC routing is done through the bottom metal layer). Inset shows the zoom-in view of the heater routing.

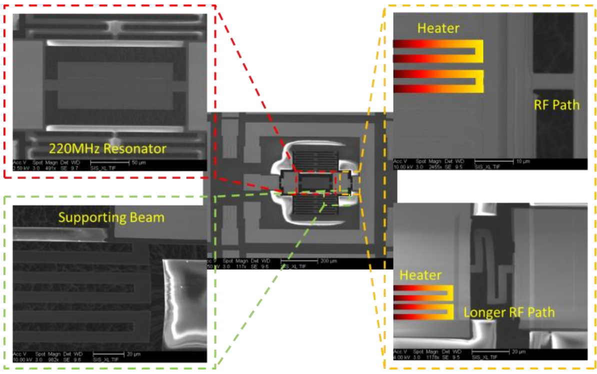

Figure 3.2: SEM pictures of a fabricated low power ovenized AlN resonator. Insets show zoomed-in views of the resonator, supporting structure, and 2 possible configurations of the RF path.

Table 3.3: Geometry of the ovenized resonators fabricated in this work. metal coverage is defined as the ratio of electrode metal width to pitch.

Device ID	Frequency [MHz]	L [µm]	P [µm]	Number of Electrodes	Metal Coverage
Res_70M	70	142	60	1	59/60
Res_220M Res_220M_2	220	142	20	3	7/10
Res_550M	550	142	8	7	5/8
Res_1160M	1160	142	4	15	1/2

For this resonator geometry, the product of P_{TH} and R_S becomes

$$P_{TH} \cdot R_S \approx (1+\beta)\frac{4k_1}{\sigma_1}\Delta T \tag{3.5}$$

where β is the ratio of the thermal resistance of the RF paths to that of the supporting beams. β can be set to be much less than α. Therefore, comparing Eq. (3.5) with (3.3), the former has a smaller product of P_{TH} and R_S. Quantitatively, for example, by substituting material properties in Table 3.1 and Device Res_220M_2's geometrical dimensions from Table 3.4, $1 + \beta = 1.5$ as compared to $1 + \alpha = 10.3$. This means that, while maintaining the same series resistance, the proposed ovenization method allows to lower the power consumption by $(1+\alpha)/(1+\beta) = 6.9$X. Furthermore, we are free to optimize suspensions' dimensions to obtain larger $(1+\alpha)/(1+\beta)$. Nonetheless, from Eq. (3.5), it is clear that to attain high Q_{load} (>1000) there are some constraints on the maximum value of the series resistance, R_S. Thus, there is a limit on the lowest power consumption that could be attained. Similarly, there exists a minimum value of the total thermal resistance (the thermal resistance of RF paths in parallel with that of supporting beams) that we should implement in order to ensure sub-mW power consumption. Keeping these constraints in mind, we designed resonators with different frequencies, RF paths and supporting beams, as listed in Table 3.4.

Table 3.4: Geometry of tested Resonators' RF Paths and Supporting Beams and corresponding theoretical thermal resistance.

Device ID	Res_70M Res_220M		Res_550M Res_1160M		Res_220M_2	
Suspension type	RF path	Supporting beam	RF path	Supporting beam	RF path	Supporting beam
Material	Al	AlN/Pt	Al	AlN/Pt	Al	AlN/Pt
Num. n	2	4	2	4	2	4
t[µm]	0.1	1/0.1	0.1	1/0.1	0.1	1/0.1
w[µm]	4	7/6	4	7/6	4	3/2
l[µm]	57	800	98	800	28.5	800
turns	2	8	2	8	2	8
Theoretical R_{TH} [K/mW]	758	332	1303	332	379	787

Beyond the supports, it is important to note that equal attention was placed in the design of the heaters. Two identical heaters formed by 2 µm wide Pt serpentines separated by a 2 µm gap, were placed symmetrically under two rectangular plates connected to the central body of the resonator. The serpentines were formed by a total of 29 turns each and had an effective length of 2458 µm (see Figure 3.1). The use of a symmetric configuration ensures attaining a uniform temperature distribution across the resonator body. This concept was verified via finite element methods. Figure 3.1 shows the geometry of Device Res_220M as modeled in commercially available finite element analysis (FEA) software, COMSOL. Figure 3.3 shows the resonator's temperature distribution given a certain voltage (1.2V) applied to the heater by the stationary solver. The uniformity of the temperature distribution over the resonator body is evident. More importantly, the temperature difference within each rectangular plate is less than 0.7 ℃. This allows temperature sensors to better represent the resonator temperature and thus enable higher frequency stability. Although it is possible to separate the heaters from the temperature sensors, in the particular implementation of this work the heaters were also used as sensors.

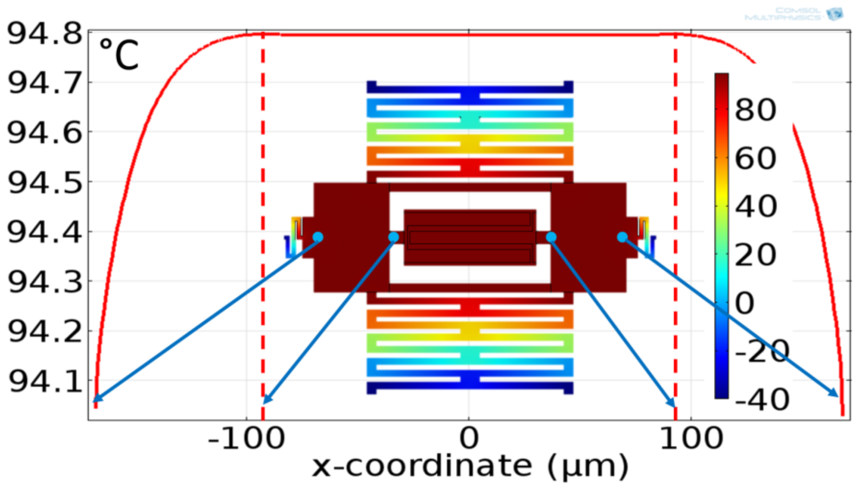

Figure 3.3: COMSOL FEA of temperature distribution in the Device Res_220M when a fixed voltage is applied to the heater. The simulation uses the *Joule Heating* module. Linearized resistivity (a built-in model for the variation of conductivity with temperature) for bottom Pt heater was set. Ambient temperature boundary conditions were imposed at the end surfaces of the supporting beams and RF paths, and ground and electrical potential boundary conditions were applied to the two ends of the heater. The geometry is meshed with 61,147 elements (predefined fine size) combining tetrahedral elements (to mesh AlN layer) and prism elements (to mesh thinner metal layers). The stationary solver occupies no more than 1.15GB of memory and converges within 4 minutes on a PC configured with a 3.2 GHz CPU.

Finally, we copied two serpentine supporting beams and placed them on both sides of the resonator. The serpentines will be used as dummy resistors (Figure 3.4) for the purpose of implementing the circuit for temperature compensation. The function of the dummy resistors will be explained in details in Section 3.2.1.

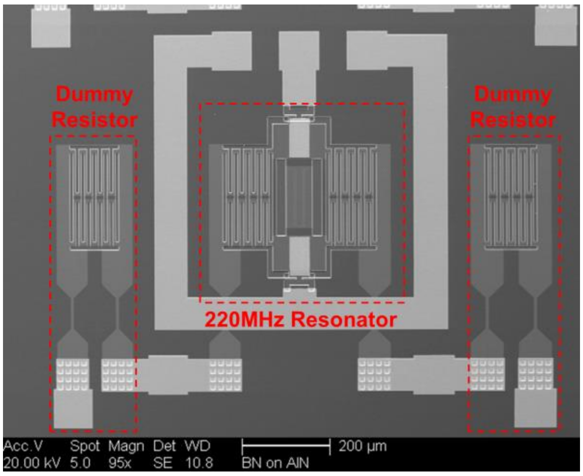

Figure 3.4: SEM image of the top view of a fabricated low power ovenized resonator (before release) and two dummy resistors placed symmetrically on the left and right side. The function of dummy resistors is explained in Section 3.2.1.

The ovenized resonators of this work can be manufactured in a four-mask post-CMOS-compatible microfabrication process, as shown in Figure 3.5. This is the same process used for the making of devices without ovenization (Figure 2.6), effectively showing that ovenization can be attained without additional complexity in the manufacturing of the resonator. A distinguishing feature of the fabrication process was the use of the via opening step to remove AlN from the suspensions and access the bottom electrode. Thanks to the gradual slope of the via openings' sidewalls, the top Al layer was used to contact a patterned bottom Pt film (②-Pt RF path in Fig. 6) or to directly bridge the gap between the heater plates and the substrate (⑤-Al RF path in Fig. 6).

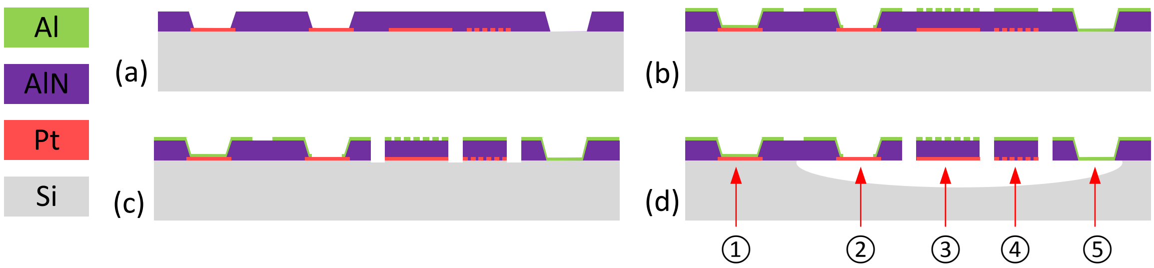

Figure 3.5: Four mask fabrication process: (a) sputter deposition and patterning of Pt and AlN layers, and via openings; (b) sputter deposition and pattering of top Al layer; (c) dry etching of AlN in Cl_2-based chemistry; (d) XeF_2 dry release of the AlN resonator. ① via to the serpentine pads, ② Pt RF path, ③ resonator, ④ serpentine heaters, ⑤ Al RF path.

3.1.2. Results and Discussion

We measured the electrical (admittance vs. frequency) and thermal (TCF and power dissipation of heater) characteristics of the ovenized resonators in an RF probe station. The electrical measurements were conducted in an RF lakeshore probe station (Model CRX-VF), in which temperature (varied between –35 ℃ and +85 ℃) and pressure (fixed at ~1×10^{-8} Torr unless specified) could be controlled. We obtained the resonators' TCF by sweeping temperature and measuring the corresponding frequency shift. We also monitored how the resonator frequency changes versus the applied heater power (Figure 3.6) by sweeping the ovenization power at a fixed temperature. Consequently, we were able to extract the thermal resistance for each resonator. Under high vacuum (~1×10^{-8} Torr), the maximum power required to change the temperature from –35 ℃ to +85 ℃ of the resonators is about 10X smaller than what is required in [73]. The 1.16 GHz resonator only consumes 353 μW – the lowest ever recorded for MEMS resonators. Nevertheless, the use of a device with a higher thermal resistance and mass inevitably increases its thermal time constant. Through simulations, we have estimated it to be around 28 msec. Although slower than prior implementations [73], it is sufficient to respond to environmental temperature changes.

Interestingly, as shown in Table 3.5, this ovenization technique is broadly applicable to resonators of different frequencies. Furthermore, we experimentally verified that high *Q*s can be attained in these resonators. It is important to note that the k_t^2 of this device is slightly lower than what reported in [20], in which a similar resonator without heaters is described. The slight degradation in k_t^2 is due to the overlap between the top RF signal path and the bottom heater, as shown in Figure 3.1b. This overlap introduces a feedthrough path (mainly capacitive) from the signal to the ground, which effectively appears in parallel with the resonator. However, it is possible to envision ways to reduce the overlap by resorting to higher resolution lithography and dramatically shrinking the size of the heaters while attaining the same resistance.

Table 3.5: Performance of Low Power Ovenized Resonators. *Q* and k_t^2 are Extracted at Room Temperature.

Device ID	Freq. [MHz]	Q	k_t^2 [%]	TCF [ppm/K]	R_{TH} [K/mW]	Max. Pwr. [μW]
R4C4_R4C1	70	2774	1.02	-26.85	224	537
R4C4_R5C6	220	4459	0.54	-25.96	223	538
R5C4_R6C6	550	3959	1.03	-24.80	278	431
R5C4_R7C4#	1160	1247	1.08	-24.69	340	353

the heater sits right under resonator body for this device under test.

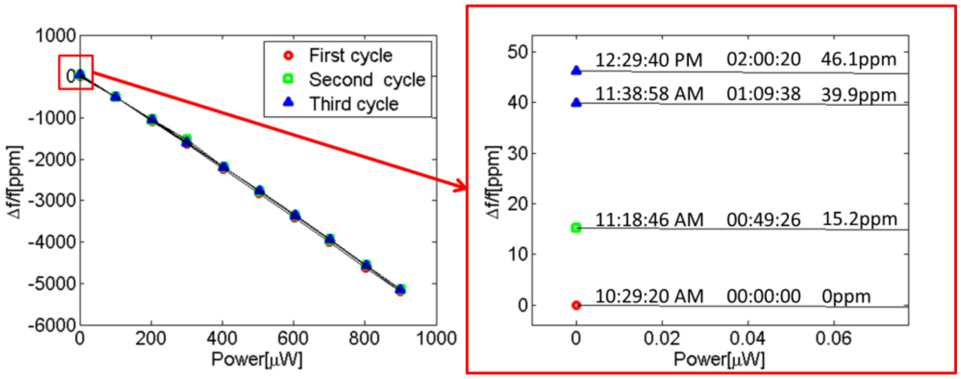

Figure 3.6: Measured frequency shift versus applied power in a Lakeshore vacuum probe station for a 220 MHz resonator. Inset shows the zoom-in view of resonator aging when no power is applied to the heater. It is interesting to note that the resonator aging is not linearly dependent on the elapsed time.

Table 3.6: Power Consumption of a 70 MHz Resonator versus Pressure.

Pressure [Torr]	Freq. Drift ppm/μW	Temperature Rise Factor [°C/mW]	Max. Power [μW]
5×10^{-1}	-2.13	79	1513
3×10^{-2}	-5.29	197	609
8.5×10^{-6}	-5.90	220	546
$\sim1\times10^{-8}$	-5.97	224	537

It is important to point out that due to a relatively large surface area, heat convection and conduction through air turn out to be significant for this class of ovenized resonators. Table 3.6 shows the dependence of power consumption on pressure for a 70 MHz resonator. It also indicates that 30 mTorr (a typical pressure for wafer level packaging) is low enough to attain sub-mW power consumption.

3.2. Analog Compensation

An oven-controlled MEMS resonator consists of a heater integrated with the resonator and an active control circuit to manipulate oven power in response to ambient temperature changes. Beyond obtaining high temperature stability, the main objective in the design of ovenized resonators is to minimize the power dissipated by the heater and the control circuit. The heater power consumption has been discussed in Section 3.1. The power consumed in feedback circuits to actively control the ovenization process is determined by the circuit design (see Table 3.7) [72, 75-77, 79, 80]. Two main types of analog circuits have been investigated: phase lock loop (PLL)-based circuits and constant-resistance-based feedback. For example, a simple PLL-based compensation method takes advantage of the difference in TCFs between two oscillators (one passively compensated and the other uncompensated) as a temperature indicator and uses feedback to adjust the thermal power in the resonator so that the frequency difference is nulled [72]. PLL-based feedback circuits can achieve high frequency stability but require complex circuit design and are power-hungry; for example, 10 to 13 mW are consumed in [72]. Constant-resistance-based feedback uses a resistive temperature sensor to detect ambient temperature variations and adjusts thermal power to set the sensor resistance to a constant value [64, 76, 77, 79, 83]. This approach generally consumes less power than a PLL, but current circuit designs based on constant resistance feedback often involve more than one operational amplifier and can result in additional power consumption, typically 2 to 20 mW per amplifier.

Table 3.7: Comparisons of This Work to the State-of-the- Art.

	[75]	[80]	[76],[84]	[77]	[79]	[72]	This work
Year	2015	2015	2015	2014	2012	2009	2015
Device Type	Capacitive Resonator	Piezoelectric-on-silicon Oscillator	Piezoelectric Oscillator	Fused Silica Oscillator	Piezoelectric Oscillator	Capacitive Oscillator	Piezoelectric Resonator
Circuit Type	Constant Resistance Feedback	PLL	Constant Resistance Feedback	Constant Resistance Feedback	Constant Resistance Feedback	PLL	Constant Resistance Feedback
TCF After Material Compensation	+5.1 ppm/℃	+5 ppm/℃	0ppm/℃ @turnover temperature	No	No	No	No
$\Delta f/f$ After Ovenization	120 ppm	11 ppm	300 ppb	1050 ppm	125 ppm	2 ppm	< 100 ppm
$\Delta f/f$ Reduction for Ovenization	5.3X	50X	100X	8.9X	28X	704X	>27.8X
$\Delta f/f$ Digital calibration	No	No	No	11 ppm	2 ppm	0.1 ppm	No
Ovenization Power	0.47 mW	8.15 mW	12.5 mW	15.8 mW	9 mW	14.9 mW	0.53 mW
Max. Total Power	N/A	N/A	31 mW	N/A	N/A	137 mW	3.8 mW
Temperature Range	-40~85 ℃	-40~70 ℃	-40~85 ℃	-40~65 ℃	-45~85 ℃	-20~80 ℃	-35~85 ℃

Finally, few approaches have considered the adverse effect of temperature gradients along the routings that connect the oven to the substrate. This routing resistance degrades the accuracy of the sensor used to read the resonator temperature and thus significantly impairs its frequency stability.

3.2.1. Temperature Compensation Circuit Design

The compensation circuit is comprised of two parts: a modified Wheatstone bridge with dummy resistor and a differential RC integrator, as schematically represented in Figure 3.7. This circuit is classified as a constant-resistance-based feedback. In the modified Wheatstone bridge, $R_{1\text{-}3}$ are off-chip constant resistors with R_1 equal to R_2. The temperature coefficient of resistance (TCR) of these resistors does not have a significant impact on the oscillator frequency stability. As long as R_1 and R_2 share the same TCR and the TCR of R_3 is less than 0.325 ppm/ ℃ (readily available commercially), the oscillator would exhibit a frequency instability < 0.25 ppm over 120 ℃. R_{dummy} is the on-chip dummy resistor, which has the same geometry of R_{h1} and R_{h3}. The constant resistor, R_3 , can be seen as formed by two separate constant resistors in series, R_{31} and R_{32}, which are respectively set to be equal to R_{h1} and R_{h2} at the target oven operating temperature, T_m. R_{h2} is the heater as shown in Figure 3.1and also works as a sensor in the same circuit. T_m is set to be slightly higher than the maximum environmental temperature in which the device is required to work (85 ℃ was considered in this work). The differential RC integrator integrates the voltage difference between V_3 and V_h over time to output a voltage, V, which is fed back to the Wheatstone bridge. Given an arbitrary ambient temperature T_0 ($\leq T_\mathrm{m}$), the output voltage V increases until the voltage difference between V_3 and V_h nulls, which is the equilibrium status of the compensation circuit. This means that (given R_1 equal to R_2), we need to have

$$R_{h1} + R_{h2} + R_{h3} = R_{31} + R_{32} + R_{dummy} \tag{3.6}$$

Based on COMSOL FEA (Figure 3.3), the temperature distribution along the supporting beams and within the rectangular plates can be simplified to be linear and uniform, respectively, as shown in Figure 3.8. To highlight the importance of the dummy resistor in ensuring high frequency stability, let us consider what happens to the temperature distribution in the resonant structure when the ambient temperature changes from T_{01} to T_{02} ($T_{02} < T_{01} \leq T_m$) and no dummy resistor, R_{dummy}, is present (see Figure 3.8). Considering the resistivity of the metal layers to be directly proportional to temperature changes, then the plot in Figure 3.8 also represents changes in resistivity along the heater traces. As the thickness and width of the Pt heaters are considered unchanged, the area under the curves in Figure 3.8 (effectively the product of resistivity times length) is proportional to the electrical resistance associated with the sensors/heaters in the 3 main regions where temperature changes are recorded (labeled R_{h3}, R_{h2}, and R_{h1} in Figure 3.8). The plot can then be used to readily explain what happens to the temperature distribution in the device as the equilibrium condition is enforced.

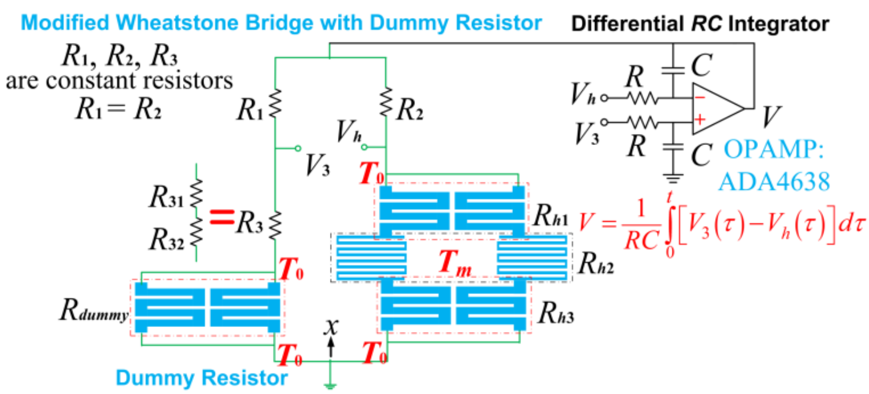

Figure 3.7: Schematic representation of the temperature compensation circuit formed by a modified Wheatstone bridge with a dummy resistor and a differential RC integrator.

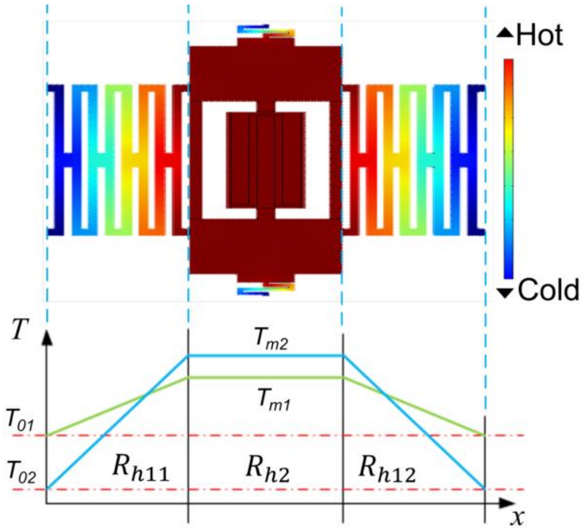

Figure 3.8: Schematic representation of a possible temperature distribution change of an ovenized resonator when no dummy resistor is present and the ambient temperature varies from T_{01} to T_{02}. The temperature distribution is simplified to be linear along the supporting beams and uniform (T_{m1} and T_{m2}) within the rectangular plates.

In the absence of the dummy resistor, the feedback circuit forces the total heater resistance R_h ($=R_{h1} + R_{h2} + R_{h3}$) to be constant because R_3 is constant. As conceptually represented in Figure 3.8, when the temperature changes from T_{01} to T_{02}, R_{h3} and R_{h1} decrease, hence R_{h2} must increase in order to maintain R_h constant. This means that the resonator temperature will increase from T_{m1} to T_{m2} ($T_{m1} < T_{m2}$),

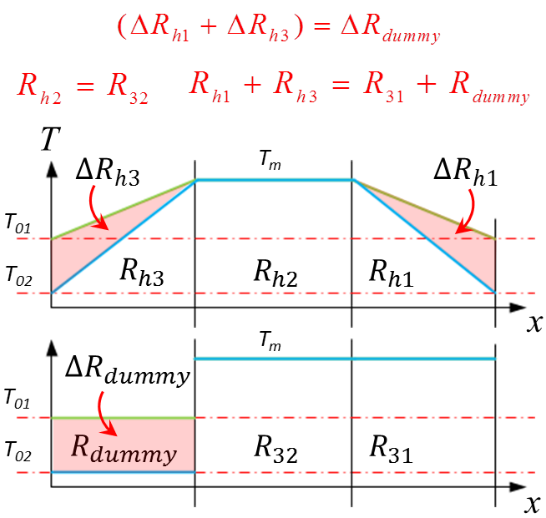

Figure 3.9: Schematic representation of resonator temperature distribution change with modified constant resistance feedback under different ambient temperatures (top) and temperature distribution change of dummy

resistor and off-chip resistor (bottom). Here, we treat the constant resistor R_{31} as if it was a chip resistor that shares the same geometry as R_{h1} but always immersed in the temperature of T_m. Similar treatment applies to R_{32}.

This temperature distribution is due to the fact that no additional constraints exist beyond Eq. (3.6). Because of this, the resonator temperature (middle region of the plot) is not constant over ambient temperature, hence clearly resulting in frequency fluctuations.

However, when the dummy resistor is included, the temperature distribution in the resonant structure and the suspensions changes to the one of Figure 3.9. Thanks to the introduction of the dummy resistor, it is possible to ensure that changes in resistance in the leg of the Wheatstone bridge between V_3 and ground are equal to those occurring in the leg where the resonator heaters are placed:

$$\left(\Delta R_{h1} + \Delta R_{h3}\right) + \Delta R_{h2} = \Delta R_{dummy} \tag{3.7}$$

where ΔR_z represents the resistance change of R_z from T_{01} to T_{02}, and z can be any subscripts in Eq. (3.7). Note that $R_{31} + R_{32} = R_3$ is approximated to be constant over temperature (see initial assumption about *TCR* of these resistors, which is approximately 3 orders of magnitude lower than the *TCR* of the heater). Again using the plot in Figure 3.9, it is evident that in order to satisfy Eq. (3.7), T_{m1} has to be equal to T_{m2}, which is equivalent to state that:

$$\Delta R_{h2} = 0 \tag{3.8}$$

Combining this condition with the initial equality between R_{h2} and R_{32} at the temperature T_m, we obtain that

$$R_{h2} = R_{32} \tag{3.9}$$

is satisfied for any given ambient temperature T_0. Therefore, the plate temperature stays at a fixed desired temperature, T_m, and so does the resonator.

Obviously, subtracting Eq. (3.6) by (3.9), we obtain that

$$R_{h1} + R_{h3} = R_{31} + R_{dummy} \tag{3.10}$$

is also satisfied for any given ambient temperature T_0. This equation offers a different perspective in understanding the function of the dummy resistor. That is, the dummy resistor together with a part of R_3 cancels out the routing resistance under the supporting beams. In other words, the adverse effect of temperature gradients along the routings is eliminated and thus the accuracy in sensing the resonator temperature is improved.

In summary, in the compensation circuit, the dummy resistor is indispensable to ensure high temperature stability. It is worth noting that, although only one of the two dummy resistors of Figure 3.4 is used in the circuit, the other resistor is designed to maintain geometrical symmetry and thus symmetrical temperature distribution across the chip.

The previous constraints define the values of all the resistors forming the Wheatstone bridge. R_{h2} has to be much larger (5X) than R_{h1} and R_{h3} to minimize the power dissipation in the supporting beams and thus validate the assumption of linear temperature distribution. R_1 and R_2 should be close to R_h in order to maximize the sensitivity of the Wheatstone bridge to temperature variations. The set-point resistance, R_3, should be set to a value larger than $R_h - R_{dummy}$, so as to ensure that the resonator operates at a temperature higher than 85 ℃. The larger R_3, the higher the resonator temperature. For the sake of lowering power consumption, R_3 should be set to be the lowest value allowed by the specific application (*i.e.* a value which corresponds to a temperature slightly above the required maximum operating temperature).

We used COMSOL to verify the analysis of the compensation circuit and resulting resonator temperature stability. The geometrical model and boundary conditions are shown in Figure 3.10. Meshing was setup similarly to what is described in Figure 3.3. This COMSOL simulation only considered the heat conduction along the supporting beams and RF paths and enabled us to extract resonator temperature and resistance of both the heater, R_h, and the dummy resistor, R_{dummy}

as the ambient temperature was varied. The overall verification process consists in varying the applied current, I_{app}, until ($R_h - R_{dummy}$) is equal to the set-point resistance, R_3. The tolerance error for this recursive solution was set to be < 0.1 Ω. The set-point resistance, R_3, was set to be equal to ($R_h - R_{dummy}$) when the ambient temperature is set to be T_m (for example, 90 ℃) and a very small I_{app} (for example, 1 μA) is applied. For every iteration, the resonator's equilibrium temperature is recorded. The procedure is repeated for different ambient temperatures, T_0.

The above verification process via COMSOL shows that the overall resonator temperature fluctuation is reduced to 0.13 ℃ over the temperature range of –35 ℃ to +85 ℃. Therefore, the frequency fluctuation is reduced to be around 3.15 ppm, as shown in Figure 3.11, when assuming an uncompensated TCF of –25 ppm/℃. This result amounts to an oven gain (which is defined as the ratio of the change in ambient temperature to the corresponding change in the ovenized resonator's temperature) as high as 923. However, when including the radiation with emissivity of 1, the total frequency fluctuation is 7.95 ppm and the oven gain is 377.

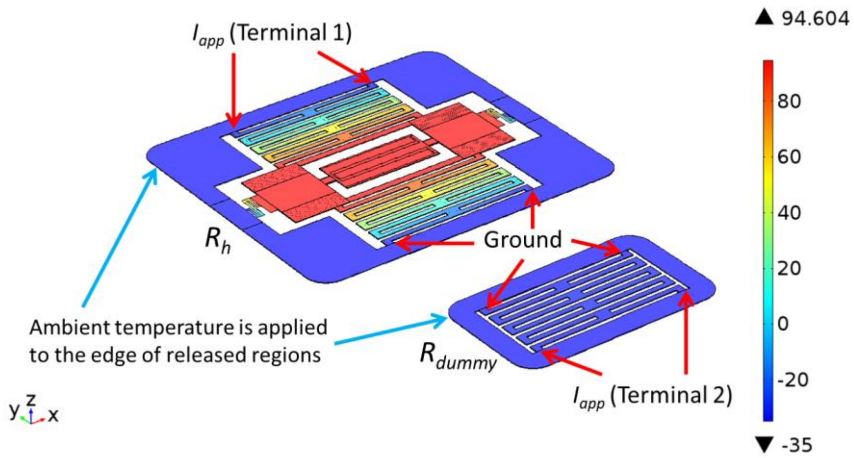

Figure 3.10: Schematic representation of COMSOL FEA setup used to verify the analysis of the compensation circuit. The boundary conditions include ambient temperature at the edge of released regions, two terminals to apply currents at one end of the heater and the dummy resistor, respectively, and two grounds at the other ends. Linearized resistivity for bottom Pt was also set up in the model.

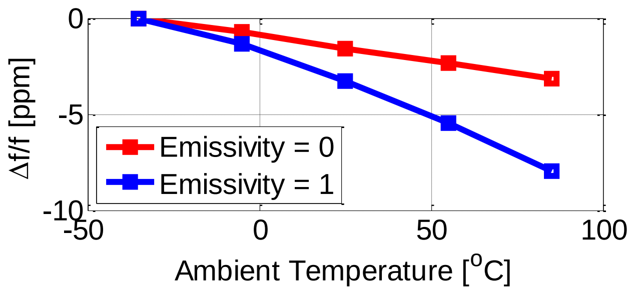

Figure 3.11: Plot of simulated $\Delta f/f$ versus ambient temperature after constant resistance- based feedback temperature compensation with and without surface-to-ambient radiation. f at -35 ℃ is chosen as the reference frequency.

The simulation did not include the impact of temperature-induced strain on frequency. Nonetheless, our analysis shows that the effective strain due to temperature along the direction of vibration is less than 1 μ strain, which would have an insignificant impact on the frequency shift.

3.2.2. Results and Discussion

The performance of the temperature compensation circuit was characterized by using the setup schematically shown in Figure 3.12. A specific resonator, Res_220M_2, was selected to validate the temperature compensation circuit. The chosen resonator was mounted inside the vacuum chamber (pressure set at 5.2×10^{-8} Torr) of the same RF lakeshore probe station used to characterize the standalone resonators, whereas the circuit was placed outside the chamber to eliminate circuit dependence on temperature and validate our analysis. Inside the chamber, an RF probe connected to a network analyzer monitored the frequency shifts of the device admittance. The frequency at which the admittance response exhibited a maximum was taken as the resonant frequency of the device under test. Simultaneously, three DC probes connect the heater, R_h, and the dummy resistor, R_{dummy}, to the temperature compensation circuit outside the chamber. In the circuit, the heater resistance, R_h, and the dummy resistance, R_{dummy}, were respectively equal to 1852.3 Ω, and 275.9 Ω at 85 ℃. The set-point resistance R_3 was set to be 1599.7 Ω, a value larger than $R_h - R_{dummy}$, so as to ensure that the resonator operates at a temperature higher than 85 ℃. We monitored ovenization power, total compensation power, and resonator frequency, as we sweep the chamber temperature from –35 to 85 ℃ in incremental steps of either 20 ℃ (from –35 to 5 ℃) or 40 ℃ (from 5 to 85 ℃). The maximum ovenization power occurred at the minimum temperature of -35 ℃. Since the dummy resistor at the temperature of –35 ℃ is R_{dummy} = 213.5 Ω, and the voltage across the heater, V_h , is measured to be 0.978 V, the maximum power for ovenizing the resonator is 527.5 μW. The amplifier was connected to a 3 V supply and the total power consumed by the circuit was 3.8 mW. We expect to further lower power consumption by using integrated circuits based on scaled technology nodes that use lower supply voltages. By changing the chamber temperature from –35 to 85 °C, we measured the resonator's center frequency with and without the temperature compensation circuit on, as shown in Figure 3.13. The total frequency drift $\Delta f/f$ is less than 100 ppm, when the compensation circuit is turned on (vs. 2775 ppm when it is off). Compared to other work (see Table 3.7), this demonstration shows the least power consumption with a good oven gain of 27. In addition, from Table 3.8, we can conclude that the temperature compensation does not significantly affect the resonator's performance, namely Q and k_t^2.

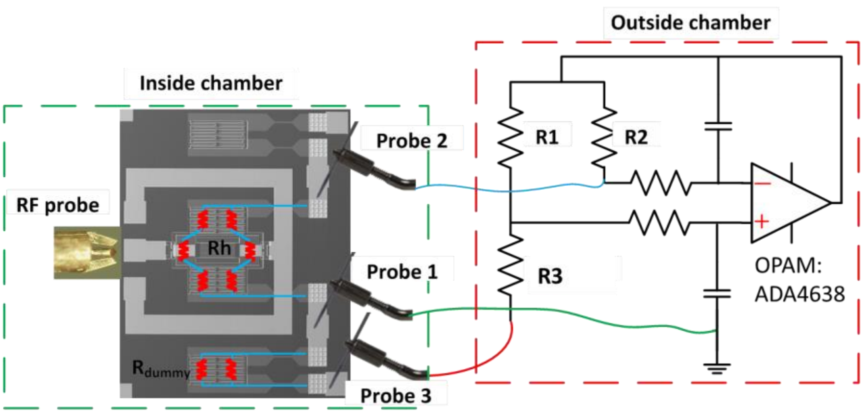

Figure 3.12: Schematic representation of the experimental setup for temperature compensation. The resonator under test is mounted inside the vacuum chamber of an RF Lakeshore probe station, while the temperature

compensation circuit is kept outside. The device and the circuit are connected via three DC probes. The resonator center frequency is monitored by a network analyzer (not shown in the picture).

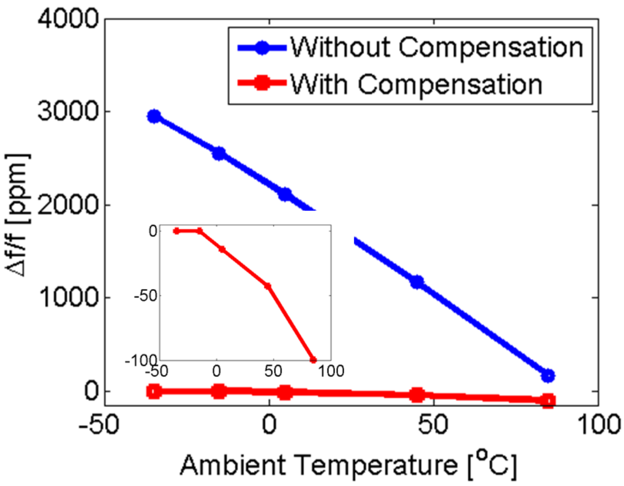

Figure 3.13: Resonator frequency variations versus ambient temperature with and without compensation. The plot uses the resonator's compensated frequency at -35 ℃ as the reference value. Inset shows zoomed-in view of frequency drift trend after compensation over the ambient temperature sweep.

Table 3.8: Comparison of Resonator performance between with and without Temperature Compensation for a 220 MHz Resonator.

Sample stage temperature	*fs*[MHz] w/o comp.	Δ*f*/*f*[ppm]	*Q*	k_t^2		*fs*[MHz] w/ comp.	Δ*f*/*f*[ppm]	*Q*	$k_t^2(\%)$
238K/-35ºC	219.7313	0	4076	0.78		219.0844	0	3540	0.77
258K/-15ºC	219.6438	-398	4081	0.76		219.0844	0	3539	0.77
278K/5ºC	219.5472	-834	3775	0.79		219.0813	-14	3492	0.79
318K/45ºC	219.3397	-1782	3568	0.77		219.0750	-43	3450	0.78
358K/85ºC	219.1216	-2775	3581	0.79		219.0625	-100	3469	0.80

Nonetheless, the oven gain extracted from the experiment is significantly smaller than what expected from simulations (27 versus 377). The authors believe that this discrepancy can be attributed to the aging of the resonator. The whole measurement took more than 6 hours to complete. Figure 3.6 shows a 46.1ppm frequency drift (resonator aging) over 2 hours, hence supporting that aging could be the major source of discrepancy between experiments and theory.

3.3. Digital Compensation

We have previously introduced two analog compensation techniques: constant-resistance-based control method (CRCM) and phase-lock-loop (PLL) based control method. The first one requires an accurate knowledge of the sources of temperature fluctuations, such as heat convention and radiation, non-uniform temperature distribution within the active area, nonlinear temperature sensitivity of the electronic circuitry, temperature difference between thermometers and resonators. The second analog method can overcome these drawbacks, since it directly compensates oscillator frequency rather than resonator temperature such that it can realize accurate temperature stability. However its implementation is both complicated and power-hungry.

Fortunately, the digital temperature compensation method (DTCM) with look-up tables can hold the same advantages of PLL-based method. DTCM is straightforward and power-efficient. A lookup table contains the required thermal power values to maintain a target frequency for some sampled ambient temperatures. For any given temperature, the digital temperature compensation method (DTCM) interpolates the lookup table and applies the calculated thermal power to the resonator. Nonetheless, in order to obtain precise temperature compensation, for example, 15 ppm/120 ℃, each data point (thermal power versus ambient temperature) of the lookup table should be attained in a well-stabilized temperature chamber (±0.3 ℃, at most, fluctuating around the set-point temperature when taking AlN CMRs for instance). Practically, it takes a long time (tens of minutes) for a temperature chamber to stabilize. What's worse, such method requires multiple sets of calibration data if different target frequencies are needed.

In this thesis, we propose and demonstrate the application of artificial neural network based digital temperature compensation method (ANN-DTCM) for AlN CMRs. ANN is a universal powerful data analysis tool, which has been widely used in finance, education, medical science, computer vision, and many other domains. Particularly for AlN MEMS resonators, it has been demonstrated to predict fast and accurately the probability of having spurious modes [85]. An

ANN is constituted by a number of neurons and is typically feed-forward connected by weighted synapses. The principle of ANN is to generalize rules stored in synaptic weights from limited observed instances through a training/learning process without task-specific programming. The generalized rules are used for prediction of new instances. By feeding measurement data of resonators to an ANN to train its synaptic weights, the ANN maps the resonator frequency to the ovenization power and the ambient temperature. In this way, ANN-DTCM delivers a compensation method that is agnostic about the physical source of temperature-induced frequency fluctuations, performs rapid calibration (>10X faster than conventional DTCM with look-up tables), and results in low power consumption. Our ovenized resonator employed in this demonstration is shown in Figure 3.14a (which is the same as Figure 3.2). The measured *TCF* for the resonator under test is –23.1 ppm/℃. In addition, there is an on-chip platinum temperature sensor (which is not shown in Figure 3.14a) far away from the resonator to minimize the effect of ovenization on ambient temperature readout. The sensor sensitivity is 2.7 Ω/℃ (Figure 3.14b).

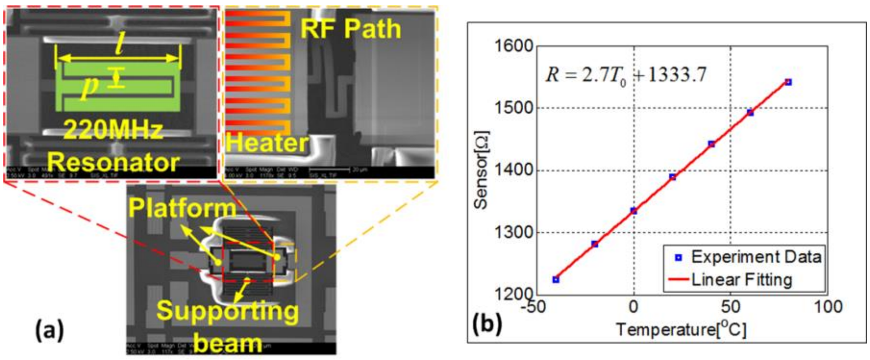

Figure 3.14: (a) The SEM image of a 220 MHz resonator that can be ovenized with extremely low power (390 µW/120 °C). Insets show zoomed-in views of the resonator and RF signal path. *p* is the pitch, which determines the resonator frequency, and l is the resonator length. The thermal resistance of the supporting beams and RF signal paths determines the ovenization power. (b) Plot of measurement data and linear fitting of the sensor resistance versus temperature.

3.3.1. ANN-DTCM Implementation

The implementation of the ANN-DTCM is based on 4 steps: i) calibration data collection, ii) ANN training, iii) generation of lookup tables, and iv) ANN-DTCM testing (see Figure 3.15).

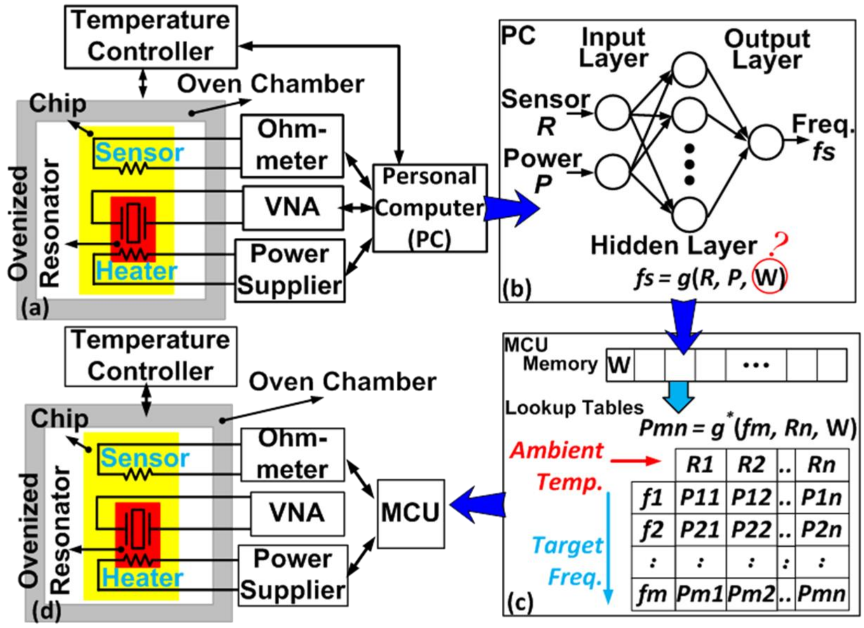

Figure 3.15: Schematic representation of the ANN-DTCM calibration and testing procedure. (a) Block diagram representation of the calibration data collection process. The red area stands for the ovenized resonator (Fig. 1), while the yellow box represents the tested chip. (b) The calibration data are used to train a 2-Input-n-hidden-1-output artificial neural network (ANN). The training process determines the optimum weight matrix, W. (c) The W matrix is downloaded to a micro-controller-unit (MCU) and then a lookup table for multiple target frequencies is generated. (d) Block diagram representation of the ANN-DTCM system and the corresponding test setup.

A. Calibration Data Collection

As shown in Figure 3.15a, the ANN-DTCM relies on automatic data collection for calibration. A personal computer (PC) sets different chamber temperatures via a temperature controller. For each temperature, a power supply is controlled to vary the ovenization power, P_{TH}, to the heater integrated with the resonator (Figure 3.14a). After 5~10 times the resonator's thermal time constant (estimated to be < 1 second in this work), the resonator's center frequency, f_s, and the real-time ambient temperature (which fluctuates around the set-point temperature and is represented by the on-chip sensor resistance, R) are monitored by the vector network analyzer

(VNA) and the ohmmeter, respectively. Each set of the collected data contains *R*, *P*, and f_s. It is worth noting that the temperature chamber's fluctuation period is about three orders of magnitude larger than the resonator's thermal time constant. Therefore, the resonator temperature follows the fluctuation of the ambient temperature such that their difference is constant given a certain amount of thermal power.

B. ANN Training

The calibration data are used to train a 2-input-*n*-hidden-1-output feedforward ANN (Figure 3.15b). The number of hidden layer's neurons, n, is chosen to be 20. The larger the number, the more complex problem ANN can address, but the more time it takes to train [86]. Except for the input neurons, each neuron first computes a linear combination of its inputs $\{x_j\}_{j=1\ldots M}$, then applies an activation function to the result, as shown in Figure 3.16. The neuron's output *y* can be formulated as

$$y = \sigma\left(b + \sum_{j=1}^{M} w_j x_j\right) \tag{3.11}$$

where $\{w_j\}_{j=1\ldots M}$ are neuron's synaptic weights, which represents the strength of connections between neurons, *b* is the neuron's bias, and $\sigma(\cdot)$ is an activation function. In this work, $\sigma(\cdot)$ is a *TanSig* function, $TanSig(x) = \frac{1-\exp(-2x)}{1+\exp(-2x)}$, for the hidden layer's neurons, and is a *Purelin* function, *Purelin*(*x*) = *x*, for the output layer's neuron.

The training process determines the optimum synaptic weights, which can be represented by a matrix, **W**. In this work, we employed Bayesian regularization backpropagation algorithm, which is inbuilt in MATLAB Neural Network Toolbox [87], to train the weight matrix. After training, a relationship that predicts f_s as a function of R, P, and $\mathbf{W}$ is established (Figure 3.17a).

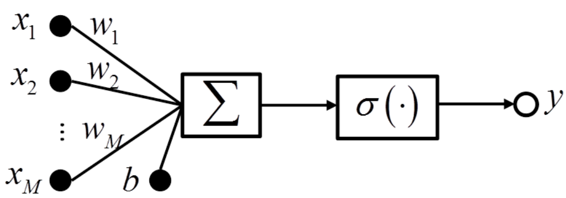

Figure 3.16: Diagram of a neuron unit.

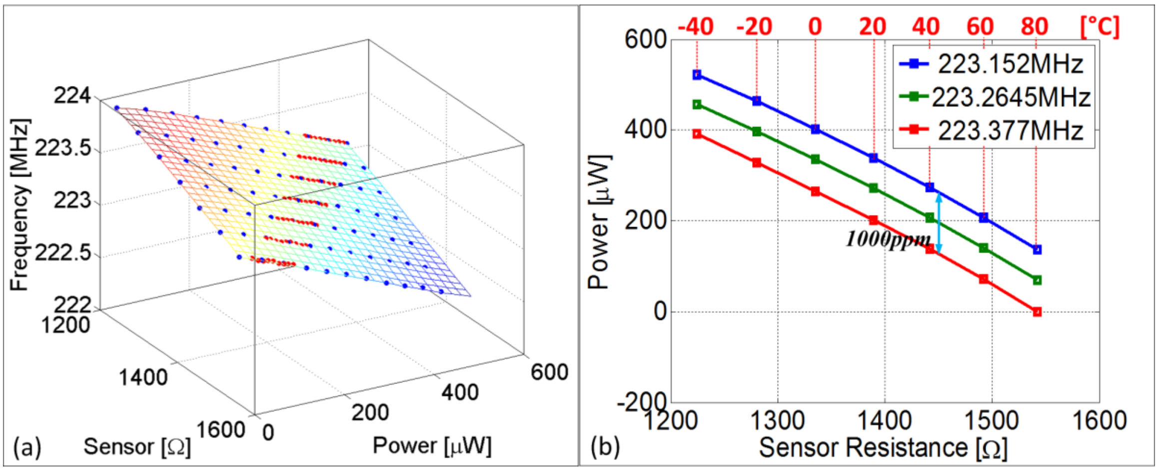

Figure 3.17: (a) The calibration data (blue points) and the relationship (surface plot) obtained from the trained ANN with n=20 between f_s, P and R. The calibration data spread over the entire region of interest. The red points represent another set of independent measurement data, which will be used for validation. In this work, the calibration data are called coarse measurement because they spread over a larger space, while the validation data are called fine measurement as they span a smaller range. (b) The plots of a lookup table obtained from (a) for 3 target frequencies. Blue and red curves represent the lower and upper bounds of the frequency shift achievable by ovenization in this work. Green is the center frequency.

C. Generation of Lookup Tables

Once the training is completed, $\mathbf{W}$ is stored in a micro-controller-unit (MCU). Lookup tables (thermal power versus sensor resistance) are then generated for arbitrary target frequencies based on the obtained relationship (Figure 3.15c and Figure 3.17b). It can be seen that ANN-DTCM can be used to set the initial frequency of operation of the oscillator (at least ±500 ppm as shown in Figure 3.17b), hence compensating for manufacturing variations and eliminating the need for additional trimming. The amount of tuning capability depends on the range of calibration data and the budget of power consumption.

It is also easy to understand why ANN-DTCM is characterized by a faster calibration process. Unlike the conventional DTCM, ANN-DTCM generates lookup tables from calibration data indirectly; therefore, it poses much less constraints on the stabilization of the temperature chamber. Instead, it requires that the ambient temperature when the center frequency is measured is the same as the ambient temperature when the sensor resistance is measured. In fact, these two measurements can be performed within order of milliseconds one after another. As long as the temperature fluctuation does not exceed 0.3 ℃ within such short period of time, ANN-DTCM can achieve a temperature compensation accuracy of 15 ppm/120 ℃. The relaxing requirements on temperature stabilization dramatically reduce the calibration time.

D. ANN-DTCM Testing

The formal testing of ANN-DTCM test should be performed as shown in Figure 3.15d. The MCU is connected to the ohmmeter to monitor the real-time temperature and adjusts the ovenization power accordingly through the power supply. The real-time frequency is monitored via the VNA.

In this work, we used an alternative effective verification method. The target frequencies are chosen and the required thermal power values versus temperatures are calculated. For each temperature, the corresponding frequency upon applying the calculated thermal power is approximated by linear interpolation of fine measurement data (Figure 3.17a) and is compared to the target frequency. As an example, Figure 3.18 shows the interpolation process at –40 ℃. The target frequency is chosen to be 223.2786 MHz. Since the sensor resistance at –40 ℃ is 1224.4 Ω, the calculated thermal power is 448.1 μW. The real frequency is merely –6 ppm off the target frequency.

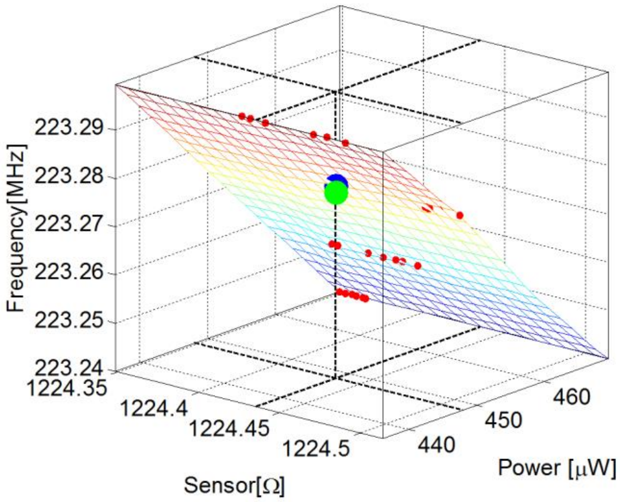

Figure 3.18: Comparison between the target frequency (blue point) and real frequency (green point) at –40 °C. The red points are part of fine measurement at –40 °C and the surface plot is the corresponding linear interpolation. From the sensor sensitivity, the temperature fluctuation is ±0.03 °C.

3.3.2. Results and Discussion

By verifying all frequencies between 223.152MHz and 223.377MHz, we obtained the best and worst frequency fluctuation of 14ppm and 27ppm, respectively, as shown in Figure 3.19. Compared to the previous work that uses resistive feedback, ANN-DTCM shows significant advantages. Beyond the improved temperature stability, no a priori knowledge of the sources of temperature fluctuations is needed. Compared to the state-of-the-art, we attained an oven gain, G, of 200X, and a power consumption of 390 μW over 120 °C (ΔT), which result in an overall figure of merit ($G{\cdot}\Delta T/P$) that is 1 to 2 order of magnitude better than any other compensation methods reported in the literature (Table 3.9). Finally, ANN-DTCM can be used to set the initial frequency of operation of the oscillator, hence compensating for manufacturing variations and eliminating the need for additional trimming.

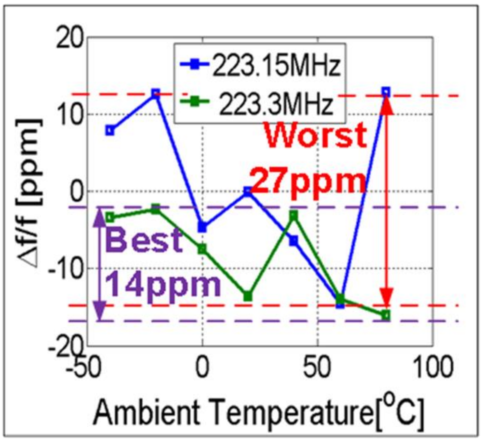

Figure 3.19: The plot of the best and worst frequency change versus temperature after ANN-DTCM for all possible target frequencies between 223.152MHz and 223.377 MHz. Note that no other temperature compensation method was used and the uncompensated resonator exhibits a frequency shift of 2800 ppm.

Table 3.9: Summary and comparison of micro-oven based compensation methods..

	[75]	[76]	[77]	[79]	[72]	**This Work**
Year	2015	2015	2014	2012	2009	2017
Device Type	Capacitive Oscillator	Piezoelectric Oscillator	Fused Silica Oscillator	Piezoelectric Oscillator	Capacitive Oscillator	Piezoelectric Resonator
Compensation Technologies	Composite Material, CRTC	Composite Material, CRTC	CRTC, DTCM	DTCM	Composite Material, PLL, DTCM	ANN-DTCM
Frequency Drift Δf/f	<120ppm/125 ℃	300ppb/125 ℃	11ppm/105 ℃	1.7ppm/110 ℃	0.1ppm/100 ℃	14ppm/120 ℃
Best Oven Gain G	5.1X	~100X	95.5X	1618X	704X	**200X**
Ovenization Power $P/\Delta T$	0.47mW/125 ℃	12.5mW/125 ℃	15.8mW/105 ℃	8.8mW/110 ℃	14.9mW/100 ℃	**0.39mW/120 ℃**
FoM $G{\cdot}\Delta T/P$	1356	1000	635	20225	4275	**61538**
Temperature Range	-40 ~ +85 ℃	-45 ~ +85 ℃	-40 ~ +65 ℃	-25 ~ +85 ℃	-20 ~ +80 ℃	-40 ~ +80 ℃

CHAPTER 4: FORCE MODULATION AND ITS APPLICATION IN PHASE NOISE REDUCTION

AlN CMRs are advantageous over legacy technologies such as quartz crystal or SAW resonators in terms of compact size, low cost, low motional resistance, CMOS-compatibility, and capability of spanning multiple frequencies on the same chip. Despite these promise, AlN CMRs suffer from relatively low quality factor when compared to quartz crystal, SAW, capacitive and thin-film piezoelectric-on-substrate (TPoS) resonators, despite the fact that AlN material has a similar f-Q theoretical limit to quartz and silicon (see Figure 4.1). Even though there have been some studies on how to improve Q of AlN CMR by using, for example, etched slots in the suspension [88], $\lambda/4$ suspensions to confine energy [89], butterfly-shaped plates [90], phononic crystal strip tethers [91], etc., the improvement is limited to about 50% of the original value. There is still a large gap between the experimental Q of AlN CMRs and the theoretical limit of the AlN layer, especially at low frequency from 10 to 500 MHz. Damping in this frequency range is mostly attributed to anchor loss [40, 42, 92] and thermoelastic damping [93]. This challenge prevents AlN CMRs from competing with other MEMS resonators for timing applications.

In this thesis, we look at a completely different approach to improve the effective quality factor of the resonant system. By effective quality factor, we refer to the ratio of center frequency to 3-dB bandwidth of the spectral magnitude response (*e.g.* admittance or the ratio of displacement to force), from the perspective of the driving voltage/force. We plan to reduce the driving voltage/force while maintaining the same level of resonator displacement (or even larger) by means of an externally applied force with a particular phase relationship with respect to (w.r.t) the displacement. By doing so, we are able to sharpen the magnitude response around the resonant frequency, hence increasing the effective Q of the system. We call this method “force modulation” in this thesis.

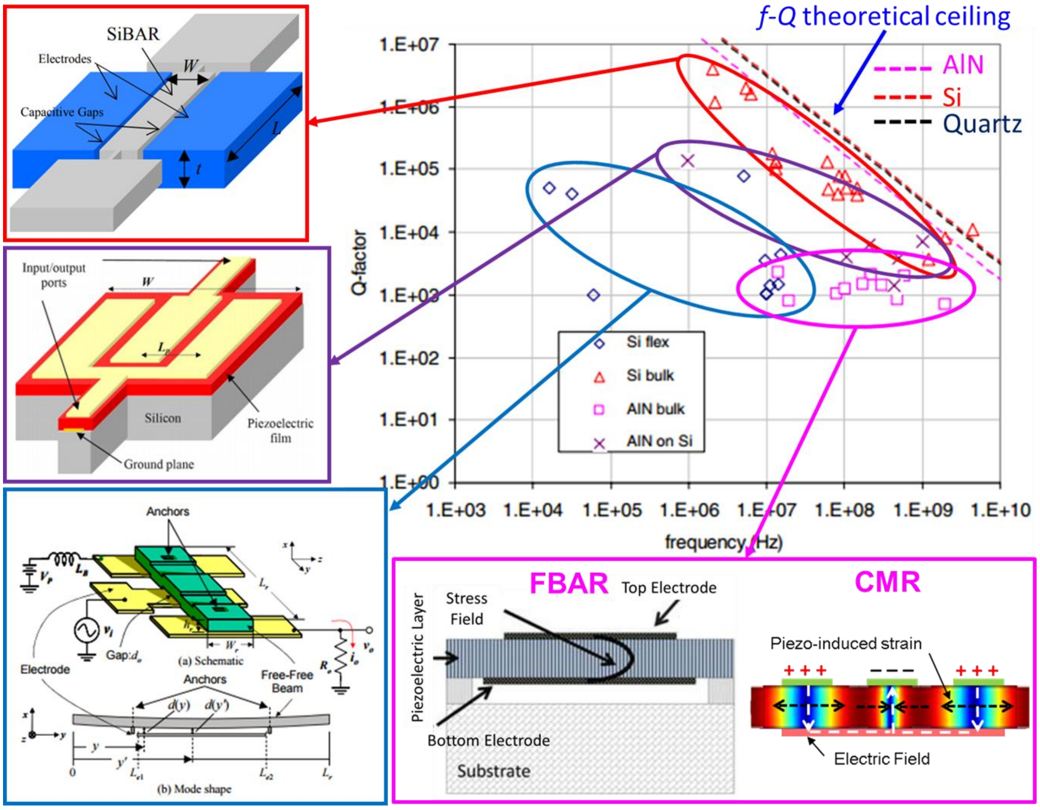

Figure 4.1: Comparison of reported Q_{un} versus frequency for various classes of resonators [19, 94-97].

The fundamental principle of force modulation is similar to a concept of “force feedback” frequently seen in the accelerometer and gyroscope applications [98, 99]. The force feedback is primarily used to improve the sensitivity, reduce the power consumption, increase the dynamic range of operation, and enhance the linearity [100]. However, its potential applications in the enhancement of Q are rarely seen except in [101] and [102], and so does its applications in the phase noise reduction. Furthermore, as will be evident later, the specific implementation of force modulation in this work is different from and also much simpler than the conventional force feedback. In this chapter, we will first intuitively explain the concept using a spring-damper-mass system, followed by a more rigorous method that uses a two-port resonator to implement this concept. In the end, we will demonstrate the force modulation experimentally and apply it to phase noise reduction in an oscillator circuit.

4.1. Force Modulation in Spring-Damper-Mass System

Let us consider a canonical second-order system, as shown in Figure 4.2, to which an external force, F_{ext}, is applied to the mass in conjunction with the driving force, F_{drive}. If F_{ext} is out-of-phase with respect to the damping force, $D\dot{x}$, the effective damping force could be made smaller from the perspective of F_{drive}. In this way, F_{drive} can be smaller than the original force to maintain the same displacement (or even larger), which means that the effective quality factor seen by F_{drive} is larger. Under particular conditions, the damping force is perfectly cancelled out by F_{ext}, hence, the displacement keeps the same even when F_{drive} is 0 and the system equivalent quality factor is infinite. In this sense, F_{ext} is called a modulation force, as it can modulate the resonator quality factor. From the perspective of this modulated second order system, it is fundamentally the same as the concept of “force feedback” in [98].

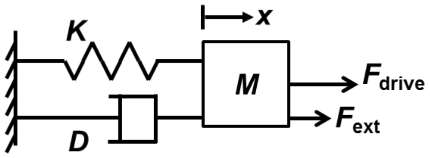

$$M\ddot{x} + D\dot{x} + Kx = F_{drive} + F_{ext}$$

If $F_{ext} = \mu\dot{x}$

$$M\ddot{x} + (D - \mu)\dot{x} + Kx = F_{drive}$$

Figure 4.2: Schematic representation of a canonic second-order system with sinusoidal excitation force F_{drive} and modulation force F_{ext}.

Recall that the displacement response without force modulation in complex form, $X^{(0)}$, of the spring-damper-mass to a single sinusoidal excitation force, $F_{drive}^{(0)}$, is

$$\frac{X^{(0)}}{F_{drive}^{(0)}} = \frac{1}{K}\frac{1}{1-r^2 + j2r\zeta}, \tag{4.1}$$

where $r = \dfrac{\Omega}{\omega_n}$ is the normalized frequency, Ω is the frequency of the driving force, $\omega_n = \sqrt{\dfrac{K}{M}}$ is the natural frequency, and $\zeta = \dfrac{D}{2\sqrt{KM}}$ is the damping factor. The system's quality factor is Q = $1/(2\zeta)$ without the modulation force. With the external force, the system displacement, $X^{(1)}$, becomes

$$\frac{X^{(1)}}{F_{drive}} = \frac{1}{K}\frac{1}{1-r^2 + j2r\zeta^*}, \tag{4.2}$$

where $\zeta^* = \dfrac{D-\mu}{2\sqrt{KM}} = \zeta^* - \dfrac{\mu}{2\sqrt{KM}}$ is the new effective damping factor after modulation. The new quality factor is $Q^* = 1/(2\zeta^*)$ which can be engineered to be larger than the intrinsic Q of the system, as exemplified in Figure 4.3a and b. If the resultant displacement with modulation stays the same as that without modulation, *i.e.* $X^{(1)} = X^{(0)}$, the ratio of $F_{drive}\big/F_{drive}^{(0)}$ is:

$$\frac{F_{drive}}{F_{drive}^{(0)}} = \frac{1-r^2 + j2r\zeta^*}{1-r^2 + j2r\zeta}, \tag{4.3}$$

Near the resonant frequency, the ratio becomes

$$\frac{F_{drive}}{F_{drive}^{(0)}} \approx \frac{\zeta^*}{\zeta} < 1 \tag{4.4}$$

which complies with the intuitive expectation. We can also calculate the ratio of $F_{ext}\big/F_{drive}^{(0)}$ to be:

$$\frac{F_{ext}}{F_{drive}^{(0)}} = \frac{j\Omega\mu X^{(1)}}{X}\frac{1}{K}\frac{1}{1-r^2 + j2r\zeta} = j2r \cdot \frac{\mu}{2\sqrt{KM}} \cdot \frac{1}{1-r^2 + j2r\zeta} \tag{4.5}$$

Around the resonant frequency, it reduces to

$$\frac{F_{ext}}{F_{drive}^{(0)}} \approx \frac{1}{\zeta}\frac{\mu}{2\sqrt{KM}} = \frac{\zeta-\zeta^*}{\zeta} \le 1 \tag{4.6}$$

which is the relative change of the damping factor. An example of F_{drive} and F_{ext} is visualized in Figure 4.3c and d. Eq. (4.5) indicates that the system quality factor with modulation increases when the F_{ext} increases until it hits the original force, $F_{drive}^{(0)}$, in which F_{drive} is 0 and the quality factor is infinite. If F_{ext} continues increasing, the quality factor decreases instead. Combining with Eq. (4.4) and (4.6), we have

$$\frac{F_{drive}+F_{ext}}{F_{drive}^{(0)}} = \frac{\zeta^*}{\zeta} + \frac{\zeta-\zeta^*}{\zeta} = 1 \tag{4.7}$$

$$\frac{F_{ext}}{F_{drive}} = \frac{\zeta-\zeta^*}{\zeta^*} \tag{4.8}$$

Eq. (4.7) means that the work difference between $F_{drive}^{(0)}$ and F_{drive} is compensated by F_{ext}. In other words, the energy pumped to the spring-damper-mass system by the F_{drive} and F_{ext} together balances with the energy dissipation by the damping force, which equals to the work done by $F_{drive}^{(0)}$. Although the force modulation method doesn't reduce the total energy loss, it alters the spectral response of $X^{(1)}/F_{drive}$ and thus the quality factor seen by F_{drive}. From Eq. (4.8), it can be inferred that the external force, F_{ext}, should be in-phase with the driving force, F_{drive}, at the resonant frequency.

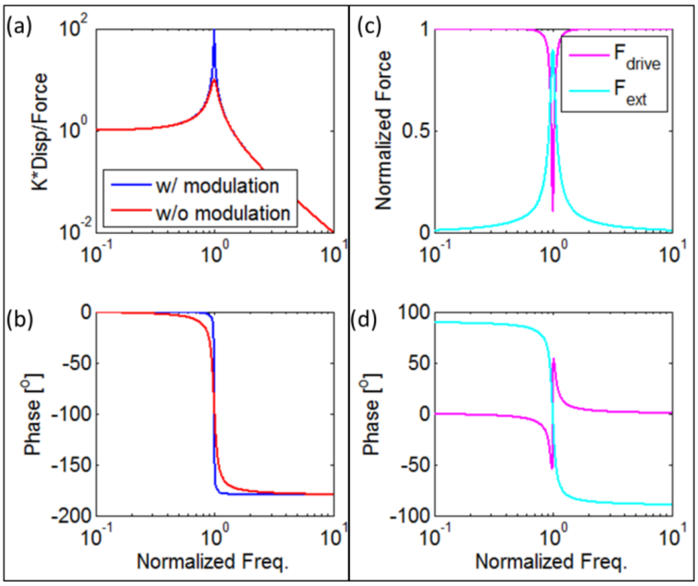

Figure 4.3: (a) Magnitude and (b) phase response of a second order system with and without modulation. Q is 10 without modulation and 100 with modulation. (c) Magnitude (normalized to $F^{(0)}_{drive}$) and (d) phase response of F_{drive} and F_{ext} for constant-phase-delay mode.

As the reader may notice, it is presumed that F_{ext} has a constant +90° or −270° phase shift w.r.t the displacement for all frequencies. We call this phase relationship "constant-phase-delay mode" in this thesis. However, only near the resonant frequencies does such phase relationship play a role in the Q amplification. In other words, there are other phase relationships that could be used to boost the quality factor as long as F_{ext} is in-phase with F_{drive} at the resonant frequency. For example,

$$F_{ext} = \Omega\mu X^{(2)} \exp\left(-jr\cdot\frac{3\pi}{2}\right) = \Omega\mu X^{(2)} \exp\left(-j\Omega\cdot\frac{3\pi}{2\omega_n}\right) = \Omega\mu X^{(2)} \exp\left(-j\Omega\tau_0\right) \quad (4.9)$$

where $\tau_0 = 3\pi/2\omega_n$ is a constant time delay, $X^{(2)}$ is the displacement under the new external force. In contrast, we call this phase relationship "constant-time-delay mode". Compared to constant-phase-delay mode, constant-time-delay mode offers more flexibility in terms of implementation in RF domain, which can be readily achieved by a commercial programmable RF phase shifter. It is the method that will be applied to boost Qs of AlN CMRs in the later sections. The new displacement response, $X^{(2)}$, becomes

$$\frac{X^{(2)}}{F_{drive}} = \frac{1}{K}\frac{1}{1-r^2+j2r\zeta-2r\left(\zeta-\zeta^*\right)\exp\left(-jr\cdot\frac{3\pi}{2}\right)}, \tag{4.10}$$

It is easy to verify that Eq. (4.4), (4.6)-(4.8) are still valid near the resonant frequency. The example spectral response for the same amount of Q amplification as Figure 4.3a and b is shown in Figure 4.4a and b. However, one can observe that the spectral responses of F_{drive} and F_{ext} are dramatically different (see Figure 4.4c and d) from Figure 4.3c and d.

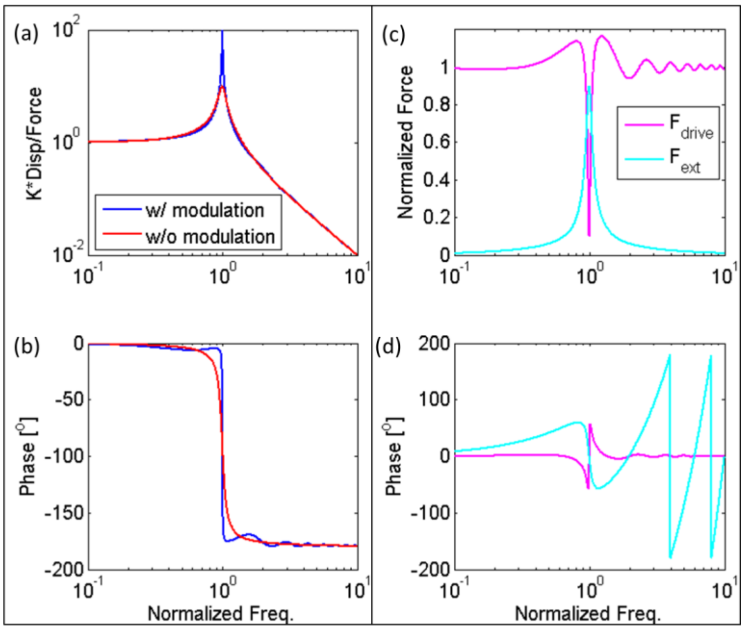

Figure 4.4: (a) Magnitude and (b) phase response of a second order system with and without modulation. Q is 10 without modulation and 100 with modulation. (c) Magnitude (normalized to $F^{(0)}_{\text{drive}}$) and (d) phase response of F_{drive} and F_{ext} for constant-time-delay mode.

It is also important to notice that, if the phase shift of F_{ext} w.r.t the displacement at the resonant frequency deviates from +90 °(−270 °), the system exhibits a different natural frequency (which is defined as the frequency where the peak response occurs). Assuming $F_{ext} = \mu\dot{x} \mp \lambda x$, then the governing equations becomes

$$M\ddot{x} + (D - \mu)\dot{x} + (K \pm \lambda)x = F_{drive} \tag{4.11}$$

This system has the same amount of Q amplification. However, the exhibited natural frequency is $\omega_n^* = \sqrt{\frac{K \pm \lambda}{M}}$.

Equally important, if the deviation of phase shift from $+90^\circ$ (-270°) occurs at other frequencies, although the peak location doesn't change, the system's effective stiffness is altered in the same way. It is obvious to conclude that, if the phase shift is smaller than $+90^\circ$ (-270°), the system's effective stiffness becomes smaller, and vice versa. Therefore, for F_{ext} expressed as Eq. (4.9), the system's effective stiffness is larger than K when $\Omega < \omega_n$, and smaller than K when $\Omega > \omega_n$.

4.2. Force Modulation in Two-Port Resonator

A possible embodiment of the simple concept of force modulation explained above is to use a resonator with two separate ports, Port 1 used to induce the resonance and Port 2 to modulate it (Figure 4.5). The alternate voltage applied to Port 2 expands and contracts the AlN body, and effectively exerts an external force on Port 1. The convenience of using this configuration is that it is possible to achieve force modulation by using a simple relationship between V_1 and V_2 (constant-time-delay mode):

$$\frac{V_2}{V_1} = C_1 e^{-j\Omega\tau_0} = C_1 e^{-j\frac{\Omega}{\omega_s}\theta_0} \tag{4.12}$$

where C_1 is a constant real number, τ_0 is a constant time delay, and θ_0 is the phase shift (delay) at the resonant frequency, ω_s. Such simple relationship can be easily implemented by a variable gain amplifier and a programmable phase delay line.

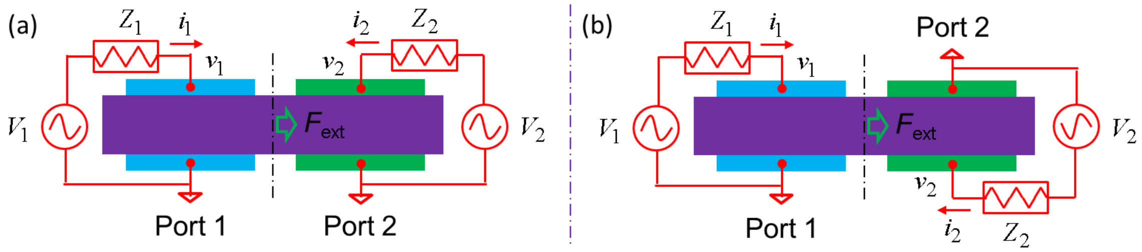

Figure 4.5: Two configurations for exerting force on Port 1 by Port 2 in a two-port-resonator that would require different amounts of time delay. Special attention should be paid to which configuration is used in the experiments to avoid confusions.

Let us start with the qualitative analysis of the phase of V_2/V_1. The relationship between V_1 and the displacement of Port 1, X_1, can be approximated by that between the driving force and the respondent displacement in the second-order system, respectively. So does that between V_2 and the displacement of Port 2, X_2. F_{ext} exerted on the right end of Port 1 (the center of the two-port resonator) is in-phase with X_2, while F_{ext} exerted on the left end of Port 1 is out-of- phase with X_2, because F_{ext} propagates half of the wave length from the right end to the left one. As a rough approximation, X_2 has an average +90° phase shift w.r.t F_{ext}. To achieve Q amplification at the resonant frequency, F_{ext} should have +90°(–270°) phase shift w.r.t X_1. Since V_1 and V_2 have the same phase shift (+90°) w.r.t X_1 and X_2, respectively, V_2 should be out-of-phase with V_1. The above analysis is visualized in Figure 4.6.

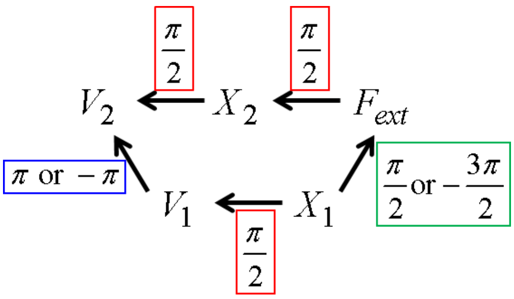

Figure 4.6: Visualization of phase relationships between variables of interest at the resonant frequency for the configuration in Figure 4.5a. The arrows mean the direction of phase increment.

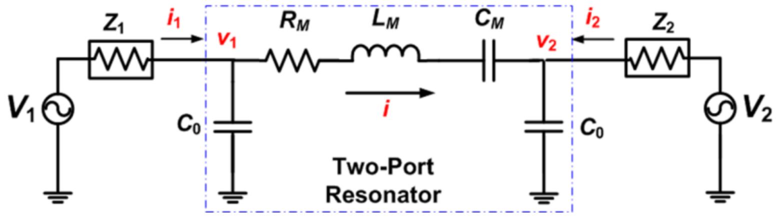

Figure 4.7: Equivalent circuit for Figure 4.5a. Z_1 and Z_2 are termination impedance, typically 50 Ω.

To derive the quantitative relationship between V_1 and V_2, the equivalent circuit model for a two-port resonator is employed. Figure 4.7 shows a circuit representation of the two-port resonator of Figure 4.5a whose transformer ratio is 1 (the transformer ratio is –1 for Figure 4.5b). The effect of the modulation signal V_2 is to null v_1 at the resonant frequency, which boosts the admittance at the resonant frequency (thus Q) to infinity. Note that the voltage v_1 in the electrical domain corresponds to the force F_{drive} in the mechanical domain. Effectively, the driving force F_{drive} is decreased to boost the Q “as seen” at port 1. For this condition to happen, a specific magnitude and phase relationship between V_2 and V_1 at the resonant frequency needs to exist (assuming $Z_1 = Z_2 = Z_0 = 50\ \Omega$):

$$\frac{V_2}{V_1} = C_1 e^{-\theta_0} = -\left[\frac{Z_0}{Z_1}\frac{R_M}{Z_0} + \frac{Z_2}{Z_1} + j \cdot \frac{Z_2}{Z_1} \cdot \omega_s R_M C_0\right] = -\left(\frac{R_M}{Z_0} + 1 + j\frac{4}{\pi^2}\frac{1}{k_t^2 Q}\right) \tag{4.13}$$

where k_t^2 is defined for a two-port device by Eq. (2.21). This ratio is called the “critical ratio” in this work. The critical phase shift (delay) $\theta_0 \in (90°, 180°)$. Typically, $k_t^2 Q >> 1$, hence $\theta_0 \sim 180°$. This is the same as the conclusion of the qualitative analysis. One can verify that, for the configuration in Figure 4.5b, the critical ratio at the resonant frequency is

$$\frac{V_2}{V_1} = C_1 e^{-\theta_0} = \left[\frac{Z_0}{Z_1}\frac{R_M}{Z_0} + \frac{Z_2}{Z_1} + j \cdot \frac{Z_2}{Z_1} \cdot \omega_s R_M C_0\right] = \left(\frac{R_M}{Z_0} + 1 + j\frac{4}{\pi^2}\frac{1}{k_t^2 Q}\right) \tag{4.14}$$

In contrast, $\theta_0 \in (-90°, 0°)$ for the configuration in Figure 4.5b. Considering $k_t^2 Q >> 1$, $\theta_0 \sim 0°$.

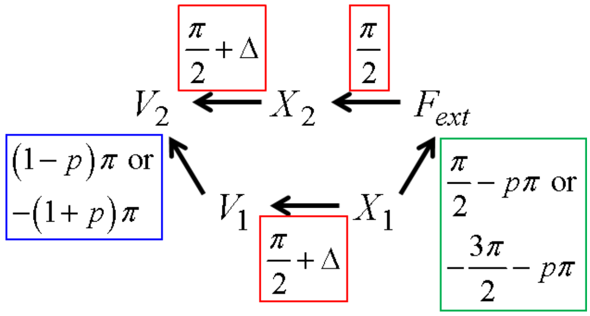

Figure 4.8: Visualization of the phase relationships between variables of interest near the resonant frequency, (1 + *p*)ω_s. *p* is the percentage of frequency shift w.r.t ω_s, and Δ is the corresponding phase change of the second-order system. The arrows mean the direction of phase increment.

As concluded in Section 4.1, for the constant-time-delay-mode force modulation, the systems' effective stiffness varies over the frequency spectrum. Considering the force modulation of a two-port resonator, near the resonant frequency, as shown in Figure 4.8, F_{ext} has <90 °phase shift w.r.t X_1 (if $p > 0$), and the effective stiffness becomes smaller. According to the analogy between C_m and $1/K$, one could expect that Port 1 sees C_m being larger for $\Omega > \omega_s$. Hence, Port 1 with force modulation would see higher k_t^2. Note that k_t^2 here is defined for one-port resonator by Eq. (2.20). Due to the same reasoning, the resonant frequency can be tuned by the force modulation if the phase delay deviates from the critical phase shift at the resonant frequency. Particularly, if θ_0 is larger than the critical phase delay, F_{ext} has <90 ° phase shift w.r.t X_1, the effective stiffness become smaller, and so does the resonant frequency.

At the out-of-band frequency, the motional branch of R_M–L_M–C_M can be neglected. Therefore, the equivalent circuit for Figure 4.5a is reduced to Figure 4.9. For the devices of interest, the feedthrough capacitance C_F is much smaller than C_0. Therefore, the admittance seen by Port 1 would be approximately the admittance of C_0.

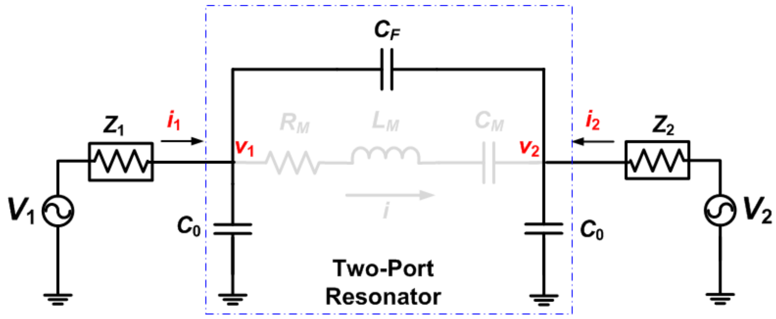

Figure 4.9: Equivalent circuit including the feedthrough capacitance C_F for Figure 4.5a far off the resonant frequency. The light black path is blocked.

Simulation in MATLAB of the same circuit further confirms the above analysis (see Figure 4.10). The electrical parameters used in the simulation are estimated from the measured admittance response of a 2-port device wirebonded on PCB and are listed in Table 4.1. For this case, the critical ratio is $-(4.76 + j0.24)$, *i.e*. the critical gain and phase delay are 4.77 and 177°, respectively. As the constant gain C_1 approaches the critical gain (with the same phase delay $\theta_0 = 177°$), Q increases dramatically as the phase slope at the resonant frequency becomes steeper (see Figure 4.10). However, if C_1 exceeds the critical gain, Q decreases instead. Such property prevents the system from self-oscillation although amplifiers are involved, as will be clearer in the Section 4.3. Furthermore, k_t^2 becomes larger because of constant time delay between V_2 and V_1. Additionally, as expected, the deviation from the critical phase delay alters the resonant frequency of the system (see Figure 4.11). Within the simulation range, the frequency shift is linearly dependent of the deviation from the critical phase shift, whose linear coefficient is 6.8 ppm/deg. Such dynamic frequency tuning capability has been demonstrated to stabilized oscillator frequency [101]. As predicted, the force modulation doesn't change the out-of-band admittance. The detailed simulated resonator performance (f_s, Q, k_t^2) under different force modulation conditions are listed in Table 4.2.

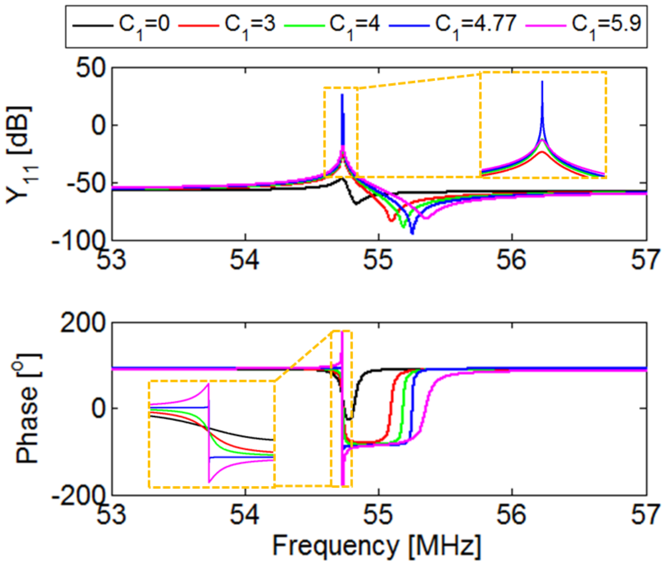

Figure 4.10: Admittance response (magnitude and phase vs. frequency) seen at port 1 as a function of different modulation forces. Except the black curves (no modulation), all other responses have the same critical phase delay of 177°.

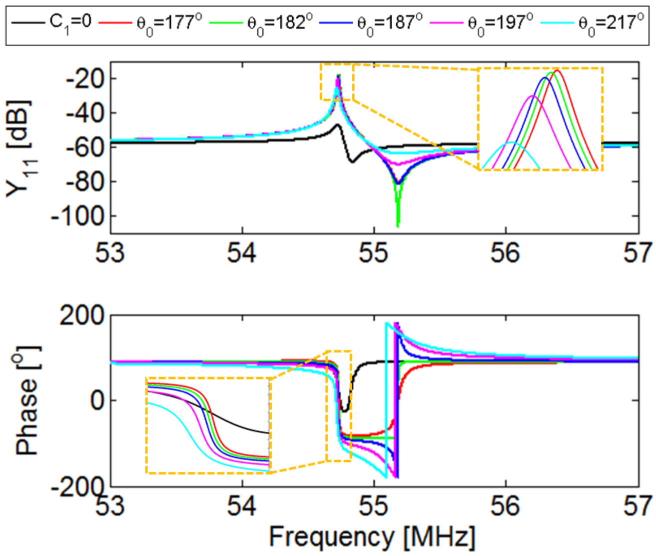

Figure 4.11: Admittance response (magnitude and phase vs. frequency) seen at port 1 as a function of different modulation forces. Except the black curves, all other responses have the same gain of 4.

Table 4.1: The parameters employed in the MATLAB simulation for the configuration in Figure 4.5a. The relative large C_0 includes both intrinsic resonator capacitance and PCB parasitics and hence relative low k_t^2. k_t^2 is defined for two-port resonator.

Parameters	ω_s	C_0	k_t^2	Q	C_M	L_M	R_M
Value	$2\pi \times 54.7$ MHz	3.69 pF	0.82%	1165	12.2 fF	693 μH	188 Ω

Table 4.2: Comparison of resonator performance (f_s, Q, k_t^2) between no force modulation (experiment) and different force modulation (simulation). k_t^2 is defined for one-port resonator. The phase delay is evaluated at 54.67 MHz in this table. Data in bold red and black correspond to Figure 4.10 and Figure 4.11, respectively.

Voltage Gain C_1 [V/V]	Phase Delay θ_0 [°]	f_s [MHz]	Q	k_t^2 [%]
w/o modulation	--	**54.6750**	**1,165**	**0.41**
3	**177**	**54.7361**	**2,710**	**1.63**
4	**177**	**54.7361**	**6,258**	**2.04**
4	182	54.7341	6,084	2.04
4	187	54.7321	5,718	2.05
4	197	54.7282	4,653	2.07
4	217	54.7212	2,759	2.21
4.77	**177**	**54.7361**	**1,089,135**	**2.36**
5.9	**177**	**54.7361**	**4,212**	**2.82**

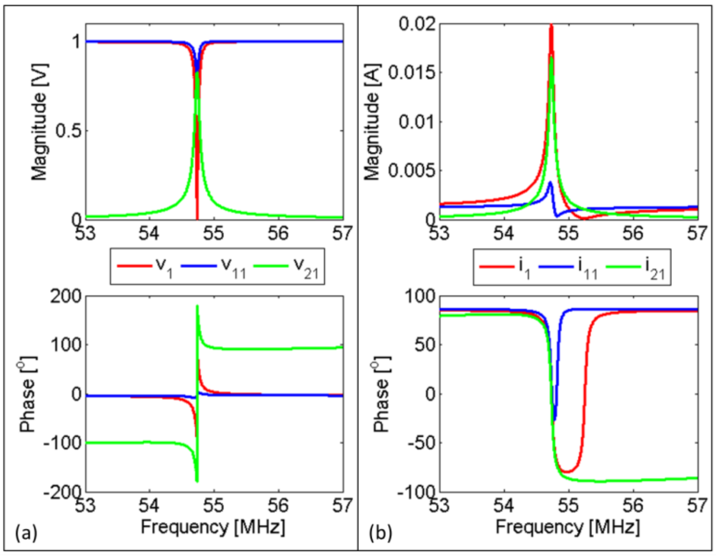

Figure 4.12: Decomposition of (a) v_1 response, and (b i_1 response, under the force modulation with critical ratio.

It is worth re-stating that, as explained with the canonical second-order system, the force modulation doesn't reduce the total damping, but rather reduce the driving voltage, v_1, while boosting the driving current, i_1, near the resonant frequency, as shown in Figure 4.12. From the linear superposition theory, the driving voltage and driving current can be decomposed into the contribution of V_1 and V_2 independently:

$$v_1 = v_{11} + v_{21} \tag{4.15}$$

$$i_1 = i_{11} + i_{21} \tag{4.16}$$

where v_{11} and i_{11} are the resultant voltage and current responding to V_1, while v_{21} and i_{21} are to V_2, which are plotted in Figure 4.12. As can be observed, at the resonant frequency, v_{21} cancels v_{11}, while i_{11} and i_{21} add up constructively. Out of band, the contribution of V_2 is minimal, thus leaving the admittance nearly intact.

As a point of comparison, let us look at a typical force feedback system as shown in Figure 4.13. In the force feedback, the feedback signal comes from the mass displacement, which is converted to force and is exerted on the mass. Typically, the control circuitry in Figure 4.13 is very complex, on which most research efforts are made [99, 100, 103, 104]. On the contrary, the feedback signal is taken from the driving source directly in our force modulation system. Therefore, our force modulation system is much simpler than the conventional force feedback system.

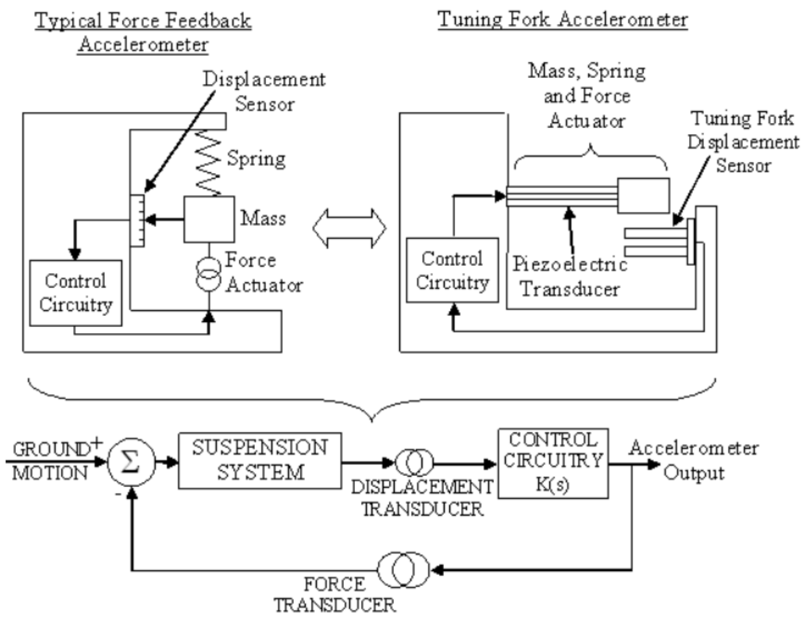

Figure 4.13: Schematic representation of the force feedback tuning fork accelerometer and its corresponding systematic block diagram. The ground motion is equivalent to the driving force, acting on the mass and causing the relative motion. The tuning fork measures the relative motion and adjusts the voltage to the piezoelectric transducer, which moves the transducer back to its initial position, effectively eliminating the relative motion. The control voltage to the piezoelectric transducer is proportional to the relative motion and becomes the output of the accelerometer. Reprinted from [98].

4.3. Experimental Verification

We verified this concept first by demonstrating the improvement in Q by monitoring the admittance response of a 2-port resonator, and then by showing reduction of phase noise in an oscillator built around the same 2-port resonator.

4.3.1. Improvement of Q in Admittance

Figure 4.14a shows the calibration setup for force modulation. The signal from the VNA port is split into two (Macom T-1000), and directed either towards the feedback branch (upper branch in Figure 4.14a) and the test branch (lower branch in Figure 4.14a), respectively. In the feedback branch, two cascaded 10 dB fixed attenuators (MiniCircuits VAT-10) are placed in front of three cascaded LNAs (one MiniCircuits ZFL-500LN+ plus two Holzworth HX2400, for a total forward gain of ~56 dB) to isolate LNAs from the power splitter (PS) as well as provide a good match to PS (well below −40 dB). At the same time, the reverse isolation provided by the cascaded LNAs is around –77 dB. Therefore, any signal pass through the feedback branch from right to left will be significantly damped by at least 97 dB. Moreover, the refection coefficient (S_{11}) of the test branch seen by the power splitter is not affected by the phase shifter (Colby PDL-100A-10NS), variable attenuator (by cascading different MiniCircuit attenuators, such as VAT-10, VAT-6, and VAT-3), directional coupler (MiniCircuits ZX30-12-4-S+), and different loading conditions following the coupler in the feedback branch. It is such property that validates the SOL calibration and following one-port measurement. After performing typical SOL calibration at the calibration plane shown in Fig. 4.6a, it is double-verified that the admittance measurements taken at the calibration plane (without the force feedback on but disconnected from the device under test) are the same as taken directly at the VNA port. To estimate the gain and phase shift of the feedback branch, directional couplers are introduced to both branches. The coupled signals (denoted as Osc1 and Osc2) are monitored by an oscilloscope around center frequency. The gain is estimated as the magnitude ratio of Osc2 to Osc1 and the phase shift as the phase difference between Osc2 and Osc1.

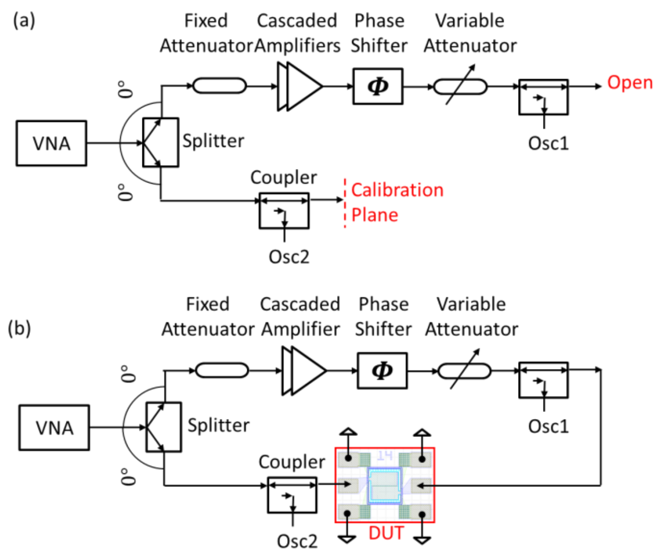

Figure 4.14: (a) calibration setup and (b) experimental verification setup for the force modulation. Arrows denotes signal propagation direction. Two cables connecting couplers to resonator ports are identical (the figure doesn't show the real scale of cables).

To directly prove the improvement of Q in admittance, S_{11} measurements are performed in the way shown in Figure 4.14b. Figure 4.15 shows the effect of increasing gain while keeping the phase delay approximately constant. The corresponding resonator performance (f_s, Q, k_t^2) for different force modulation gains are listed in Table 4.3 (bold red data). Most importantly, it is possible to obtain Q over 160,000 (C_1~5.9V/V, θ_0~180°) which is more than 140 times larger than the original 3dB-bandwidth Q of the resonator. Secondly, the exhibited patterns of changes in resonator Q and k_t^2 are similar to the simulations in Figure 4.10. However, the experiment exhibits improvements in the device Q for different values of the critical ratio. The reason for this discrepancy is currently unknown. Deviations from the critical phase delay alter the resonant frequency, which could explain the frequency shift seen experimentally. Figure 4.16 displays the resultant admittance response when increasing the phase shift (maintaining the gain). The corresponding resonator performance (f_s, Q, k_t^2) for different force modulation phase shifts are also listed in Table 4.3 (black data). The exhibited patterns of changes in resonator f_s, Q and k_t^2 are also similar to the simulations in Figure 4.11. The linear coefficient of the dependence of resonant frequency on the phase shift is estimated to be −8.9 ppm/deg, comparable to the theoretical value.

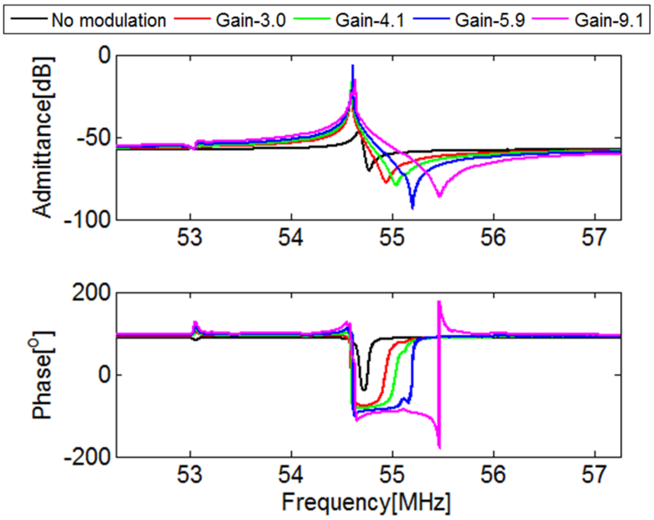

Figure 4.15: Comparison of admittance response between force modulation with different gains and no force modulation. The phase shift of all force modulation is estimated to be 180°.

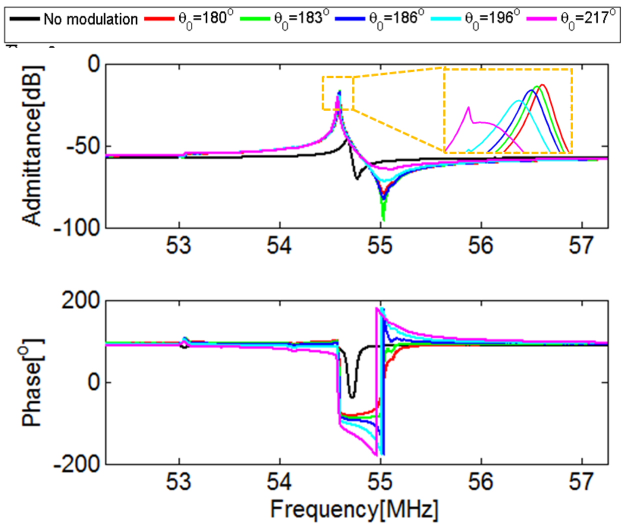

Figure 4.16: Comparison of admittance response between force modulation with different phase shifts and no force modulation. The gain of all force modulation is estimated to be 4.1.

Table 4.3: Comparison of resonator performance (f_s, Q, k_t^2) between no force modulation and different force modulation. The first column represents the implementation of variable attenuators. For example, 10-10-6 means the series connection of VAT-10, VAT-10, and VAT-6. Each attenuator introduces an additional time delay of ~250 psec. The second column records the specified time delay of the programmable phase shifter. The voltage gain and phase delay are averaged over different measurements and are evaluated at 54.7594MHz in this table. Data in bold red and black correspond to Figure 4.15 and Figure 4.16, respectively.

Cascaded Attenuator [dB]	Programmed Delay [psec]	Voltage Gain C_1 [V/V]	Phase Delay θ_0 [°]	f_s [MHz]	Q	k_t^2 [%]
w/o modulation	--	--	--	**54.6750**	**1,165**	**0.41**
10-10-6	**0**	**3.0**	**180**	**54.5938**	**3,984**	**1.58**
10-10-3	**0**	**4.1**	**180**	**54.5984**	**8,782**	**1.96**
10-10-3	250	4.1	183	54.5969	8,142	1.99
10-10-3	500	4.1	186	54.5953	7,118	2.01
10-10-3	1000	4.1	196	54.5906	5,210	2.01
10-10-3	2000	4.1	217	54.5734	4,800	2.41
10-10	**250**	**5.9**	**180**	**54.6071**	**165,071**	**2.71**
10-6	**250**	**9.1**	**180**	**54.6359**	**7,648**	**3.76**

As mentioned before, the force modulation is able to boost Q without issues associated with self-oscillation. Considering the setup in Figure 4.14b without VNA, the oscillation condition in Eq. (2.27a) is impossible to be satisfied because of the isolation (~40 dB) between the two outputs of the power splitter. This is advantageous over other active Q-boosting methods [105].

4.3.2. Oscillator Phase Noise Reduction

A possible application of the force modulation is to reduce the phase noise (PN) of resonator-based oscillators as shown in Figure 4.17 and Figure 4.18. We use one port of the two-port resonator (similar to the resonator tested in Figure 4.14) as a frequency-selective component in the oscillator loop. The cut-off frequency of the low pass filter (LPF) is 100 MHz, which prevents the oscillator from operating at higher frequency. One quarter of the oscillator output is phase shifted, attenuated, amplified, filtered, and finally fed to the second port of the resonator. The reason for putting variable attenuators (by cascading different fixed MiniCircuits attenuators) prior to the amplifier is to reduce nonlinear distortion in the amplifiers. The LPF in the feedback path is used to filter out any harmonic tones. Similarly, the oscillation signal (Osc1) and the feedback signal (Osc2) can be monitored by introducing directional couplers (MiniCircuits ZX30-12-4-S+). The phase noise of the oscillator signal is measured by an Agilent E5052B signal source analyzer (SSA).

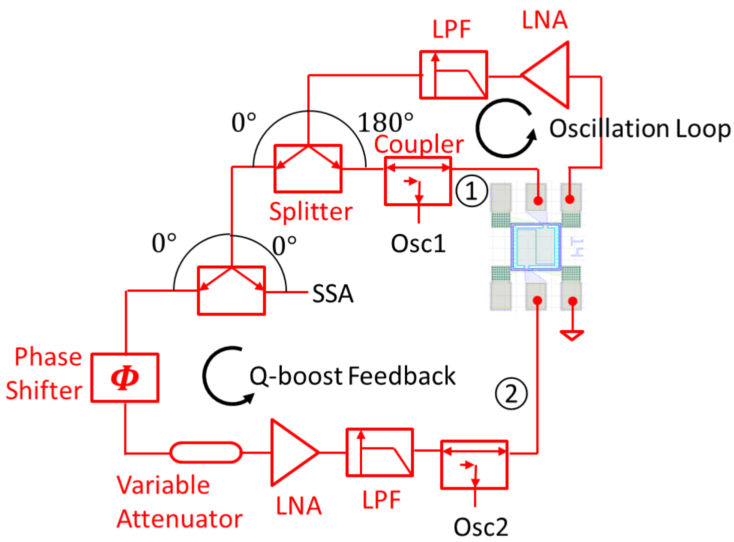

Figure 4.17: Experimental setup of oscillator circuit with feedback path for force modulation. LPFs are MiniCircuits SLP-100. The LNA in oscillation loop is MiniCircuits ZFL-500LN+, while the LNA in the feedback loop is two cascaded Holzworth HX2400 (Typical total gain of 28 dB). The phase-unbalanced splitter is MiniCircuits ZFSCJ-2-232-S+. The rest components are the same as that in Figure 4.14.

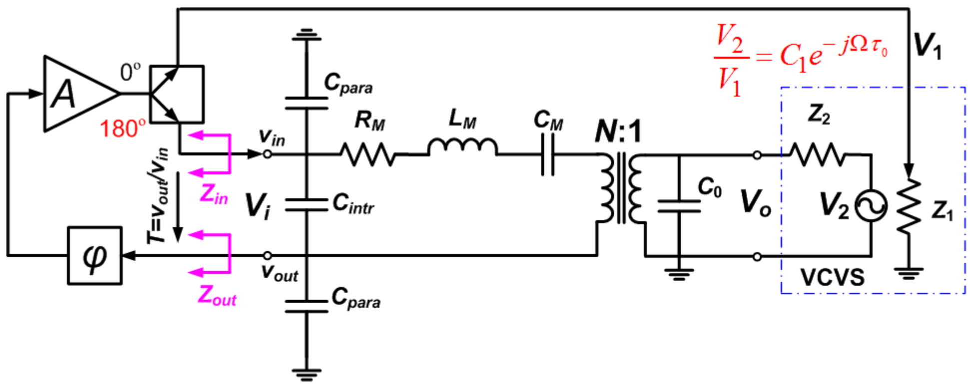

Figure 4.18: Equivalent circuit of oscillator circuit in Figure 4.17. C_{intr} is the intrinsic capacitance of the first port, and C_{para} is the PCB parasitic capacitance (primarily due to SMA connectors). Therefore, $C_0 = C_{intr} + C_{para}$. The transform ratio $N = 1$. The feedback path is modeled as a VCVS. φ represents the overall phase delay of SMA cables in the oscillator loop. The transfer function, T, is the ratio of output voltage, v_{out}, to the input voltage, v_{in}, of Port 1. Z_{in} and Z_{out} are the equivalent impedance seen from the right side at node v_{in} and v_{out}, respectively.

As shown in Figure 4.19, without feedback, the oscillator oscillates at 54.444 MHz with a phase noise of –105.9 dBc/Hz at 10 kHz offset. In contrast, with the appropriate feedback signal applied to port 2 (the variable attenuator is the series connection of VAT-10, VAT-10, and, VAT-3, while the specified time delay of the phase shifter is 500 psec), the oscillator frequency shifts to 54.569 MHz and the phase noise reduces to –135.0 dBc/Hz at 10 kHz offset. The waveforms of the oscillator output (Osc1) and of the feedback signal (Osc2) are presented in Figure 4.21. From these curves it is possible to roughly estimate the values of the overall gain and phase shift for Osc2 signal w.r.t Osc1 signal, which are respectively 1.25 V/V and 112°. The overall gain is consistent with difference between the amplifier gain (~28 dB) and the attenuation (~23 dB from attenuators plus ~3 dB due to power splitter) in the feedback path, which is ~2 dB (1.26 V/V).

The 30 dB improvement could be attributed to two possible mechanisms: improvement of *Q* due to the force modulation and steeper phase slope (original) at new oscillation frequency. To quantify the contribution of the latter mechanism, additional phase shift is introduced in the oscillator loop (see Figure 2.8) to set the frequency of operation as close as possible to the one at which the system operates when the feedback signal is present. The new frequency of oscillation is set to 54.564 MHz. The phase noise at 10 kHz offset improves to –119.2 dBc/Hz at the new frequency of oscillation. The improvement, though, is still less than what attained when the feedback signal is present. This means that there is an overall improvement of phase noise of around 10 dBc through the feedback mechanism. The improvement in phase noise is further confirmed by comparing the Allan deviation of the two circuits (Figure 4.20). However, it seems to be hard to improve the phase noise further in the experiment. We hypothesized that this is because the frequency selectivity depends on the *Q* of transfer function *T* rather than the effective resonator quality factor, but the loading effect of Z_{in} and Z_{out} on T limits the maximum Q can be boosted.

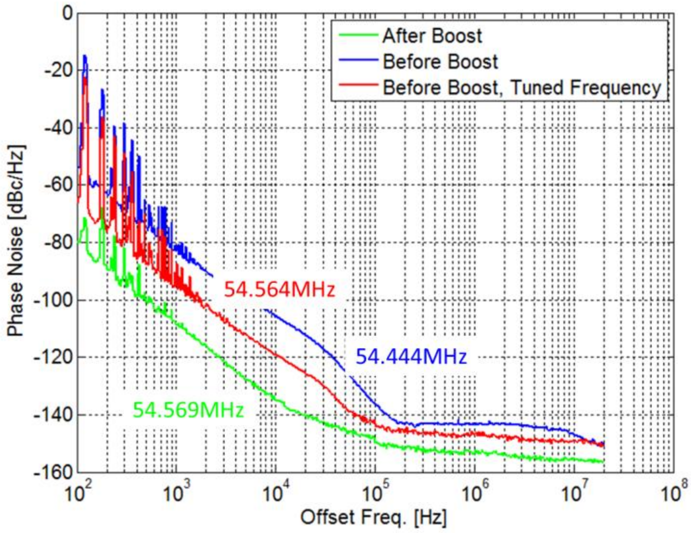

Figure 4.19: Comparison of phase noise between after and before force modulation.

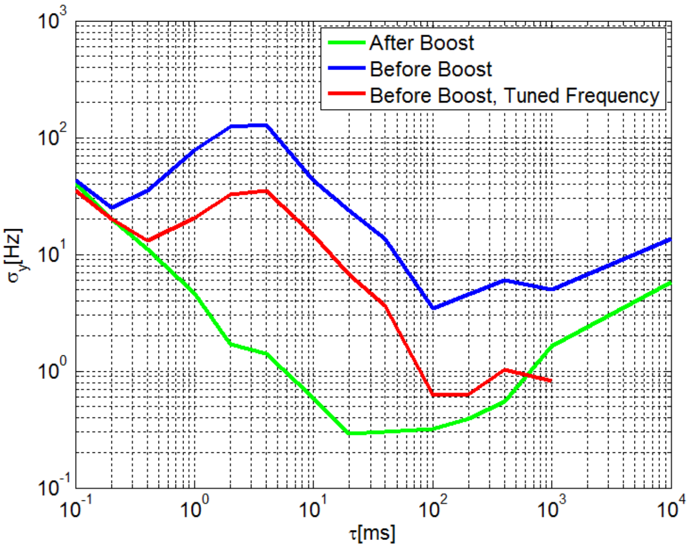

Figure 4.20: Comparison of Allan deviations between after and before force modulation. The increase in Allan deviations between 1ms and 10 ms is due to the spikes of the phase noise between 100 and 1000 Hz offset in Figure 4.19.

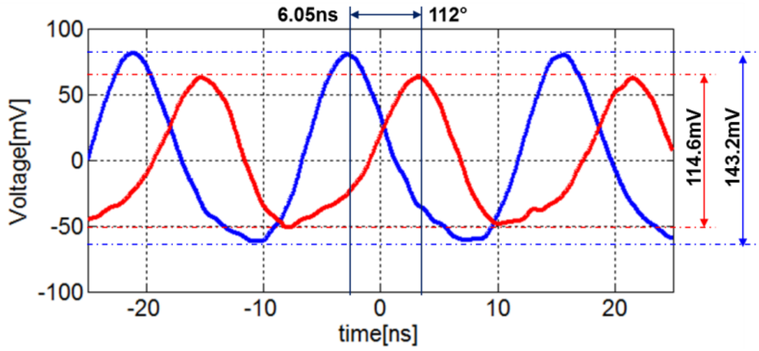

Figure 4.21: Comparison of waveforms at Osc1 (red) and Osc2 (blue).

CHAPTER 5: EXTERNAL ELECTRONIC MODULATION AND ITS APPLICATION IN THE SYNTHESIS OF CIRCULATORS

Conventionally, RF front-ends rely on either time-division duplexing (TDD) or frequency-division duplexing (FDD) to isolate receiver and transmitter paths [8]. This means that they transmit and receive either at different times, or over different frequency bands. However, considering the limitation in the available electromagnetic (EM) spectrum, these approaches are inefficient. An alternative approach is to replace the conventional duplexers with circulators, which allow simultaneous transmit and receive (STAR) at the same frequency and thus increase the efficient utilization of the electromagnetic spectrum. Circulators, though, are usually implemented by passive nonreciprocal ferrite materials, which are bulky and cannot be integrated on chip, hence making STAR impractical in hand-held devices. Non-reciprocity can also be achieved by transistor-based networks, but they exhibit poor linearity and noisy performance [106]. Recently, circulators based on angular momentum biasing [107] and staggered commutation [108] have been investigated. The former is limited by the low modulation ratio and nonlinearity of varactors, while the latter requires high Q off-chip inductors to reduce its waveguide length (~30cm).

This chapter proposes, models, and demonstrates a novel and generalized circulator topology by using linear time-invariant (LTI) network based on integratable filters (for example, AlN MEMS filters) and CMOS RF switches. This topology ensures high modulation ratio, improving the linearity, and simultaneously reducing the size of the circulator, thus constituting a significant step forward towards building in-band full-duplexers (IBFD) and more efficient utilization of the EM spectrum.

5.1. Proposed Circulator Topology

Reciprocity is a fundamental property of linear time-invariant (LTI) electrical networks. To break reciprocity, one common way is to introduce time-variant components. Figure 5.1a shows the schematic representation of the proposed circulator: two identical LTI networks (blue and black colors) with 3-fold rotational symmetry are parametrically modulated by a switch matrix. The modulation signals used to drive the switches of the black branch are shown in Figure 5.1b, which are three digital pulse trains with the same period but a phase difference of 120° with respect to each other. This modulation technique is defined as "spatiotemporal modulation". The modulation signals of the blue branch complement that of the black one such that the RF input from the antenna is commutated between the two branches. It is the parametric modulation of the two branches that renders the network non-reciprocal. As shown in Figure 5.2, the parametric modulation up-converts and down-converts the RF carrier frequency, ω_{RF}, to many intermodulation frequencies, $\omega_{RF} + n\omega_0$, where n is an integer and ω_0 (= $2\pi/T_0$) is the modulation frequency, thus generates different "paths" for power transfer from one port to the other two ports. Part of the RF power from antenna (Port 1) can be transferred to the receiver/transmitter (Port2/3) directly without any frequency conversion. The rest of the power is first up/down converted to the intermodulation frequencies at Switch S_1, and then down/up converted to the RF carrier frequency at S_2 and S_3. Because of different phase shifts introduced in different paths (due to modulation phase and filter spectral phase), the signals can be made to add up constructively when flowing in a particular direction (e.g. from the antenna to the receiver), and destructively when in another (e.g. from the transmitter to the receiver). The effectiveness of the non-reciprocity is controlled by the frequency, ω_0, and duty cycle, α, of the modulation. These aspects of non-reciprocal network are explained in more details in the following sections.

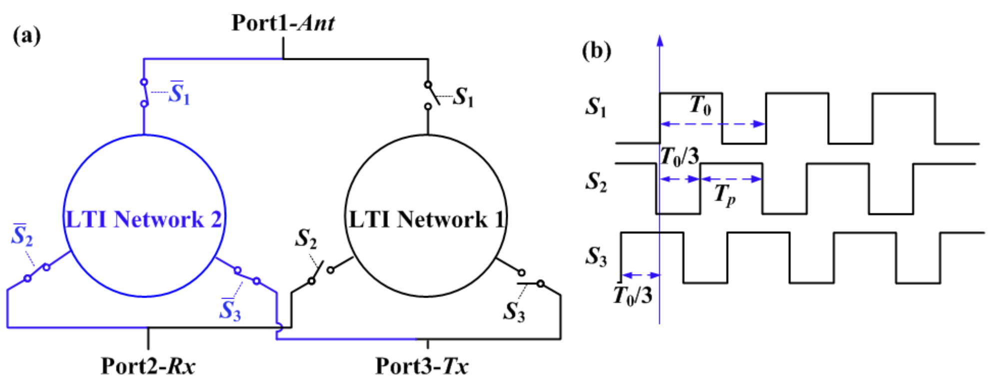

Figure 5.1: (a) Schematic representation of proposed non-reciprocal network based on the parametric modulation of two identical LTI networks (1 and 2) with 3-fold rotational symmetry. (b) The 120° rotational phase relationships between modulation signals (square wave pulses). T_0 is the modulation period (1/frequency) and T_p is the pulse width. Duty cycle, α, is defined by the ratio of T_p to T_0.

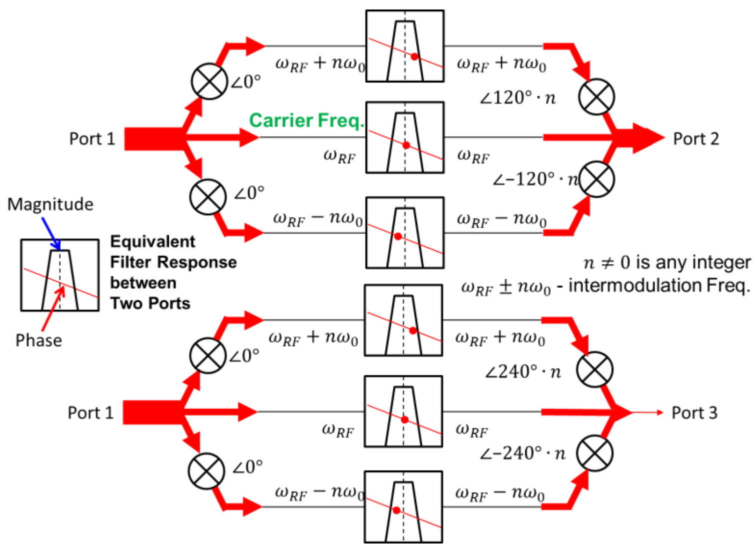

Figure 5.2: Schematic representation of different phase shifts of power transfer in different "paths".

5.2. Circulator Model and Verification

Unfortunately, there are no generalized analytical models for describing the behavior of circulators with high modulation ratio. In this thesis, the modulation ratio of a modulation signal is defined as the ratio of first harmonic amplitude of the Complex Fourier Transform to the average amplitude. For a switch turned on and off with a duty cycle of α, the modulation ratio is $|\mathrm{sinc}(\alpha\pi)| \in [0,1]$. For example, $|\mathrm{sinc}(\alpha\pi)| = 0.64$ when $\alpha = 0.5$. The analytical models developed in [107, 109] can only deal with the particular circulator topologies described in that work. Any slight change in the circuit topology requires a new derivation of the mathematical equations. Moreover, they are valid for small modulation ratio (typically < 0.05) and sinusoidal modulation pattern, where it is enough to consider only three intermodulation frequencies, ω_{RF}, $\omega_{RF} \pm \omega_0$. In contrast, for the switch modulation (square modulation pattern), it is necessary to take more than 25 intermodulation products into account to accurately predict the circulator response.

In terms of universal simulation, Harmonic Balance (HB) is a nonlinear, frequency-domain, steady-state method, hence appears naturally suitable for predicting the proposed circulators' behaviors, which is frequently described by S-parameters. However, these simulations are tedious to setup and take long time to find the converged solutions, especially true when it comes to an accurate solution (requires more harmonic tones) and a large number of frequencies of interest. What is worst, it is hard to get insights in the generation of non-reciprocity by the parametric modulation from HB simulations.

Therefore, we aim at deriving a generalized analytical model and corresponding algorithms to accurately and efficiently predict the proposed circulator's behavior and verifying it by comparing to experimental results. As we will see later, the analytical model offers insights in the generation of non-reciprocity by the parametric modulation, and is agnostic of the LTI network and the switch performance. Admittedly, the scope of the analytical model in this thesis focuses on the prediction of circulator performance given the performance of the LTI networks and the switches, rather than providing insight in the design of a good circulator, which is driven by the design of the LTI network and the switch matrix.

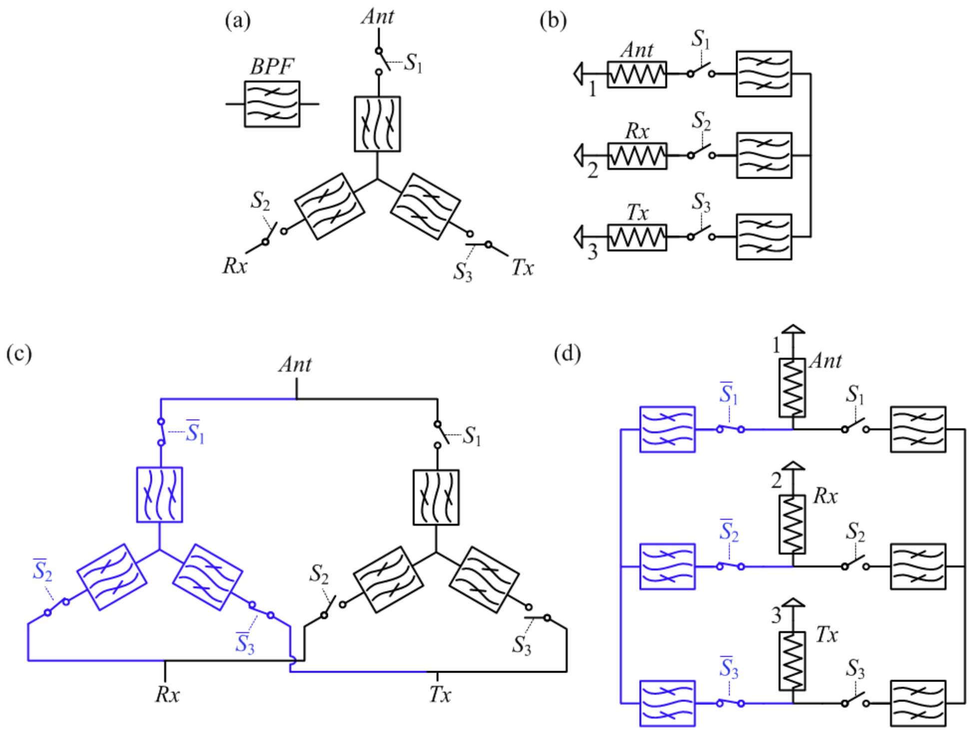

Figure 5.3: (a) Schematic representation of a single-branch switch-filter-based circulator used in the front-ends. (b) The folded representation of circulator in (a) with resistive modeling of antenna, receiver and transmitter. (c) Schematic representation of a double-branch switch-filter-based circulator. (d) The folded representation of circulator in (c).

For convenience in presenting the analytical model, a star-shaped filter network with 3-fold rotational symmetry is employed to embody the general LTI networks of Figure 5.1. But one should keep in mind that the following derivation is independent of how the LTI network is implemented. Firstly, the analysis will be performed on one half of the circulator as shown in Figure 5.3a and b, and then on the full circulator as shown in Figure 5.3c and d. In this thesis, we call them single-branch and double-branch circulator, respectively. Compared to the single-branch circulator, which blocks the antenna signal for a fraction equal to (1 – α) of the modulation signal period, T_0, the double-branch counterpart is a more efficient approach whereby two set of switches are driven by three pairs of differential modulation signals, thus "commutating" the antenna input to the receiver through two filter networks.

5.2.1. Compact Switch Model with Modulation Effect

To build the circulator model, the most important aspect is to model the switch behavior with modulation effect, which becomes particularly complex when the switch interacts with energy storage elements, such as L-C-R circuits and mechanical resonators. To model the switch behavior, we start with the switch I-V relationship under modulation. It is assumed that the switch admittance spectrum is equal to $y_S(\omega)$ Siemens when in the on state and 0 Siemens when in the off state. We neglect any shunt parasitics to ground. With an applied voltage of $u_S(t)=U_S e^{j\omega_{RF}t}$ at the carrier frequency, ω_{RF}, across the switch, the corresponding excited steady current, I (assuming I exists), in the time domain is

$$I(t)=\mathfrak{I}^{-1}\left[y_S(\omega)\right]*y(t)u_S(t) \tag{5.1}$$

where $\mathfrak{I}^{-1}(\cdot)$ represents the inverse Fourier transform, $y(t)=rect\left(\frac{t}{\alpha T_0}-\frac{1}{2}\right)*\sum_{n=-\infty}^{+\infty}\delta\left(t-nT_0-\tau\right)$ is a square wave with an amplitude of 1 as shown in Figure 5.4, $\tau = T_0\cdot\theta/(2\pi)$ is the time delay (not shown in the figure), and θ is the corresponding phase delay.

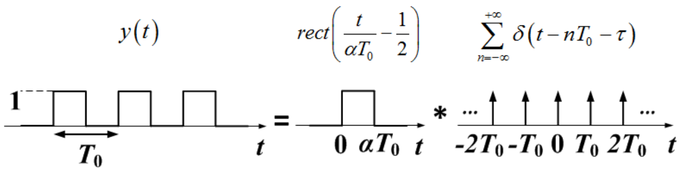

Figure 5.4: Decomposition of a square wave when the time delay τ = 0. Rectangular function $rect(x)=\begin{cases}0, & |x|>0.5\\ 1, & |x|\le 0.5\end{cases}$.

The representation of a square wave by complex Fourier series can be written as

$$y(t)=\sum_{n=-\infty}^{+\infty} c_n e^{-jn\theta} e^{jn\omega_0 t} \tag{5.2}$$

where $c_n=\frac{1}{T_0}\int_0^{T_0} rect\left(\frac{t}{\alpha T_0}-\frac{1}{2}\right)e^{-jn\omega_0 t}dt=\frac{1}{j2n\pi}\left(1-e^{-j2\alpha n\pi}\right)$, and particularly, $c_0 = \alpha$, which is the duty cycle. Therefore,

$$\begin{aligned}
I(t) &= \Im^{-1}\left[y_S(\omega)\right]*y(t)u_S(t)\\
&=\alpha y_S(\omega_{RF})U_S e^{j\omega_{RF}t}+\left[\sum_{n\neq 0} c_n e^{-jn\theta} y_S(\omega_{RF}+n\omega_0)U_S e^{j(\omega_{RF}+n\omega_0)t}\right]\\
&=y_S(\omega_{RF})U_S e^{j\omega_{RF}t}+\left[(\alpha-1)y_S(\omega_{RF})U_S e^{j\omega_{RF}t}+\sum_{n\neq 0} c_n e^{-jn\theta} y_S(\omega_{RF}+n\omega_0)U_S e^{j(\omega_{RF}+n\omega_0)t}\right]\\
&=i_{S,0}e^{j\omega_{RF}t}+\sum_{n=-\infty}^{+\infty} i_{C,n}e^{j(\omega_{RF}+n\omega_0)t}
\end{aligned} \tag{5.3}$$

where $i_{S,0}=y_S(\omega_{RF})U_S, i_{C,n}=\frac{y_S(\omega_{RF}+n\omega_0)}{y_S(\omega_{RF})}e^{-jn\theta}c_n i_{S,0}\,(n\neq 0), i_{C,0}=(\alpha-1)i_{S,0}$. From Eq. (5.3), infinite intermodulation products (ω_{RF} + $n\omega_0$ where n is integer, which are called “modulation index” in this thesis) are generated due to the mixing effect. The first term $i_{S,0}e^{j\omega_{RF}t}$ obeys the Ohm’s law as if a voltage $U_S e^{j\omega_{RF}t}$ is applied across an equivalent resistor of $\left[y_S(\omega_{RF})\right]^{-1}$ Ohms, while the rest can be treated as current controlled current sources (CCCSs) with signal of $i_{C,n}e^{j(\omega_{RF}+n\omega_0)t}$ dependent on $i_{S,0}$ at the intermodulation frequencies, $(\omega_{RF}+n\omega_0)$, in parallel with the equivalent resistance of the switch, as shown in Figure 5.5a and b. Eq. (5.3) also implies that once there is current $i_{S,n}e^{j(\omega_{RF}+n\omega_0)t}$ flowing through the equivalent resistor, CCCSs are generated correspondingly. Upon the interaction of current sources with external circuits, the current sources inject currents into the equivalent resistor, then causing another iteration of mixing processes. This process repeats until the circuit currents and voltages converge to a steady state. In this state, there are infinite intermodulation frequency currents flowing through the equivalent resistor in parallel with infinite intermodulation frequency CCCSs, which are represented in a compact form as shown in Figure 5.5c. For convenience, the vectors comprised of current phasors (frequency information is omitted but implied by the positions and subscripts of phasors) are used to represent the circuit states. In this thesis, we call them phasor vectors. The steady-state currents, I_S and I_C, can be decomposed into the sum of infinite iterative currents, $I_{S,m}$, and $I_{C,m}$, respectively, where m represents the iteration number.

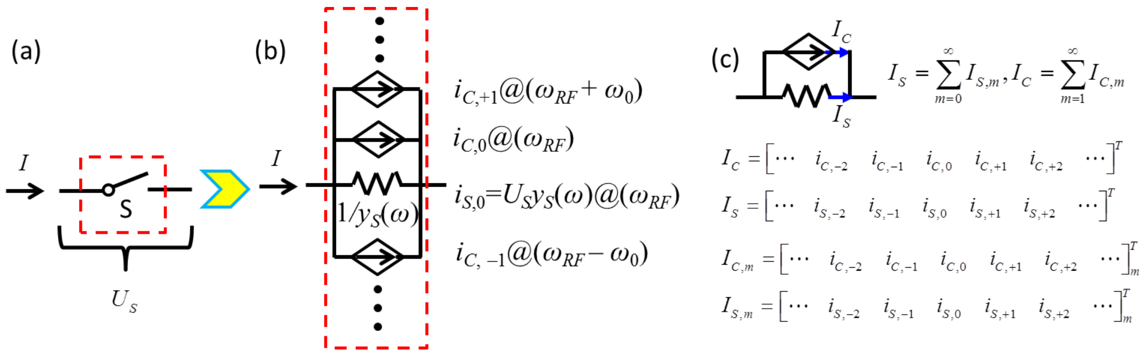

Figure 5.5: (a) Current is induced by a voltage across the switch at the initial iteration. (b) The equivalent circuit of the switch formed by a resistor of $1/y_S(\omega)$ Ohms and infinite CCCSs at the initial iteration. (c) The equivalent circuit of the switch formed by a resistor of $1/y_S(\omega)$ Ohms and a CCCS accounting for infinite harmonics and infinite iterations.

Now, let us consider the interaction between a switch and a general LTI electrical network, as shown in Figure 5.6a. The circuit states can be completely described by phasor vectors, I_{P0}, I_{S0}, and I_{C0}, which are the sum of all the corresponding iterative currents, $I_{P0,m}$, $I_{S0,m}$, and $I_{C0,m}$, respectively. It is important to note that high-order intermodulation terms in the circuit state vectors are truncated to make the numerical computation feasible. Therefore, in Figure 5.6a, only ($2N$ + 1) intermodulation frequencies, *i.e.* from $\left(\omega_{RF}-N\omega_0\right)$ to $\left(\omega_{RF}+N\omega_0\right)$, are taken into account. The iterative currents are correlated by the frequency mixing due to the switch modulation and the transfer functions of the LTI network, $Q(\omega)$ and $R(\omega)$, defined in Figure 5.6b. Expressing these relationships in quantitative equations produces

$$I_{C0,m+1}=\mathbf{Y}_S\left(\omega_{RF},\omega_0\right)\mathbf{C}(\alpha,\theta)\left[\mathbf{Y}_S\left(\omega_{RF},\omega_0\right)\right]^{-1}I_{S0,m} \tag{5.4}$$

and

$$I_{S0,m+1}=\mathbf{F}_Q\left(\omega_{RF},\omega_0\right)I_{C0,m+1} \tag{5.5}$$

$$I_{P0,m+1}=\mathbf{F}_R\left(\omega_{RF},\omega_0\right)I_{C0,m+1} \tag{5.6}$$

where

$$\mathbf{Y}_S\left(\omega_{RF},\omega_0\right)=diag\left[y_{S0}\left(\omega_{RF}-N\omega_0\right)\ \ldots y_{S0}\left(\omega_{RF}-\omega_0\right)y_{S0}\left(\omega_{RF}\right)y_{S0}\left(\omega_{RF}+\omega_0\right)\ \ldots y_{S0}\left(\omega_{RF}+N\omega_0\right)\right],$$

$$\mathbf{C}(\alpha,\theta)=\begin{bmatrix} \alpha-1 & e^{j\theta}c_{-1} & \cdots & e^{jk\theta}c_{-k} & \cdots & e^{j(2N)\theta}c_{-2N} \\ e^{-j\theta}c_1 & \alpha-1 & \cdots & e^{j(k-1)\theta}c_{-k+1} & \cdots & e^{j(2N-1)\theta}c_{-2N+1} \\ \vdots & \vdots & \ddots & \vdots & \cdots & \vdots \\ e^{-jl\theta}c_l & e^{-j(l-1)\theta}c_{l-1} & \cdots & C_{lk}(\alpha,\theta) & \cdots & e^{j(2N-l)\theta}c_{-2N+l} \\ \vdots & \vdots & \cdots & \vdots & \ddots & \vdots \\ e^{-j(2N)\theta}c_{2N} & e^{-j(2N-1)\theta}c_{2N-1} & \cdots & e^{-j(2N-k)\theta}c_{2N-k} & \cdots & \alpha-1 \end{bmatrix}, C_{lk}(\alpha,\theta)=\begin{cases} \alpha-1, & l=k \\ e^{-j(l-k)\theta}c_{l-k}, & l\neq k \end{cases},$$

$$\mathbf{F}_X\left(\omega_{RF},\omega_0\right)=diag\left[X\left(\omega_{RF}-N\omega_0\right)\ \cdots\ X\left(\omega_{RF}-\omega_0\right)\ X\left(\omega_{RF}\right)\ X\left(\omega_{RF}+\omega_0\right)\ \cdots\ X\left(\omega_{RF}+N\omega_0\right)\right],$$

and $X(\omega)$ represents either $Q(\omega)$ or $R(\omega)$. In the following sections, we will use $\mathbf{F}_X$ and $\mathbf{Y}_S$ to represent $\mathbf{F}_X\left(\omega_{RF},\omega_0\right)$ and $\mathbf{Y}_S\left(\omega_{RF},\omega_0\right)$ to make the equations compact but without the loss of clarity. It is interesting to note that $\mathbf{C}(\alpha,\theta)$ is asymmetric when α is neither 0 nor 1, which is the root cause of the non-reciprocity. This can be proven by contradiction. If the circuit in Figure 5.6a is reciprocal, then all the matrix correlating currents at different locations should be symmetric. However, the opposite is true, therefore, the circuit in Figure 5.6a is non-reciprocal. This statement will become clearer in the following sections.

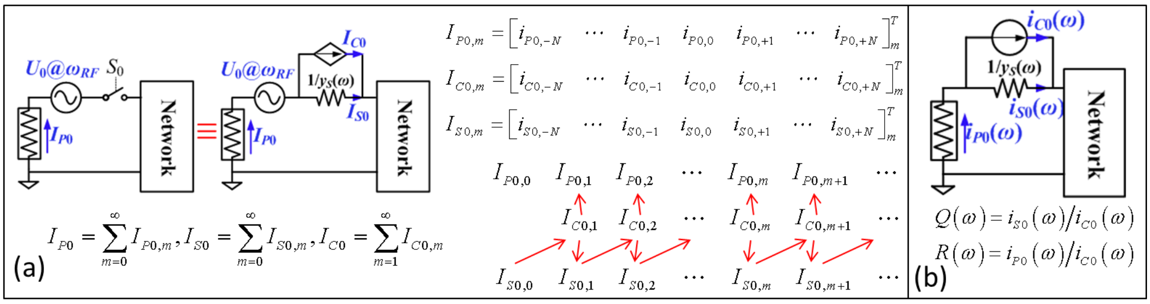

Figure 5.6: (a) The switch in a circuit and its corresponding equivalent circuit. I_{P0}, I_{S0}, and I_{C0} are the steady current of the port, the equivalent resistor, and the CCCS, respectively. Each current is the sum of its corresponding iterative currents, $I_{P0,m}$, $I_{S0,m}$, or $I_{C0,m}$. $I_{P0,0}$ and $I_{S0,0}$ are the circuit response without modulation. It is important to note that all components of $I_{P0,0}$ and $I_{S0,0}$ are zero except their elements at carrier frequency, which are represented by $[i_{P0,0}]_0$ and $[i_{S0,0}]_0$, respectively. (b) The definition of a characteristic transfer function $Q(\omega)$ and its correlation to current source, i_{C0}, and the respondent currents, i_{S0}, and i_{P0}.

Eq. (5.4)-(5.6) are the switch model based on the iterative circuit states. The disadvantage is the potential divergence issue when taking the summation of these iterative terms to the circuit steady states. To bypass this issue, we will deduce an alternative formula of the switch from the iterative equations. Taking the summation of Eq. (5.4) from m = 0 to m = M produces

$$\sum_{m=0}^{M} I_{C0,m+1} = \sum_{m=0}^{M} \mathbf{Y}_S \mathbf{C}(\alpha,\theta)(\mathbf{Y}_S)^{-1} I_{S0,m} \tag{5.7}$$

By taking the limit when M approaches infinity as well as combining $I_{S0} = \sum_{m=0}^{\infty} I_{S0,m}$ and $I_{C0} = \sum_{m=1}^{\infty} I_{C0,m}$, we have

$$I_{C0} = \mathbf{Y}_S \mathbf{C}(\alpha,\theta)(\mathbf{Y}_S)^{-1} I_{S0} \tag{5.8}$$

This equation correlates I_{C0} to I_{S0}, which means that a switch can be modeled by an equivalent resistor in parallel with a CCCS without resorting to the iterative currents. Eq. (5.8) also indicates that the switch model relies on only its own parameters and is independent of the LTI network, thus is valid for its interaction with any LTI network. Similarly, taking the summation of Eq. (5.6) from m = 0 to m = M produces

$$\sum_{m=0}^{M} I_{P0,m+1} = \sum_{m=0}^{M} \mathbf{F}_R I_{C0,m+1} \tag{5.9}$$

Adding $I_{P0,0}$ to both sides of Eq. (5.9), taking the limit when M approaches infinity, and applying $I_{P0} = \sum_{m=0}^{\infty} I_{P0,m}$, we have

$$I_{P0} = I_{P0,0} + \mathbf{F}_R I_{C0} \tag{5.10}$$

This equation states that the steady port current, I_{P0}, is comprised of two parts: the port current without modulation, $I_{P0,0}$, and the contribution of the switch's CCCS to the port, $\mathbf{F}_R I_{C0}$. Now, the key problem is to find the steady currents, I_{S0}, flowing through the switch's equivalent resistor. Again, taking the summation of Eq. (5.5) from m = 0 to m = M produces

$$\sum_{m=0}^{M} I_{S0,m+1} = \sum_{m=0}^{M} \mathbf{F}_Q I_{C0,m+1} \tag{5.11}$$

Adding $I_{S0,0}$ to both sides of Eq. (5.11) and taking the limit when M approaches infinity, we have

$$I_{S0} = I_{S0,0} + \mathbf{F}_Q I_{C0} \tag{5.12}$$

Interestingly, this equation states that the steady resistor current, I_{S0}, is comprised of two parts: the switch current without modulation, $I_{S0,0}$, and the contribution of the switch's CCCS to the equivalent resistor, $\mathbf{F}_Q I_{C0}$. Combining Eq. (5.8) and (5.12), the steady resistor current can be calculated by

$$I_{S0} = \left[\mathbf{I}_d - \mathbf{F}_Q \mathbf{Y}_S \mathbf{C}(\alpha,\theta)(\mathbf{Y}_S)^{-1} \right]^{-1} I_{S0,0} \tag{5.13}$$

where $\mathbf{I}_d$ is a (2N + 1) order identity matrix. Hence, the steady currents of the switch equivalent resistor with modulation, I_{S0}, are related to the steady currents without modulation, $I_{S0,0}$.

To wrap up, Eq. (5.8) describes the switch's equivalent model, while Eq. (5.10), (5.12), and (5.13) formulate the interaction between a switch and a general LTI network. It should be highlighted that this is a generalized model valid for any LTI network. From Eq. (5.10) and (5.12), we know that the CCCS in the switch model interacts with the LTI network in the same way as common current sources.

5.2.2. Single-Branch Circulator Model

We start by modeling the response of the single-branch circulator and computing the S-parameters of the non-reciprocal network. A single-tone voltage source excites the circuit at Port 1 (Antenna), as shown in Figure 5.7a. From the above analysis of the switch, we know that we can replace the switches with resistors and CCCSs (see Figure 5.7b). This circuit can be solved by applying the linear superposition theory, and is related to the circulator response without modulation (see Figure 5.7c).

For convenience, we firstly define *p*-functions for the circuit in Figure 5.8a:

$$P_I(\omega) = \frac{i_{P1}}{u_1}, P_{IJ}(\omega) = \frac{i_{P2}}{u_1} = \frac{i_{P3}}{u_1} \tag{5.14}$$

as well as *q*- and *r*-functions from circuit in Figure 5.8b:

$$Q_I(\omega) = \frac{i_{S1}}{i_1}, Q_{IJ}(\omega) = \frac{i_{S2}}{i_1} = \frac{i_{S3}}{i_1} \tag{5.15}$$

$$R_I(\omega) = \frac{i_{P1}}{i_1}, R_{IJ}(\omega) = \frac{i_{P2}}{i_1} = \frac{i_{P3}}{i_1} \tag{5.16}$$

Intuitively, *p*- and *r*-functions describe the fraction of current that each port can absorb from the voltage source and current source, respectively, while *q*-functions indicate the capability of the current source to pump currents into the equivalent resistor. It is interesting to note that, without modulation, $P_I(\omega)$ and $P_{IJ}(\omega)$ are related to the S-parameters ($S_{11}^*, S_{21}^*, S_{31}^*$) of the circuit of Fig. 5.6b in the following way:

$$S_{11}^{*}(\omega)=1-2P_{I}(\omega)Z_0,$$
$$S_{21}^{*}(\omega)=S_{31}^{*}(\omega)=-2P_{IJ}(\omega)Z_0, \tag{5.17}$$

where Z_0 is the characteristic impedance of the circuit.

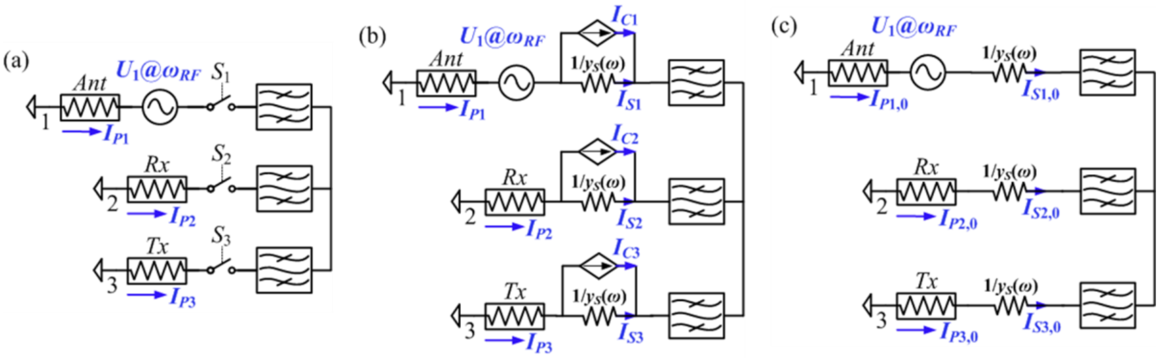

Figure 5.7: (a) Applying excitation source at the antenna and inducing steady currents: $I_{P1\text{-}P3}$. (b) Replacing the switches in (a) with $1/y_S(\omega)$ Ω resistors in parallel with CCCSs. (c) Circuit states without modulation (switches are always on).

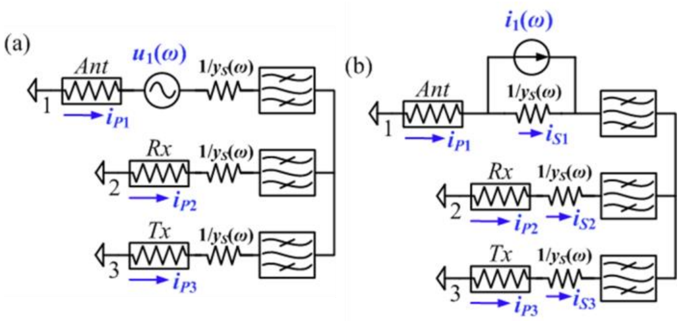

Figure 5.8: (a) The linear circuit used to define *p*-functions. (b) The linear circuit used to define *p*- and *r*-functions.

Table 5.1: Naming Convention of Currents in the Single-Branch Circulator Topology.

Notation	Meaning
I_{Xi}	Steady current of i-th X element with modulation, defined as $I_{Xi}=\begin{bmatrix} i_{Xi,-N} & \cdots & i_{Xi,-1} & i_{Xi,0} & i_{Xi,+1} & \cdots & i_{Xi,+N}\end{bmatrix}^T$, where X represents S (switch equivalent resistor), C (CCCS), or P (port), and i = 1, 2, 3. The current element at the frequency ($\omega_{RF}+n\omega_0$) in I_{Xi} is represented as $i_{Xi,+n}$.
I_X	Steady currents of 3 X elements with modulation, defined as $\begin{bmatrix}(I_{X1})^T & (I_{X2})^T & (I_{X3})^T\end{bmatrix}^T$, where X represents S, C, or P.
$I_{Xi,0}$	Steady current of i-th X element <u>without</u> modulation. X represents S, or P, and i = 1, 2, 3. All components are zero except its element at the carrier frequency. The current element at the frequency ($\omega_{RF}+n\omega_0$) in I_{Xi} is represented as $[i_{Xi,+n}]_0$.
$I_{X,0}$	Steady currents of 3 X elements <u>without</u> modulation, defined as $\begin{bmatrix}(I_{X1,0})^T & (I_{X2,0})^T & (I_{X3,0})^T\end{bmatrix}^T$. X represents S, or P.

By using the naming convention defined in Table 5.1, from Eq. (5.8), (5.10), and (5.12), we have:

$$I_{Ci} = \mathbf{Y}_S \mathbf{C}(\alpha, \theta_i)(\mathbf{Y}_S)^{-1} I_{Si} \tag{5.18}$$

where $\theta_i = (i-1)\dfrac{2\pi}{3}, i = 1, 2, 3$, ands

$$I_{Sr} = I_{Sr,0} + \mathbf{F}_{Q_I} I_{Cr} + \mathbf{F}_{Q_{IJ}} (I_{Cs} + I_{Ct}) \tag{5.19}$$

$$I_{Pr} = I_{Pr,0} + \mathbf{F}_{R_I} I_{Cr} + \mathbf{F}_{R_{IJ}} (I_{Cs} + I_{Ct}) \tag{5.20}$$

due to the 3-fold rotational symmetry, where *r*, *s*, *t* are the permutation of 1, 2, 3. Formulating Eq. (5.18)-(5.20) in a more concise form, we obtain

$$I_C = \tilde{\mathbf{Y}}_s \tilde{\mathbf{C}}_s (\tilde{\mathbf{Y}}_s)^{-1} I_S \tag{5.21}$$

$$I_S = I_{S,0} + \tilde{\mathbf{F}}_{Qs} I_C \tag{5.22}$$

$$I_P = I_{P,0} + \tilde{\mathbf{F}}_{Rs} I_C \tag{5.23}$$

where $\tilde{\mathbf{C}}_s = diag\left[\mathbf{C}(\alpha,\theta_1) \quad \mathbf{C}(\alpha,\theta_2) \quad \mathbf{C}(\alpha,\theta_3)\right]$, $\tilde{\mathbf{Y}}_s = diag\left[\mathbf{Y}_S \quad \mathbf{Y}_S \quad \mathbf{Y}_S\right]$, and $\tilde{\mathbf{F}}_{Xs} = \begin{bmatrix} \mathbf{F}_{X_I} & \mathbf{F}_{X_{IJ}} & \mathbf{F}_{X_{IJ}} \\ \mathbf{F}_{X_{IJ}} & \mathbf{F}_{X_I} & \mathbf{F}_{X_{IJ}} \\ \mathbf{F}_{X_{IJ}} & \mathbf{F}_{X_{IJ}} & \mathbf{F}_{X_I} \end{bmatrix}$, where subscript "*s*" refers to a single-branch circulator and *X* represents either *Q* or *R*. $I_{P,0}$ and $I_{S,0}$ are the circuit response without switching modulation. The non-zero elements in $I_{Pi,0}$ and $I_{Si,0}$ are:

$$\begin{aligned} \left[i_{S1,0}\right]_0 &= \left[i_{P1,0}\right]_0 = P_I U_1 \\ \left[i_{S2,0}\right]_0 &= \left[i_{P2,0}\right]_0 = \left[i_{S3,0}\right]_0 = \left[i_{P3,0}\right]_0 = P_{IJ} U_1 \end{aligned} \tag{5.24}$$

Similarly, the key problem for obtaining the steady states is to solve I_S, which can calculated by combing Eq. (5.21) and (5.22)

$$I_S = \left[\tilde{\mathbf{I}}_d - \tilde{\mathbf{F}}_{Qs} \tilde{\mathbf{Y}}_s \tilde{\mathbf{C}}_s (\tilde{\mathbf{Y}}_s)^{-1}\right]^{-1} I_{S,0} \tag{5.25}$$

where $\tilde{\mathbf{I}}_d$ is a 3(2*N* + 1) order identity matrix. And then I_C and I_P can be easily calculated accordingly. Using $i_{p1,0}$, $i_{p2,0}$, and $i_{p3,0}$ to represent the carrier-frequency currents of Port 1, 2, and 3, respectively, S_{11}, S_{21}, and S_{31} of the single-branch circulator can be expressed as:

$$
\begin{aligned}
S_{11} &= 1 - 2\frac{i_{P1,0}}{U_1} Z_0, \\
S_{21} &= -2\frac{i_{P2,0}}{U_1} Z_0, \\
S_{31} &= -2\frac{i_{P3,0}}{U_1} Z_0.
\end{aligned}
\tag{5.26}
$$

As evident from the derivation process, the analytical model of the single-branch circulator is agnostic of the LTI network and the switch performance. It will be verified later that the circulator model can accurately predict the circulator response given the LTI networks and switches. However, the key performance of the circulator will depend dramatically on the choice of the circuit topology and the LTI network. Hence, for a given modulation scheme, the design of the circulator should boil down to the design of the LTI network, which is out of the scope of this thesis but could be the next contribution coming the same circulator model.

Now, let us qualitatively analyze the non-reciprocity, which can be roughly characterized by a ratio of $|S_{21}/S_{31}|$. Without modulation, the ratio is 1 because the 3-fold rotational symmetry of the topology leads to the equity of $I_{P2,0} = I_{P3,0}$. With modulation ($\alpha \neq 0, 1$), obviously, $\tilde{\mathbf{C}}_s$ is asymmetric while all other matrix are symmetric. Therefore, from Eq. (5.25), it is possible the equity of $I_{S2,0} = I_{S3,0}$ turns to an inequity of $I_{S2} \neq I_{S3}$ by Eq. (5.25), which ultimately propagates to the inequity of $I_{P2} \neq I_{P3}$ by Eq. (5.21) and (5.23), and thus $S_{21} \neq S_{31}$. As expected, the parametric modulation results in the asymmetry of $\tilde{\mathbf{C}}_s$ and ultimately the non-reciprocity of the circuit.

5.2.3. Double-Branch Circulator Model

The derivation of the analytical model that describes the behavior of the double-branch circulator is similar to that of the single-branch circulator. A single-tone voltage source excites the double-branch circulator at Port 1 (Antenna), as shown in Figure 5.9a. From the above analysis of the switch, the switches can be replaced with resistors plus CCCSs (see Figure 5.9b). This circuit can be solved by applying the linear superposition theory, and is related to the circulator response without modulation (see Figure 5.9c). $P_I(\omega)$ and $P_{IJ}(\omega)$ are defined as the previous section (use Eq. (5.14) for the circuit in Figure 5.10a), and they are related to the S-parameters ($S_{11}^*, S_{21}^*, S_{31}^*$) without modulation in the same way. However, the *q*- and *r*-functions for the circuit in Figure 5.10b need to be redefined as:

$$Q_{Iw}(\omega)=\frac{i_{S1w}}{i_1}, Q_{IJw}(\omega)=\frac{i_{S2w}}{i_1}=\frac{i_{S3w}}{i_1}, w=1,2. \tag{5.27}$$

$$R_I(\omega)=\frac{i_{P1}}{i_1}, R_{IJ}(\omega)=\frac{i_{P2}}{i_1}=\frac{i_{P3}}{i_1}. \tag{5.28}$$

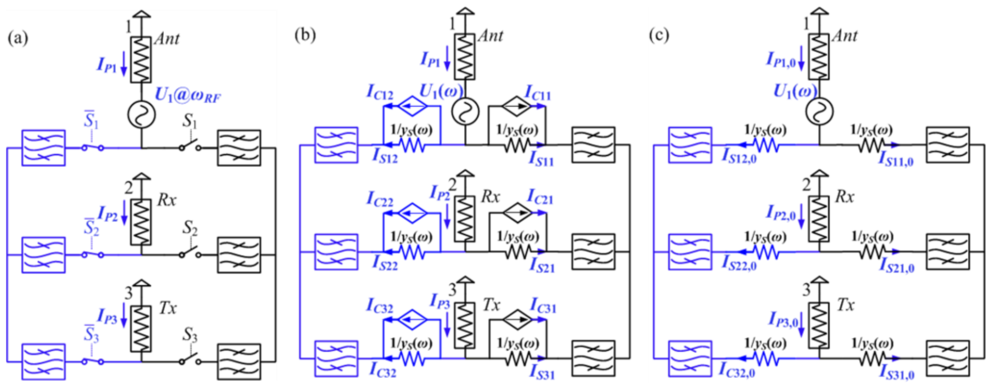

Figure 5.9: (a) Applying excitation source at the antenna and inducing steady currents: $I_{P1\text{-}P3}$. (b) Replacing switches in (a) with $1/y_S(\omega)$ Ω resistors in parallel with CCCSs. (c) Circuit states without modulation (switches are always on).

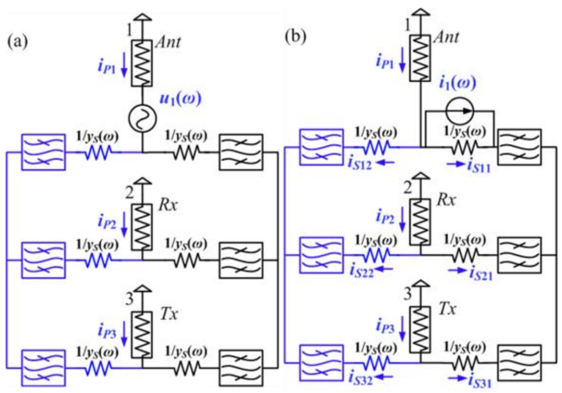

Figure 5.10: (a) The linear circuit used to define *p*-functions. (b) The linear circuit used to define *p*- and *r*-functions.

Table 5.2: Naming Convention of Currents in the Double-Branch Circulator.

Notation	Meaning
I_{Pi}	Steady current of *i*-th port with modulation, defined as $I_{Pi} = \left[i_{Pi,-N} \ \cdots \ i_{Pi,-1} \ i_{Pi,0} \ i_{Pi,+1} \ \cdots \ i_{Pi,+N} \right]^T$, where i = 1, 2, 3. The current element at the frequency ($\omega_{RF} + n\omega_0$) in I_{Pi} is represented as $i_{Pi,+n}$.
I_{Xij}	Steady current of *ij*-th *X* element with modulation, defined as $I_{Xij} = \left[i_{Xij,-N} \ \cdots \ i_{Xij,-1} \ i_{Xij,0} \ i_{Xij,+1} \ \cdots \ i_{Xij,+N} \right]^T$, where X represents S (switch equivalent resistor), or C (CCCS), i = 1, 2, 3, and j = 1, 2. The current element at the frequency ($\omega_{RF} + n\omega_0$) in I_{Xij} is represented as $i_{Xij,+n}$.
I_P	Steady currents of 3 ports with modulation, defined as $\left[\left(I_{P1}\right)^T \ \left(I_{P2,}\right)^T \ \left(I_{P3}\right)^T \right]^T$.
I_X	Steady currents of 6 X elements with modulation, defined as $\left[\left(I_{X11}\right)^T \ \left(I_{X12}\right)^T \ \left(I_{X21}\right)^T \ \left(I_{X22}\right)^T \ \left(I_{X31}\right)^T \ \left(I_{X32}\right)^T \right]^T$.
$I_{Pi,0}$	Steady current of *i*-th port <u>without</u> modulation, where i = 1, 2, 3. All components are zero except its element at the carrier frequency. The current element at the frequency ($\omega_{RF} + n\omega_0$) in I_{Pi} is represented as $[i_{Pi,+n}]_0$.
$I_{Sij,0}$	Steady current of *ij*-th switch's equivalent resistor <u>without</u> modulation, where i = 1, 2, 3 and j = 1, 2. All components are zero except its element at the carrier frequency. The current element at the frequency ($\omega_{RF} + n\omega_0$) in I_{Si} is represented as $[i_{Si,+n}]_0$.
$I_{P,0}$	Steady currents of 3 ports <u>without</u> modulation, defined as $\left[\left(I_{P1,0}\right)^T \ \left(I_{P2,0}\right)^T \ \left(I_{P3,0}\right)^T \right]^T$.
$I_{S,0}$	Steady currents of 6 switches' equivalent resistors <u>without</u> modulation, defined as $\left[\left(I_{S11,0}\right)^T \ \left(I_{S12,0}\right)^T \ \left(I_{S21,0}\right)^T \ \left(I_{S22,0}\right)^T \ \left(I_{S31,0}\right)^T \ \left(I_{S32,0}\right)^T \right]^T$.

After defining the necessary circuit state vectors, from Eq. (5.8), (5.10), and (5.12), we have

$$\begin{aligned} I_{Ci1} &= \mathbf{Y}_S \mathbf{C}\left(\alpha, \theta_i\right)\left(\mathbf{Y}_S\right)^{-1} I_{Si1} \\ I_{Ci2} &= \mathbf{Y}_S \mathbf{C}\left(\overline{\alpha, \theta_i}\right)\left(\mathbf{Y}_S\right)^{-1} I_{Si2} \end{aligned} \tag{5.29}$$

where $\mathbf{C}\left(\overline{\alpha, \theta_i}\right) = \mathbf{C}\left(1-\alpha, 2\alpha\pi + \theta_i\right)$, and i = 1, 2, 3. With the assumption of 3-fold rotational symmetry, there are

$$I_{Srw} = I_{Srw,0} + \mathbf{F}_{Q_{I1}} I_{Crw} + \mathbf{F}_{Q_{I2}} I_{Crv} + \mathbf{F}_{Q_{IJ1}} \left(I_{Csw} + I_{Ctw}\right) + \mathbf{F}_{Q_{IJ2}} \left(I_{Csv} + I_{Ctv}\right) \tag{5.30}$$

$$I_{Pr} = I_{Pr,0} + \mathbf{F}_{R_I} \left(I_{Cr1} + I_{Cr2}\right) + \mathbf{F}_{R_{IJ}} \left(I_{Cs1} + I_{Cs2} + I_{Ct1} + I_{Ct2}\right) \tag{5.31}$$

where r, s, t are the permutation of 1, 2, 3, and w, v are the permutation of 1, 2. Similarly, by rewriting Eq. (5.29)-(5.31) in a compact form we obtain:

$$I_C = \tilde{\mathbf{Y}}_d \tilde{\mathbf{C}}_d \left(\tilde{\mathbf{Y}}_d\right)^{-1} I_S \tag{5.32}$$

$$I_S = I_{S,0} + \tilde{\mathbf{F}}_{Qd} I_C \tag{5.33}$$

$$I_P = I_{P,0} + \tilde{\mathbf{F}}_{Qd} I_C \tag{5.34}$$

where $\tilde{\mathbf{C}}_d = diag\left[\mathbf{C}\left(\alpha,\theta_1\right) \ \ \mathbf{C}\left(\overline{\alpha,\theta_1}\right) \ \ \mathbf{C}\left(\alpha,\theta_2\right) \ \ \mathbf{C}\left(\overline{\alpha,\theta_2}\right) \ \ \mathbf{C}\left(\alpha,\theta_3\right) \ \ \mathbf{C}\left(\overline{\alpha,\theta_3}\right)\right]$,

$\tilde{\mathbf{Y}}_d = diag\left[\mathbf{Y}_S \ \ \mathbf{Y}_S \ \ \mathbf{Y}_S \ \ \mathbf{Y}_S \ \ \mathbf{Y}_S \ \ \mathbf{Y}_S\right]$,

$$\tilde{\mathbf{F}}_{Qd} = \begin{bmatrix} \bar{\mathbf{F}}_{Q_I} & \bar{\mathbf{F}}_{Q_{IJ}} & \bar{\mathbf{F}}_{Q_{IJ}} \\ \bar{\mathbf{F}}_{Q_{IJ}} & \bar{\mathbf{F}}_{Q_I} & \bar{\mathbf{F}}_{Q_{IJ}} \\ \bar{\mathbf{F}}_{Q_{IJ}} & \bar{\mathbf{F}}_{Q_{IJ}} & \bar{\mathbf{F}}_{Q_I} \end{bmatrix}, \text{where } \bar{\mathbf{F}}_{Q_I} = \begin{bmatrix} \mathbf{F}_{Q_{I1}} & \mathbf{F}_{Q_{I2}} \\ \mathbf{F}_{Q_{I2}} & \mathbf{F}_{Q_{I1}} \end{bmatrix}, \bar{\mathbf{F}}_{Q_{IJ}} = \begin{bmatrix} \mathbf{F}_{Q_{IJ1}} & \mathbf{F}_{Q_{IJ2}} \\ \mathbf{F}_{Q_{IJ2}} & \mathbf{F}_{Q_{IJ1}} \end{bmatrix}$$

$$\text{and } \tilde{\mathbf{F}}_{Rd} = \begin{bmatrix} \mathbf{F}_{R_I} & \mathbf{F}_{R_I} & \mathbf{F}_{R_{IJ}} & \mathbf{F}_{R_{IJ}} & \mathbf{F}_{R_{IJ}} & \mathbf{F}_{R_{IJ}} \\ \mathbf{F}_{R_{IJ}} & \mathbf{F}_{R_{IJ}} & \mathbf{F}_{R_I} & \mathbf{F}_{R_I} & \mathbf{F}_{R_{IJ}} & \mathbf{F}_{R_{IJ}} \\ \mathbf{F}_{R_{IJ}} & \mathbf{F}_{R_{IJ}} & \mathbf{F}_{R_{IJ}} & \mathbf{F}_{R_{IJ}} & \mathbf{F}_{R_I} & \mathbf{F}_{R_I} \end{bmatrix},$$

where the subscript "*d*" refers to the double-branch circulators. The different colors in matrix $\tilde{\mathbf{F}}_{Qd}, \tilde{\mathbf{F}}_{Rd}$ map the location of different sub-matrices. $I_{P,0}$ and $I_{S,0}$ are the circuit response without modulation. The non-zero elements in $I_{Pi,0}$ and $I_{Si,0}$ are:

$$\begin{aligned} &\left[i_{P1,0}\right]_0 = P_I U_1, \left[i_{P2,0}\right]_0 = \left[i_{P3,0}\right]_0 = P_{IJ} U_1 \\ &\left[i_{S11,0}\right]_0 = \left[i_{S12,0}\right]_0 = P_I U_1/2 \\ &\left[i_{S12,0}\right]_0 = \left[i_{S13,0}\right]_0 = \left[i_{S22,0}\right]_0 = \left[i_{S23,0}\right]_0 = P_{IJ} U_1/2 \end{aligned} \tag{5.35}$$

Combining Eq. (5.32) and (5.33), I_S can be calculated as

$$I_S = \left[\tilde{\mathbf{I}}_d - \tilde{\mathbf{F}}_{Qd} \tilde{\mathbf{Y}}_d \tilde{\mathbf{C}}_d \left(\tilde{\mathbf{Y}}_d\right)^{-1}\right]^{-1} I_{S,0} \tag{5.36}$$

where $\tilde{\mathbf{I}}_d$ is a 6(2*N* + 1) order identity matrix. Then the S-parameters for double-branch circulator can be obtained using the same Eq. (5.26). Similarly, the analytical model of the double-branch circulator is agnostic of the LTI network and the switch performance and its prediction power will be verified experimentally. However, the methodology of designing the LTI network to produce a good circulator is not readily enabled. It could be derived from the same model, which is out of the scope in this thesis yet. Finally, the non-reciprocity comes from the asymmetry of $\tilde{\mathbf{C}}_d$ due to the parametric modulation, which could be deduced in a similar way as presented in the previous section.

5.2.4. Experimental Verification

To verify the previously described circulator models, we set up the circulators as shown in Figure 5.3a and c by using MiniCitcuits discrete RF high isolation switches, ZFSWHA-1-20+, and bandpass filters, SBP-21.4+. Figure 5.11a and b show the frequency responses of the selected switch and filter, respectively. The filter center frequency is 21.4MHz and its 3dB-bandwidth is 7.4MHz. The *IL* of filter and switch at 21.4MHz are 0.81 dB and 0.61 dB, respectively. As shown in Figure 5.11a, since the magnitudes of y_1 and y_2 are at least 100 times smaller than y_S, it is reasonable to neglect their effect on the results and only take y_S into account as the theoretical models do. The three modulation signals required for the single-branch circulator topology in Figure 5.3a are generated by two synchronized pulse generators, Agilent 81110A. The phase differences between these signals were monitored by a 4-channel oscilloscope, Agilent DSO6014, and are automatically adjusted to be 120° by a MATLAB program. The six normal and complementary modulation signals required for the double-branch circulator topology in Figure 5.3c are generated by a hex inverter, 74HCT04, which includes six independent inverters, with those three square waves from pulse generators as the inputs.

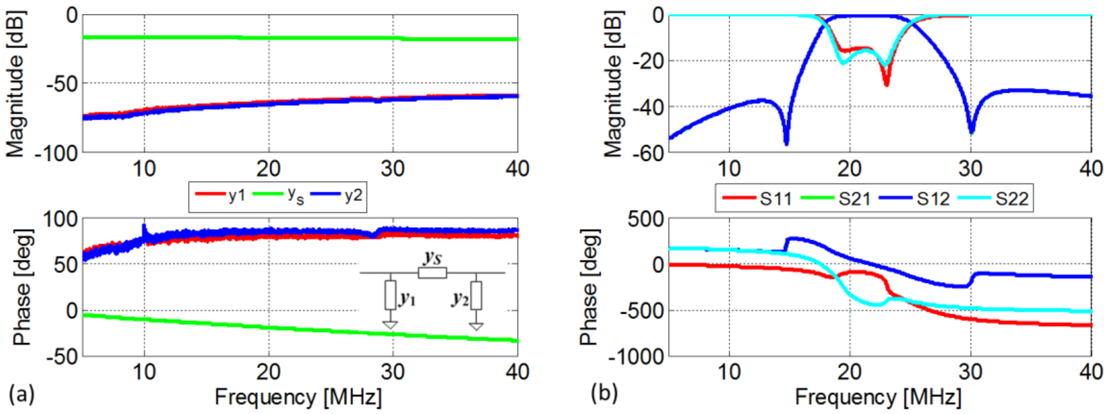

Figure 5.11: (a) π-model of the selected switch when it is on and the frequency response of each element. (b) S-parameters of the selected filter.

Before obtaining the theoretical results from the mathematical models, we simulated *p*- and *q*-functions from Agilent ADS simulation based on the measured responses of switches and filters (Figure 5.11a and b), while *r*-functions can be easily obtained from *q*-functions for the proposed topology via Kirchhoff's Current Law (KCL). For the single-branch circulator topology, the *p*- and *q*-functions are shown in Figure 5.12. Figure 5.13a shows the circulator response without modulation, which looks similar to the one of the standalone filter. The *IL* at 21.4 MHz is 6.52 dB, while the ideal *IL* should have been 3.52dB. The 3 dB difference is due to the intrinsic loss of components and connection cables. After sweeping the modulation frequency and duty cycle, we chose a 0.54 MHz square wave with duty cycle of 45% as the modulation signals in order to impart substantial isolation (>15 dB) between receiver and transmitter and to have a good *IL* . The circulator response with modulation is presented in Figure 5.13b. It is observed that the theoretical results overlap well with the experimental ones. The minor discrepancy originates from the deviation of the circulator from 3-fold rotational symmetry.

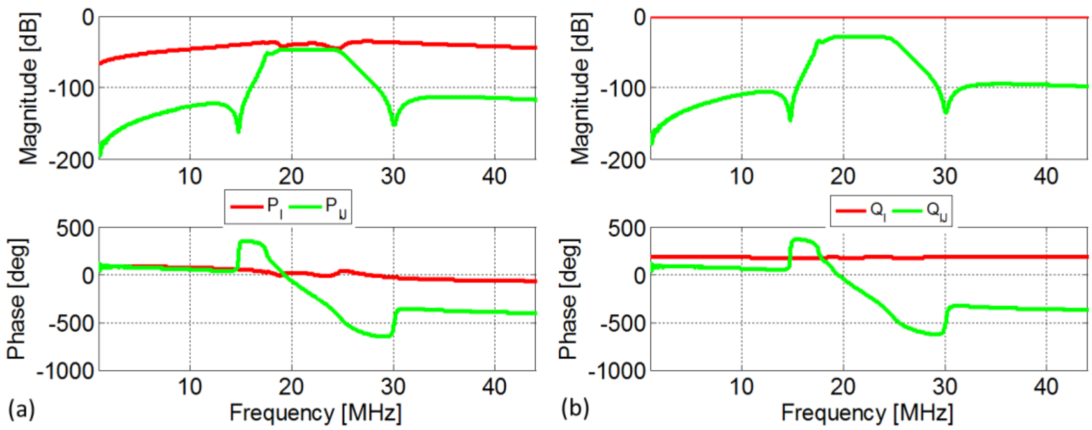

Figure 5.12: (a) The frequency response of P_I and P_{IJ} for the single-branch circulator topology. (b) The frequency response of Q_I and Q_{IJ} for the single-branch circulator topology.

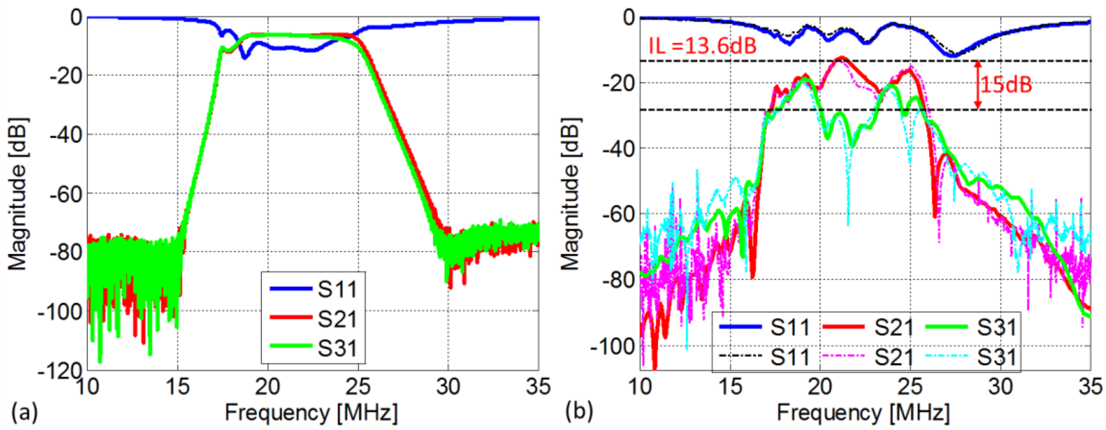

Figure 5.13: (a) The measured response of single-branch topology without modulation. (b) The overlap between theoretical (solid lines) and experimental (dotted lines) responses of the single-branch topology with modulation frequency of 0.54MHz and duty cycle of 45% with N = 16.

The large IL, 13.6 dB, for the single-branch circulator is mainly attributed to the intrinsic loss of components, the modulation loss, and poor matching. The intrinsic loss of components can be roughly estimated by the total loss of two switches in series with two filters, which is around 2.7 dB. A duty cycle of 45% means 55% of energy is not delivered to the load, equivalent to 5.2 dB loss (and which can be accounted as the loss due to the modulation). Meanwhile, a port only sees the corresponding filter αT_0 within a period because the switches toggle on and off, thus increasing the equivalent filter impedance seen by the port. Although the filters are designed to match with 50 Ω, poor matching with port impedance is evident, which is indicated by in-band S_{11} of around –5 dB. The double-branch circulator topology is expected to address these issues and improve IL, because a port always sees the filter within a whole period. Similarly, we obtained p- and q-functions from Agilent ADS simulation as shown in Figure 5.14, as well as r-functions obtained from q-functions for the proposed topology via Kirchhoff's Current Law (KCL). And the corresponding responses of the circulator modulated by the same square waves are shown in Figure 5.15. As expected, IL decreases to 6.4 dB and S_{11} is well below –10 dB. Again, the theoretical results overlap well with the experimental ones apart from minor discrepancies. It is important to note that the modulation loss still exists, because, fundamentally, modulation scatters the carrier-frequency energy over all the intermodulation frequencies. It is possible to cancel the modulation loss by using differential circulator topologies [110]. The analysis of these topologies is beyond the scope of this thesis.

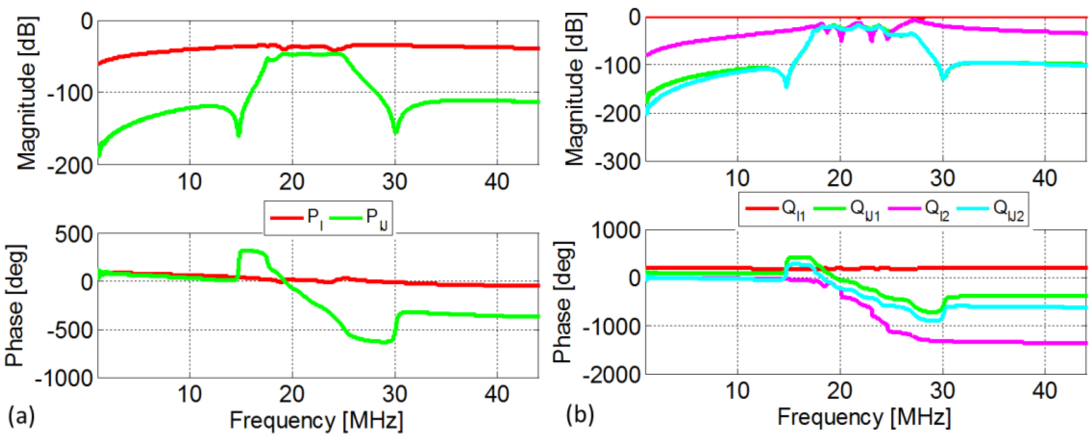

Figure 5.14: (a) The frequency response of P_I and P_{IJ} for the double-branch circulator topology. (b) The frequency response of Q_{I1}, Q_{IJ1}, Q_{I2}, and Q_{IJ2} for the double-branch circulator topology.

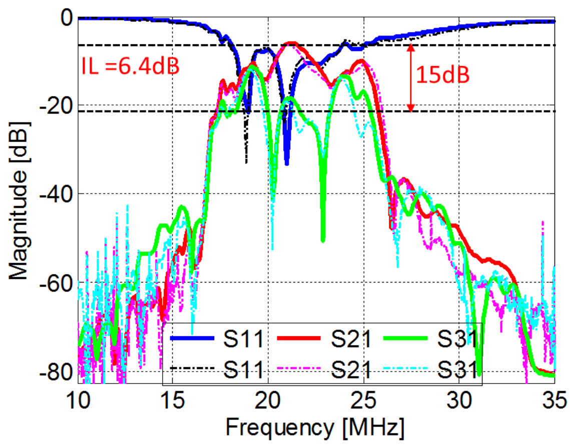

Figure 5.15: (a) The overlap between theoretical (solid lines) and experimental (dotted lines) responses of the double-branch topology with modulation frequency of 0.54MHz and duty cycle of 45% with N = 16.

It is very interesting to see how the modulation parameters affect the circulator performance. Sweeping modulation frequency and duty cycle and overlapping the isolation and *IL* performance produces Figure 5.16a. It can be concluded that there is some trade-off between *IL* and isolation because the best *IL* and the largest isolation occur at different positions. At this point in time, the reason of the trade-off remains unclear. The shaded area is the region where modulation parameters are chosen to offer both good isolation and *IL*. Point A in Figure 5.16a is an example of a circulator operating in this region and its corresponding performance is shown in Figure 5.16b. The *IL* is slightly better than Figure 5.15 while maintaining a similar isolation performance. In addition, Figure 5.16a is supposed to be symmetrical with respect to the duty cycle equal to 50% in the ideal situation. But deviations of the real circuit from the rotational symmetry and the imperfect square waves from the hex inverter contribute to the asymmetry in the circulator performance. These factors are not included in the circulator model, which results in the minor discrepancies between analytical and experimental results.

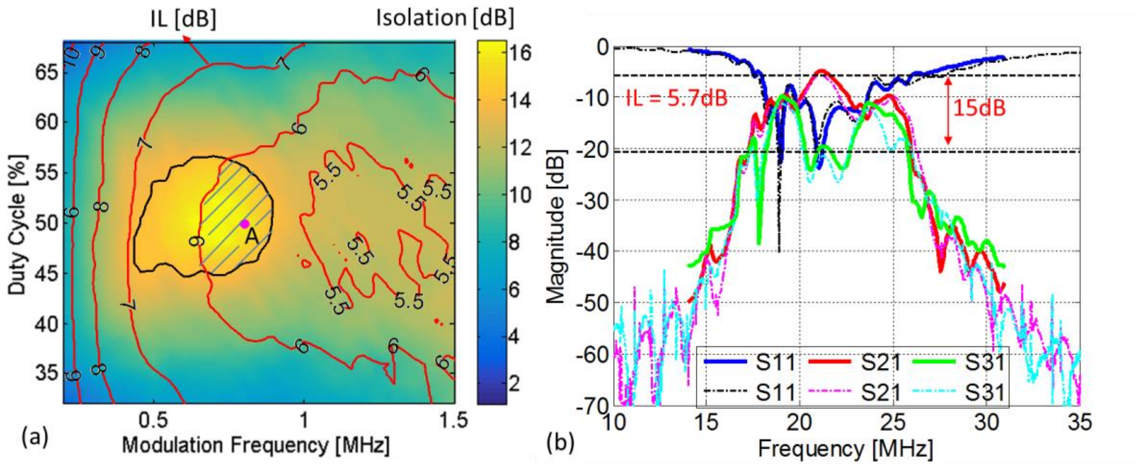

Figure 5.16: (a) The performance in isolation (represented by color) and *IL* (red contour lines) of the double-branch circulator versus modulation frequency and duty cycle. The area within the black contour line is the parameter space that produces isolation larger than 14 dB, while the shaded area is the region that can offer *IL* lower than 6 dB at the same time. (b) The overlap between theoretical (solid lines) and experimental (dotted lines) responses of the double-branch topology with modulation parameters (0.8 MHz, 50%) given by point A in (a).

So far, we prove the validity of our circulator models which can be used to predict circulator behaviors well, given specific switch performance, LTI response, modulation frequency, and duty cycle. It should be emphasized again that no particular LTI network property is used in the derivation of the circulator models. Therefore, the models keep valid for all LTI networks with 3-fold symmetry. Moreover, it is easy to extend the models to account for general LTI networks when quantifying the effect of variations in filter spectrum, port impedance, modulation signal phase shift, etc. The derivation process of the models is also broadly applicable to any circulator topology that is essentially based on the parametric modulation of LTI networks [107-109], which will be shown in Section 6.2.

5.2.5. Comparison with Harmonic Balance Simulations

This section compares the proposed theoretical model to Harmonic Balance (HB) simulations to further prove the effectiveness and efficiency of the theoretical model. HB simulation is a method used to calculate the steady-state response of nonlinear circuits in frequency domain. The circuit states (currents and voltages) are assumed to be a linear combination of multiple tones. A tone refers to a sinusoid at a given frequency. This is the same assumption used by our proposed models. A generalized tutorial on HB simulation can be found in [111].

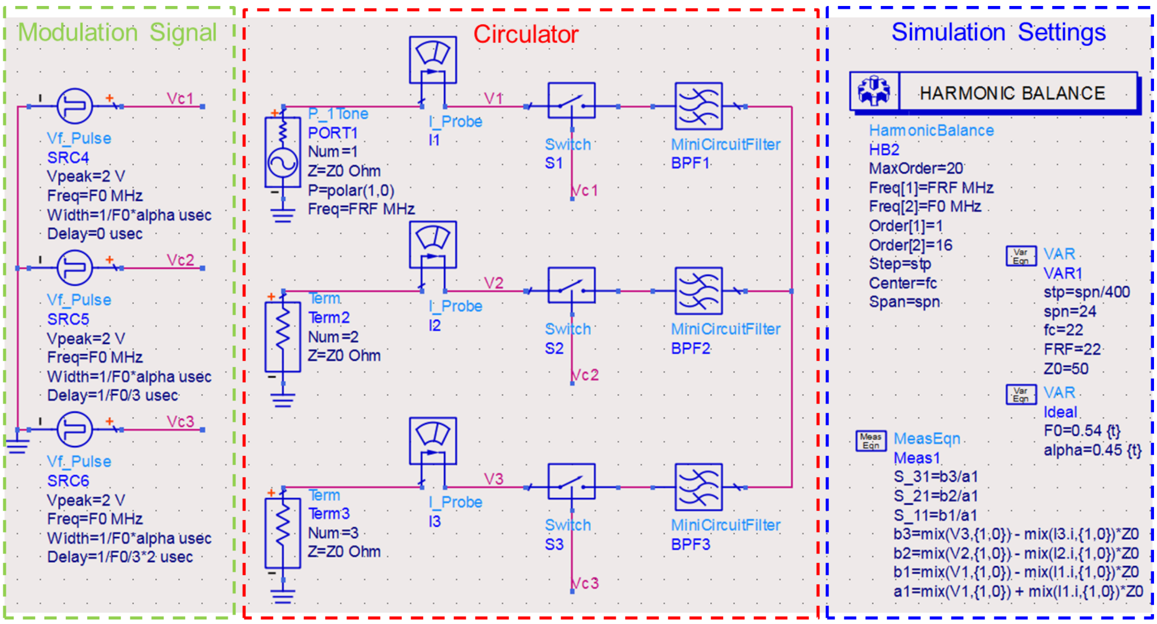

Figure 5.17: HB simulation set-up of single-branch circulator circuit in Agilent ADS. The circuit is excited by a single-tone source, P_1Tone. FRF is the carrier frequency, F0 the modulation frequency, and alpha the duty cycle. Vc*i* is the *i*-th modulation signal, where *i* = 1, 2, 3. The on-impedance of identical Switches takes the

measured data, while the off-impedance is 100 MΩ. The response of identical BPFs also uses measured two-port S-parameters. The number of frequencies over the specified simulation spectrum is 401.

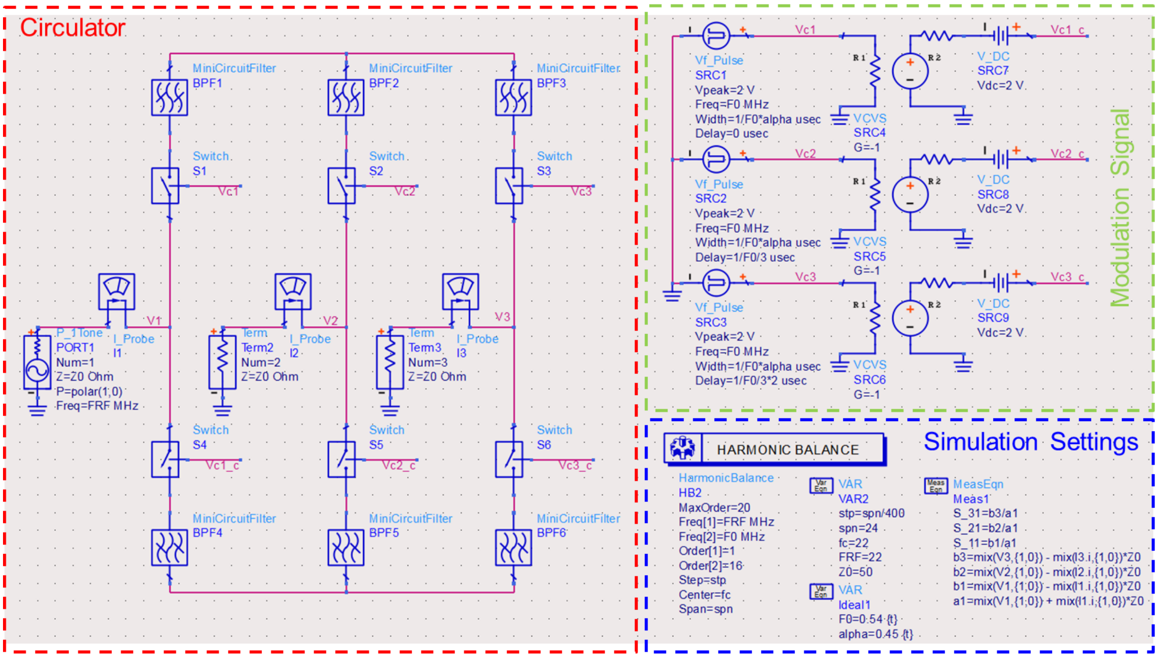

Figure 5.18: HB simulation set-up of double-branch circulator circuit in Agilent ADS. Vc*i*_c is complementary to to Vc*i*, where i = 1, 2, 3. R_1 and R_2 in VCVS are 10^{100} Ω and 0 Ω, respectively. The number of frequencies over the specified simulation spectrum is 401.

Here, we would like to give a brief introduction to the process of how HB simulation analyzes the circulator circuits in Figure 5.7a and Figure 5.10a. The HB simulation setups of single- and double-branch circulators are shown in Figure 5.17 and Figure 5.18, respectively. Order[i] sets the maximum mixing order of Freq[i]. Order[1] = 1 is enough due to the bandwidth of the BPFs. The optimal value of Order[2] needs to be tested to provide not only accurate but also reasonably-fast solutions. In the presented setups, the tones (single side) involved in calculation are: 0, F_0, …, $16F_0$, F_{RF}, $|F_{RF} \pm F_0|$, …, $|F_{RF} \pm 16F_0|$, 50 tones in total. One may notice that the first 17 tones are unnecessary because they are out-of-band for the filters of interest. In contrast, our proposed model only uses 33 tones (two sides): F_{RF}, $F_{RF} \pm F_0$, …, $F_{RF} \pm 16F_0$, which would be more efficient. Once all parameters for the simulation are ready, the HB simulator kicks off with an initial guess of nodal voltages in frequency domain. Then it calculates the linear currents enter the filters and ports in frequency domain. Instead, the HB simulator calculates the nonlinear currents through the switches in time domain because it is easier to express the nonlinear I-V relationship of modulation in time domain. Therefore, it requires to transform the nodal voltages from frequency domain to time domain (Inverse Fourier Transform) as well as to transform nonlinear currents in time domain back to frequency domain (Fourier Transform). The next step is to calculate the difference between the two sets of currents, modify the nodal voltages in frequency domain, and recalculate the currents. To reduce the current difference, Newton-Raphson technique is typically applied to obtain the new guess of nodal voltages. Such process is repeated until KCL is satisfied, in which linear currents are balanced with nonlinear ones. Compared to HB simulation, our model eliminates the transformation of currents and voltages between time and frequency domain back and forth, which saves time and memory. Furthermore, our model calculates the steady-states directly without iterations, which gets rid of potential divergence issues. Lastly but most importantly, our model offers insights in the generation of non-reciprocity, which is not available for HB simulation.

Figure 5.19a and b show the comparison of HB simulations with experimental results for single- and double-branch circulators, respectively. Compared to Figure 5.15 and Figure 5.13b, the proposed models are able to predict the circulator in-band behaviors with better accuracy than HB simulations. Moreover, our theoretical models are much more efficient in prediction than HB simulations. As an example, to analyze the single- and double-branch circulators in Figure 5.17 and Figure 5.18, it takes HB simulation around 75 and 317 seconds, respectively. However, it takes our theoretical models only about 17 and 37 seconds, respectively, for the same maximum mixing order of the modulation frequency and the number of frequencies over the specified spectrum.

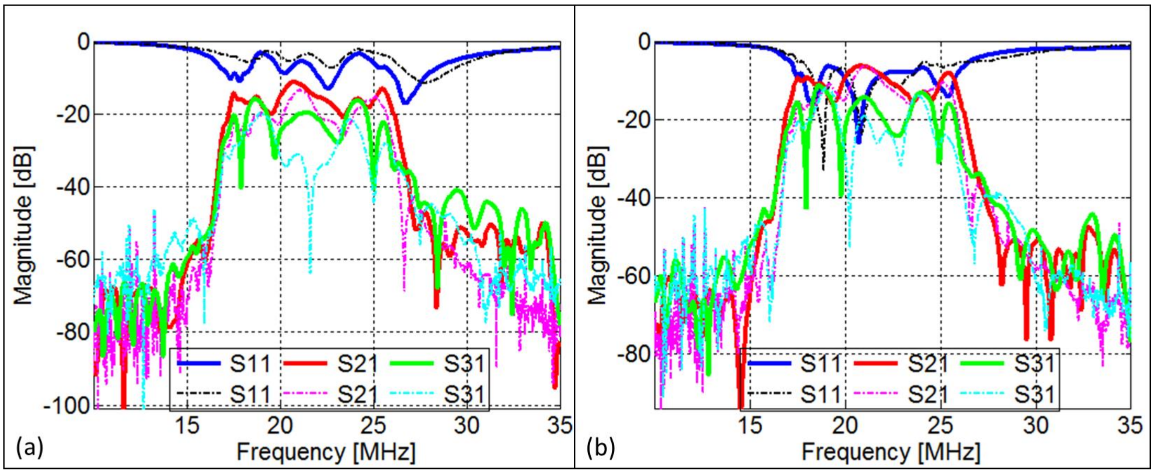

Figure 5.19: The overlap between HB simulations (solid lines) and experiment results (dotted lines) of (a) the single-branch topology and (b) the double-branch topology with modulation frequency of 0.54MHz and duty cycle of 45%.

5.3. Demonstration of Circulators Based on MEMS Resonators

The ultimate goal of magnetic-free circulators is to be integrated in the handheld device in order to facilitate the development of in-band full duplexers (IBFD) for simultaneous transmit and receive (STAR) and double the efficiency of EM spectrum. In this demonstration, we implement a 1.16 GHz circulator with CMOS-integrable components such as AlN MEMS filters [112] and CMOS RF switches, which were mounted on connected PCBs (Figure 5.20). It should be pointed out that the main contribution of this demonstration lies in the synthesis of the first CMOS-integratable MEMS-filter-based circulator as proposed in Figure 5.1a, rather than the analysis and improvement of circulator performance.

The AlN MEMS filters are either first-order (a single two-port AlN MEMS resonator, which exhibits an *IL* of 3.7 dB, as shown in Figure 5.21a) or third-order (three cascaded two-port AlN MEMS resonators, which exhibits an *IL* of 6.6 dB, as shown in Figure 5.22a). Higher-order filters offer wider bandwidth and larger out-of-band rejection. The filters are connected in a Δ-shaped network, as shown in Figure 5.21b and Figure 5.22b. The deviation from identity and 3-fold rotational symmetry is due to variations of wire bonding and PCB designs.

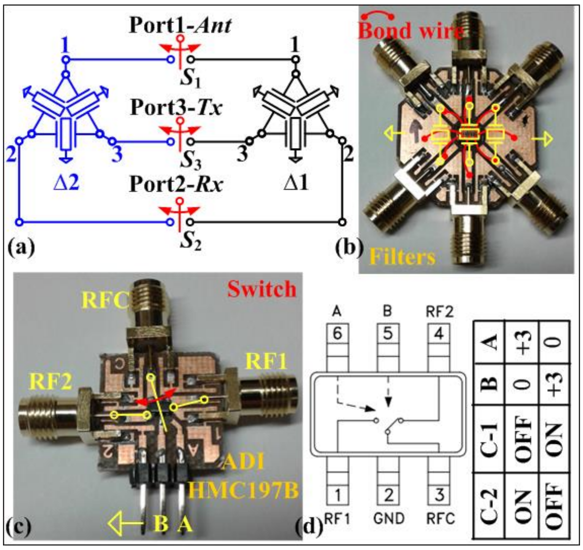

A	B	C-1	C-2
+3	0	OFF	ON
0	+3	ON	OFF

Figure 5.20: (a) The implementation of the circulator of Figure 5.1a. (b) PCB for wire-bonding three AlN MEMS filters. (c) PCB for a single CMOS RF switch. (d) Pin configuration of the CMOS RF switch and the corresponding truth table.

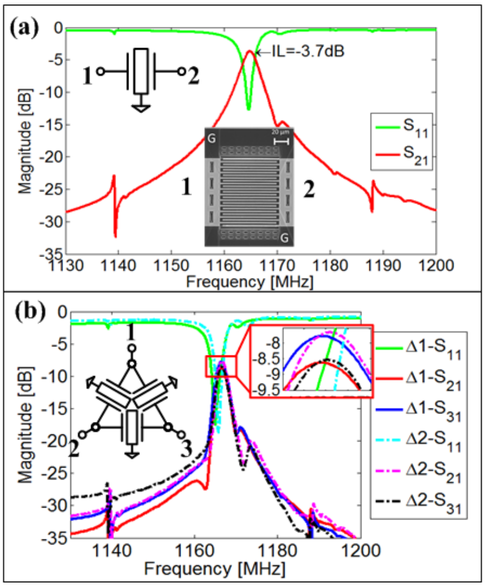

Figure 5.21: (a) The response of a first-order resonant filter wire bonded on PCB. (b) The response of the two Δ networks (Δ1 and Δ2) in use.

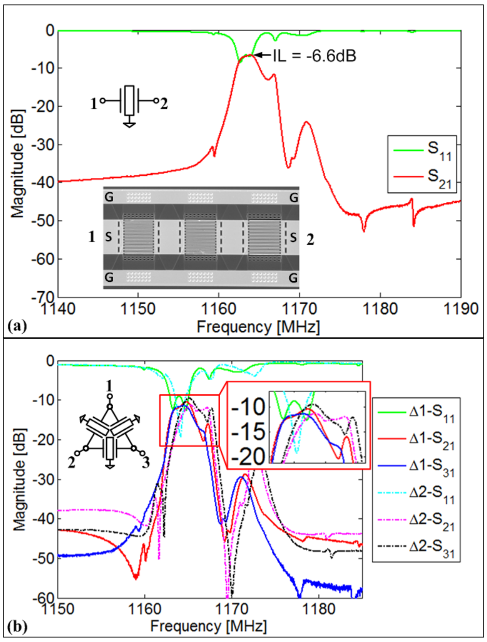

Figure 5.22: (a) The response of a third-order resonant filter wire bonded on PCB. (b) The response of the two Δ networks (Δ1 and Δ2) in use.

Since special attention is paid to the discrepancy between fabricated devices, especially the resonant frequency, a more precise fabrication process is used to make encapsulated AlN CMRs, as shown in Figure 5.23. The Institute of Microelectronics (IME), Singapore, has an excellent capability of depositing very uniform AlN (center) and Mo (bottom and top) layers. Moreover, the polysilicon barriers in the oxide layer offer a repeatable and CAD-defined etching volume for releasing devices. Finally, the encapsulation prevents the environment (for example, dust) from affecting the resonator operation. The standard deviations of resonant frequency and insertion loss for a 4-by-4 array of resonators with identical layout are 131.8 kHz and 0.023 dB, respectively, which meet our needs. Other detailed study on the uniformity of the same fabrication process can be found in [113].

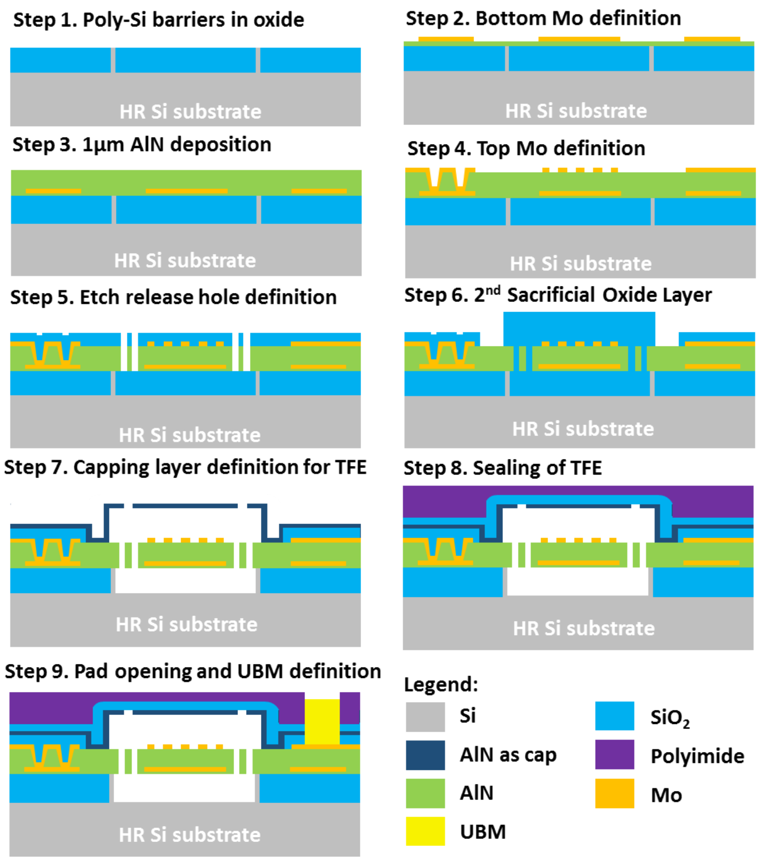

Figure 5.23: The developed fabrication process flow of AlN MEMS platform at A*STAR, IME, Singapore. Reprinted from [113].

As for the RF switches, ADI single-pole-double-throw (SPDT) RF switches are used to implement these 3 normal/complementary pairs of switches. They introduce additional ~1 dB loss. It is also observed that response of the switch in normal mode is asymmetric to the complementary mode, and that the off-paths are shunted to ground (y_{2_off} and y_{1_off} are comparable to y_{c1_on} and y_{c2_on}, respectively), as shown in Figure 5.24. To account for the shunt paths, the ADI SPDT switch is equivalent to four switches configured in Figure 5.26. Such deviation from the ideal switch model with negligible shunt paths potentially affects the circulator performance. Its behavior cannot be accurately predicted by the proposed model for double-branch circulator, which only accounts for six switches in total. However, it is possible to extend the model to account for twelve switches or even more, which will be briefly discussed in Section 6.2.

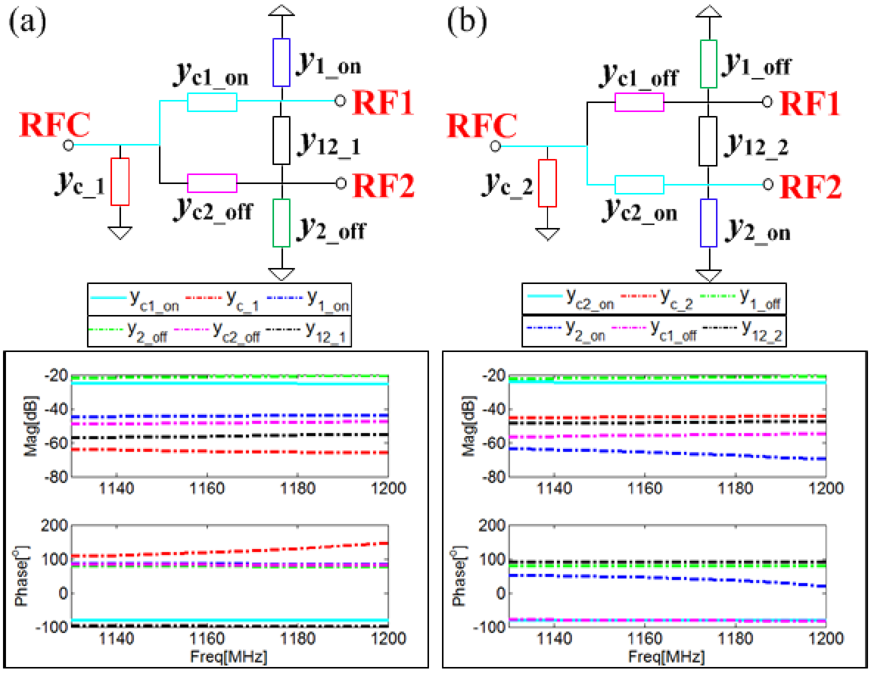

Figure 5.24: Electrical models of the ADI SPDT switch when (a) RFC-RF1 or (b) RFC-RF2 is on.

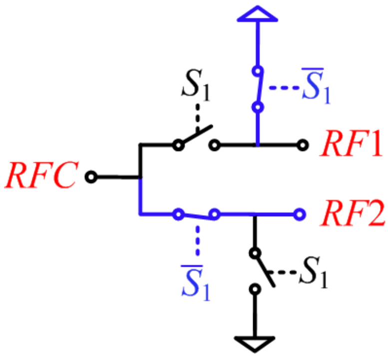

Figure 5.25: Simplified model of the ADI SPDT switch.

We implemented the circulators with discrete AlN MEMS filters and CMOS RF switches, which were separately wirebonded onto two PCBs (see Figure 5.26b and d). These PCBs were then connected through SMA cables/adaptors (see Figure 5.26a). As for the modulation signals, three pulse trains are generated by two synchronized 2-output pulse generators, Agilent 81110A. These pulse trains are then fed to a hex inverter, 74HCT04, to generate 3 complementary pairs of square waves (see Figure 5.26c). The phase differences between these signals were monitored by a 4-channel oscilloscope, Agilent DSO6014, and are automatically adjusted to be 120° by a

MATLAB program. The S-parameters are measured using an Agilent 4-port network analyzer, N5230A, after performing SOLT calibration.

The modulation frequency and duty cycle were swept to investigate their effect on insertion loss (*IL*) and isolation of the circulator, as shown in Figure 5.27a and Figure 5.28a. It can be observed that there are different patterns of trade-off between modulation frequency and duty cycle for two filter topologies. At this point in time, the reason behind the trade-off is not fully understood. Nonetheless, this experimental characterization facilitates the selection of the optimal modulation frequency and duty cycle so as to simultaneously attain the lowest *IL* and largest isolation. The S-parameters of the circulator using the modulation parameters at Point A and B are shown in Figure 5.27b and Figure 5.28b, respectively. Interestingly, more than 15 dB of isolation can be attained over the entire bandwidth of the filter (2.2 MHz and 3.3 MHz, respectively), in contrast to the narrow-band rejection demonstrated in [107] and [108]. As expected, the third-order filter based circulator achieves better out-of-band rejection (~60 dB). The *IL* of the demonstrated circulators are 12 dB and 14.5 dB, respectively. We have analyzed the main sources of loss in this configuration and listed them in Table 1. The mechanisms that account for ~6 dB loss still remain unclear. The plausible causes are asymmetries in the filters, the modulation process itself, delays in the inverter controlling the switching process, and glitches in the inverter outputs (observed especially beyond 1 MHz). Among the loss factors, PCB loss and the deviations in the implementation from rotational symmetry are expected to be significantly reduced by monolithic integration of the switches with the AlN devices.

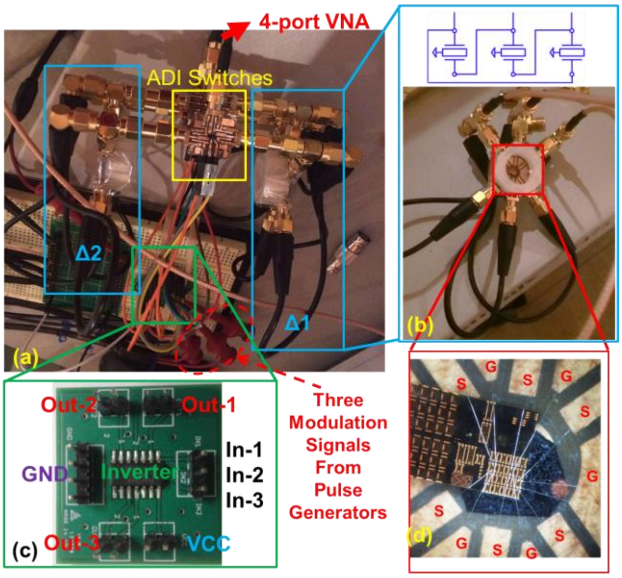

Figure 5.26: (a) The experimental setup of the proposed circulator in Figure 5.20a. (b) The connection method of the Δ-networks. (c) PCB design for the hex inverter. Each Out-*k* (*k* = 1-3) is a pair of pins, carrying two signals, one of which is the same as In-*k* (*k* = 1-3), the other is its complementary. (d) The optical image of wire-bonded resonators on PCB. The chip is formed by a 4-by-4 array of identical resonators. Three of these 16 resonators are chosen for this experiment.

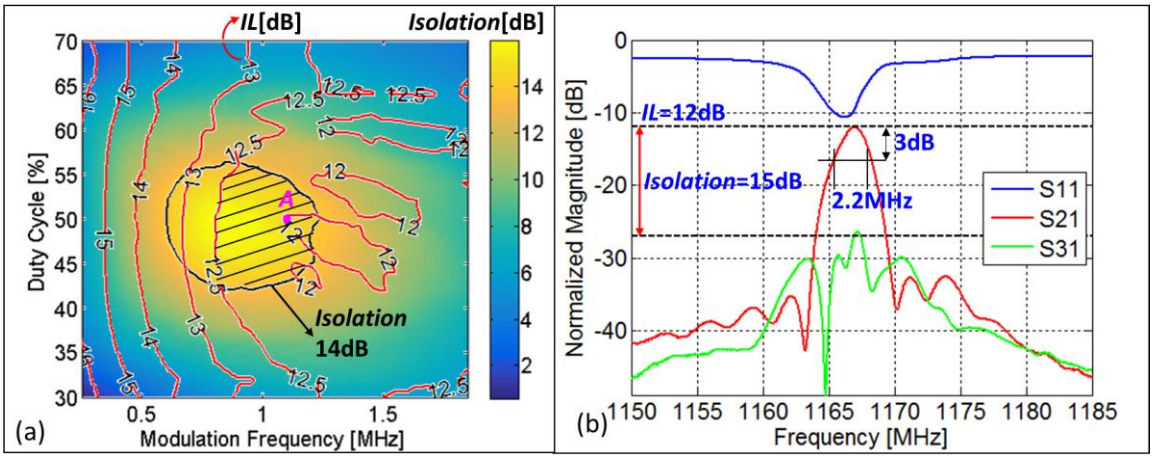

Figure 5.27: (a) The contour plot of IL (red lines) and isolation (background color) with respect to the modulation frequency and duty cycle for a first-order filter based circulator. (b) The response of the circulator when modulated at 1.1MHz with 50% duty cycle (Point A in Figure 5.27a)

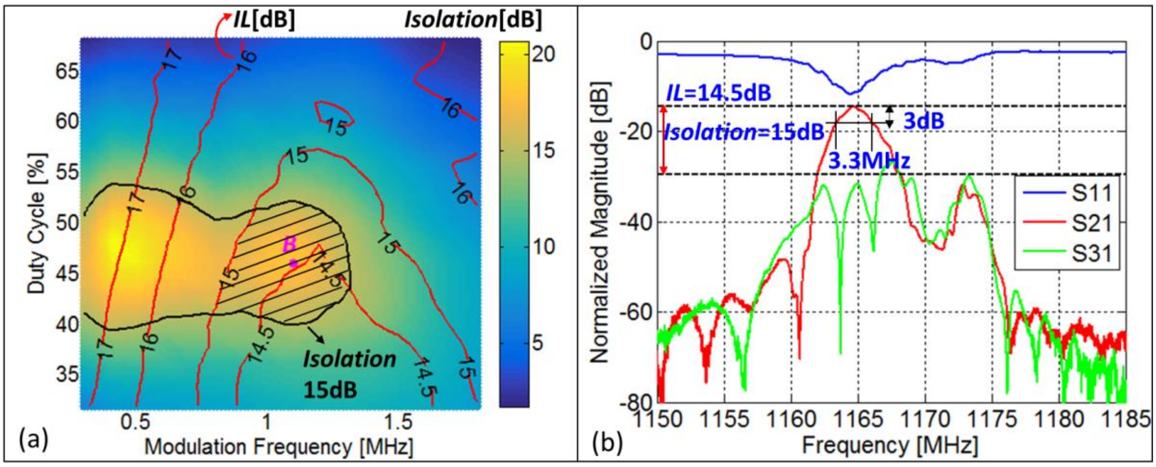

Figure 5.28: **(a) The contour plot of *IL* (red lines) and isolation (background color) with respect to the modulation frequency and duty cycle for third-order filter based circulator. (b) The response of the circulator when modulated at 1.1MHz with 46% duty cycle (Point B in Figure 5.28a).**

Table 5.3: Estimated contributions to the *IL* of the circulators. Units are in dB..

Factor	First-order	Third-order
Filter Loss + PCB Loss①	~3.7	~6.6
Switch Loss	~1.1	~1.1
Mismatch②	~0.9	~0.4
Leakage to Tx③	~0.3	~0.3
Unknown Loss④	~6.0	~6.1
Total	**12**	**14.5**

①PCB Loss is measured to be around 1 dB in this work.
②calculated as $20\cdot\log_{10}(1-|S_{11}|^2)$. In this work, S_{11} = 0.32 (–10 dB) and 0.22 (–13 dB), respectively.
③calculated as $20\cdot\log_{10}(1-|Iso|^2)$, where *Iso* means the isolation between Rx and Tx (the ratio of S_{31} to S_{21}). In this work, *Iso* = 0.18 (–15 dB).
④calculated by subtracting the first four types of loss from the total loss.

It's worth noting that the switches are used as passive devices, so they exhibit high linearity. Furthermore, AlN CMRs can be laid out in an array to improve the power handling capability [114]. Therefore, the proposed prototype is a very compact solution for the implementation of magnetic-free circulators, which also intrinsically offer low noise and high linearity.

CHAPTER 6: CONCLUSIONS AND FUTURE WORK

This thesis has mainly investigated three modulation methods to synthesize high-performance RF components.

To build frequency-stable oscillators, we utilize thermal modulation to "demodulate" the effect of ambient temperature fluctuations on the resonator frequency. By decoupling RF paths from supporting beams, the trade-off between power and Q is mitigated by ~10 times which results in simultaneously low power (as low as 353 μW over 120 °C) and high Q (as high as 4450 for 220 MHz device) [115]. The modulation strength (the amount of thermal power) is controlled by either analog or digital feedback circuits/systems. The analog method reduces the total power consumption (circuit + ovenization) to 3.8 mW and achieves a frequency stability of 100 ppm over 120 ℃ [78]. The digital method introduces the ANN algorithm for the first time in order to accelerate the calibration process of look-up tables and attain a better frequency stability of 14 ppm over 120 ℃ [116].

To construct low-noise oscillators based on AlN CMR, we employ force modulation to boost its Q and thus reduce the phase noise of an oscillator built with the same type of resonators. For a two-port CMR, by applying a second voltage source to drive the second port, the admittance Q ("sensed" by the first voltage source) of the first port can be theoretically boosted to infinity if specific conditions on the magnitude and phase of the modulating signal are met. With this method, we have demonstrated the ability to boost Q by at least 140 times (from 1,100 to 150,000) and reduce phase noise by at least 10 dBc/Hz.

To develop magnetic-free compact circulators, we take advantage of external electronic modulation to break the intrinsic reciprocity of LTI networks. A generalized magnetic-free topology is proposed and an accurate method to model the circulator electrical performance is developed by replacing switches with on-resistors plus parallel CCCSs and solving the circuits by linear superposition. A special embodiment of the proposed circulator based on AlN MEMS filters and CMOS RF switches has been demonstrated to provide 15 dB isolation, thus delivering a compact solution to in-band full duplexers [117].

The research work presented in this thesis sets a pathway for the development of fully integrated RF front-ends with multi-bands and spectral efficiency. However, before fulfilling this vision, a more comprehensive study of these modulation methods is necessary. Suggested avenues of future investigation efforts are: 1) identification of the physical limit in the minimization of the total power consumption of oven-controlled oscillators based on AlN CMRs, and 2) the synthesis of a more generalized circulator model that is able to accommodate any LTI networks and any number of modulation elements, being either switches or varactors. In the following, the validity and feasibility of these two topics will be proven in details and the guidelines of the rest work will be briefly provided.

6.1. Limit in Minimizing the Power Consumption of Oven-Controlled Oscillators

The total power consumption, P_{TOT}, of an oven-controlled oscillator is composed of the electrical power used to sustain oscillations, P_{ELEC}, and the thermal power, P_{TH}, used to ovenize the device:

$$P_{TOT} = P_{TH} + P_{ELEC} \tag{6.1}$$

There is a fundamental trade-off between P_{ELEC} and P_{TH}, thus dictating minimum power consumption.

The thermal power is examined first. In Section 3.1, the trade-off between oven power and loaded quality factor was derived. However, only power consumption via thermal conduction is taken into account. In fact, for high vaccum encapsulated ovenized resonators, thermal conduction might be negligible, but the power consumption via thermal radiation could play a significant role for sub-millwatt levels. Therefore, the total thermal power consumption, P_{TH}, can be decomposed as

$$P_{TH} = P_{cond} + P_{rad} \tag{6.2}$$

where P_{cond} and P_{rad} represent the power escaping through thermal conduction and thermal radiation. From Eq. (3.5), there exists an inequality

$$P_{cond} \cdot R_S > 4L_o T_a \Delta T \tag{6.3}$$

where R_S is the resistance in series, L_o *Lorentz number*, T_a absolute temperature, and ΔT the maximum temperature change of the resonator with respect to ambient temperature. The power consumption due to thermal radiation is given by

$$P_{rad} = \gamma \sigma A T_m^2 \tag{6.4}$$

where γ is the emissivity, σ the Stefan-Boltzmann constant, A the surface area of resonator, and T_m resonator operation temperature. The surface area can be estimated as

$$A \approx 2nPL + 2T\left(nP + L\right) > 2nPL \tag{6.5}$$

where n, P, L, and T are resonator parameters as shown in Figure 2.1.

Now, let's take a look at the electrical power. If a three-point oscillator as the one in Figure 2.7 is employed, the oscillation condition can be expressed as [8]

$$R_S + R_M \le \frac{g_m}{C_1 C_2 \omega_c^2} \tag{6.6}$$

where g_m is the transconductance for transistor M_1, which is given by

$$g_m = \frac{2I_D}{\Delta V_{GS}} \tag{6.7}$$

where I_D is the current through the transistor M_1 and ΔV_{GS} is the overdrive voltage, *i.e.* the amount of voltage across gate and source (V_{GS}) exceeding the threshold voltage (V_T), $V_{GS} - V_T$. The electrical power is given by

$$P_{ELEC} = V_{DD} \cdot I_D > V_{GS} \cdot I_D \tag{6.8}$$

From Eq. (2.17), we have

$$R_M = \frac{\pi^2}{8} \frac{1}{\omega_s C_0} \frac{1}{k_t^2 Q_{un}} \tag{6.9}$$

The parallel capacitance, C_0, can be estimated as

$$C_0 = \varepsilon_{33}\varepsilon_0 \frac{nWL}{T} = \varepsilon_{33}\varepsilon_0 \kappa \frac{nPL}{T} \tag{6.10}$$

where κ is the metal coverage, typically between 0.5 and 1.

To reduce the electrical power, R_M and R_S are desired to be small. On one hand, for a given resonator frequency, since $k_t^2 \cdot Q_{\mathrm{un}}$ is fixed for AlN CMR, R_M can be decreased by increasing C_0. However, it increases the surface area thus increasing radiation power. On the other hand, decreasing R_S increases the conduction power by Eq. (6.3). Therefore, there is trade-off between electrical power and thermal power, which means that the total power consumption of oven-controlled oscillators has a minimum value.

The rest of the work would be focused on i) the derivation or estimation of the minimum total power consumption of oven controlled oscillators, and ii) the visualization of the trade-off between electrical and thermal power, which could be obtained by the above analytical model or SPICE simulation.

6.2. Generalized Model for Circulators Based on Parametric Modulation

The problem of the two circulator models developed in Chapter 5 are that they are not flexible enough to accommodate any number of modulation elements, not only switches but also varactors. The reason is the derivation depends on the specific modulation scheme. To address this issue, we examine a generalized non-reciprocal circuit with switches and varactors, as shown in Figure 6.1.

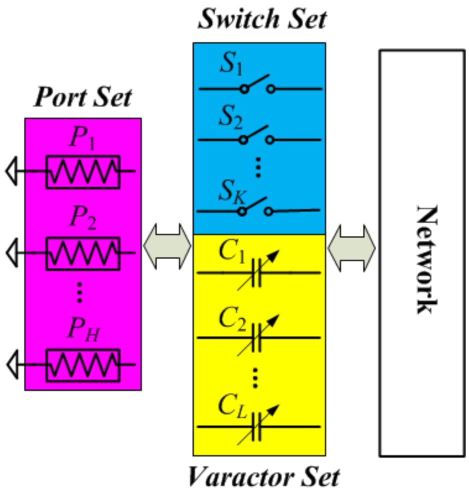

Figure 6.1: A generalized non-reciprocal circuit with *H* ports, *K* switches, and *L* varactors. The modulation frequency is the same for all switches and varactors. The modulation signal is square wave for switches and sinusoidal wave for varactors for the analysis. If the modulation signal is also a square wave for a varactor, it can be treated as a switch in parallel with a static capacitor.

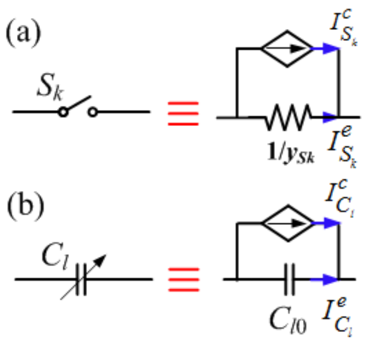

Figure 6.2: Comparison of equivalent models between (a) *k*-th Switch and *l*-th Varactor. $I^c_{S_k}, I^c_{C_l}$ are the CCCSs' current phasors. $I^e_{S_k}, I^e_{C_l}$ are the current phasors through the equivalent resistor and the static capacitor, respectively.

The idea of solving this circuit is the same as the method presented in Chapter 5. The switches and varactors are replaced with corresponding models and then solving the equivalent circuit with linear superposition. The equivalent model of a switch is already presented in Figure 5.5c, which is re-printed in Figure 6.2a. The relationship between $I_{S_k}^c$ and $I_{S_k}^e$ is rewritten as

$$I_{S_k}^c = \mathbf{Y}_{S_k} \mathbf{C}_{S_k}(\alpha_k, \theta_k)\left(\mathbf{Y}_{S_k}\right)^{-1} I_{S_k}^e \tag{6.11}$$

where $\mathbf{Y}_{S_k}$ and $\mathbf{C}_{S_k}(\alpha_k, \theta_k)$ are essentially the same as $\mathbf{Y}_S$ and $\mathbf{C}(\alpha, \theta)$ defined in Section 5.2.1, but with new subscript to be clearly associated with *k*-th Switch. In the following section, $\mathbf{C}_{S_k}(\alpha_k, \theta_k)$ is denoted as $\mathbf{C}_{S_k}$ for convenience. As for the varactor model, its capacitance varying in time can be expressed as

$$C_l = C_{l0}\left[1 + \delta_l \cos\left(\omega_0 t - \theta_l\right)\right] = C_{l0}\left[1 + \delta_l \frac{e^{j(\omega_0 t - \theta_l)} + e^{-j(\omega_0 t - \theta_l)}}{2}\right] \tag{6.12}$$

where C_l is the real-time capacitance of *l*-th varactor, C_{l0} the static capacitance, δ_l the modulation amplitude, and ω_0 the modulation frequency. With an applied voltage of $u_{C_l}(t) = U_{C_l} e^{j\omega_{RF} t}$ at the carrier frequency, ω_{RF}, across the switch, the corresponding excited current, I_l, in time domain is

$$\begin{aligned} I_l(t) &= \frac{d}{dt}\left(C_l u_{C_l}\right) = C_l \frac{d}{dt}\left(u_{C_l}\right) + u_{C_l} \frac{d}{dt}\left(C_l\right) \\ &= \left[j\frac{\delta_l}{2}\left(\omega_{RF} - \omega_0\right) e^{j(\omega_{RF} - \omega_0 + \theta_l)t} + j\omega_{RF} e^{j\omega_{RF} t} + j\frac{\delta_l}{2}\left(\omega_{RF} + \omega_0\right) e^{j(\omega_{RF} + \omega_0 - \theta_l)t} \right] C_{l0} U_{C_l} \\ &= \sum_{n=-\infty}^{+\infty} i_{C_l,n} e^{j(\omega_{RF} + n\omega_0)t} \end{aligned} \tag{6.13}$$

where $i_{C_l,0} = j\omega_{RF} C_{l0} U_{C_l}, i_{C_l,-1} = \frac{\delta_l}{2}\frac{\omega_{RF} - \omega_0}{\omega_{RF}} e^{j\theta_l} i_{C_l,0}, i_{C_l,+1} = \frac{\delta_l}{2}\frac{\omega_{RF} + \omega_0}{\omega_{RF}} e^{-j\theta_l} i_{C_l,0}, i_{C_l,n} = 0\left(n \neq 0, \pm 1\right)$. This is similar to Eq. (5.3). Therefore, we can develop a similar model as shown in Figure 6.2b to the switch model as shown in Figure 6.2a (except that the equivalent resistor is replaced by the static capacitor). The relationship between $I_{C_l}^{c}$ and $I_{C_l}^{e}$ can be written as

$$I_{C_l}^{c} = \mathbf{Y}_{C_l}\mathbf{C}_{C_l}\left(\delta_l,\theta_l\right)\left(\mathbf{Y}_{C_l}\right)^{-1} I_{C_l}^{e} \tag{6.14}$$

where $\mathbf{Y}_{C_l} = jC_{l0}\cdot diag\left[\left(\omega_{RF}-N\omega_0\right)\ \ldots\ \left(\omega_{RF}-\omega_0\right)\ \left(\omega_{RF}\right)\ \left(\omega_{RF}+\omega_0\right)\ \ldots\ \left(\omega_{RF}+N\omega_0\right)\right]$,

$$\mathbf{C}_{C_l}\left(\delta_l,\theta_l\right)=\begin{bmatrix} 1 & \frac{\delta_l}{2}e^{j\theta} & \cdots & 0 & \cdots & 0 \\ \frac{\delta_l}{2}e^{-j\theta} & 1 & \cdots & 0 & \cdots & 0 \\ \vdots & \vdots & \ddots & \vdots & \cdots & \vdots \\ 0 & 0 & \cdots & C_{ij}\left(\delta_l,\theta_l\right) & \cdots & 0 \\ \vdots & \vdots & \cdots & \vdots & \ddots & \vdots \\ 0 & 0 & \cdots & 0 & \cdots & 1 \end{bmatrix}, \text{where } C_{ij}\left(\delta_l,\theta_l\right)=\begin{cases} 1, & i=j \\ \frac{\delta_l}{2}e^{(j-i)\theta_l}, & |j-i|=1. \\ 0, & else \end{cases}$$

Obviously, $\mathbf{C}_{C_l}\left(\delta_l,\theta_l\right)$ is also asymmetric but has much fewer non-zero terms than $\mathbf{C}_{S_k}\left(\alpha_k,\theta_k\right)$. In the following section, $\mathbf{C}_{C_l}\left(\delta_l,\theta_l\right)$ is denoted as $\mathbf{C}_{C_l}$ for convenience.

Similarly, we define linear *p*-, *q*-, and *r*-functions for the circuit as shown in Figure 6.3. *p*-functions are defined as

$$P_{Xz} = \frac{i_{Xz}}{u_1} \tag{6.15}$$

where u_1 is a voltage source in series with Port 1, and i_{Xz} is the current of *z*-th *X* component, *X* can be *P* (port), *S* (switch), or *C* (varactor), *z* is *h*, *k*, or *l*, correspondingly. *q*-functions are defined as

$$Q_{X_jY_i} = \frac{i_{X_j}}{i_{Y_i}} \tag{6.16}$$

where X_j and Y_i represent either any *k*-th switch equivalent resistor (denoted as 'S_k') or *l*-th static capacitor (denote as 'C_l'), i_{Yi} is the current source in parallel with Y_i component, i_{Xj} is the current injected to X_j component. *r*-functions are defined as

$$R_{P_hY_i} = \frac{i_{P_h}}{i_{Y_i}}. \tag{6.17}$$

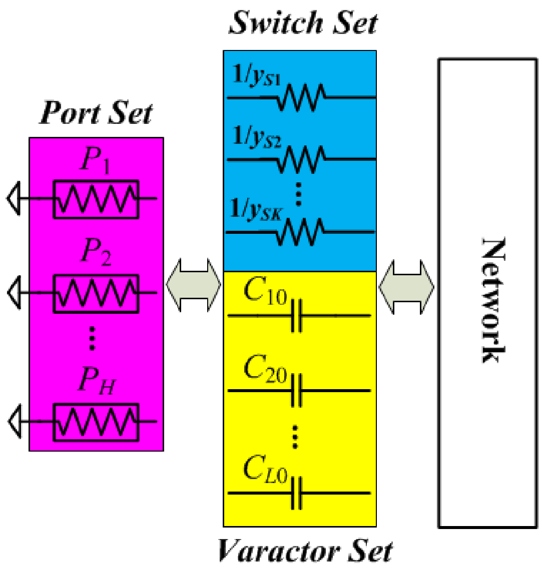

Figure 6.3: The equivalent circuit of the non-reciprocal circuit in Figure 6.1without modulation.

Table 6.1: Naming Convention of Currents in the Generalized Non-reciprocal Circuits.

Notation	Meaning
I_P	Steady currents of all ports with modulation, defined as $\left[(I_{P1})^T \quad (I_{P2})^T \quad \cdots \quad (I_{PH})^T\right]^T$.
I_X^e	Steady currents of X static elements with modulation, defined as $\left[(I_{X1}^e)^T \quad (I_{X2}^e)^T \quad \cdots \quad (I_{XZ}^e)^T\right]^T$. X can be S or C. Z = K, or L.
I_X^c	Steady currents of CCCCs in parallel with X elements with modulation, defined as $\left[(I_{X1}^c)^T \quad (I_{X2}^c)^T \quad \cdots \quad (I_{XZ}^c)^T\right]^T$. X can be S or C. Z = K, or L.
$I_{P,0}$	Steady currents of all ports without modulation, defined as $\left[(I_{P1,0})^T \quad (I_{P2,0})^T \quad \cdots \quad (I_{PH,0})^T\right]^T$.
$I_{X,0}$	Steady currents of X static elements without modulation, defined as $\left[(I_{X1,0})^T \quad (I_{X2,0})^T \quad \cdots \quad (I_{XZ,0})^T\right]^T$. X can be S or C. Z = K, or L.

By using the naming convention defined in, we have the model readily available

$$\begin{bmatrix} I_S^c \\ I_C^c \end{bmatrix} = \begin{pmatrix} \tilde{\mathbf{Y}}_S & \mathbf{0} \\ \mathbf{0} & \tilde{\mathbf{Y}}_C \end{pmatrix} \begin{pmatrix} \tilde{\mathbf{C}}_S & \mathbf{0} \\ \mathbf{0} & \tilde{\mathbf{C}}_C \end{pmatrix} \begin{pmatrix} \tilde{\mathbf{Y}}_S & \mathbf{0} \\ \mathbf{0} & \tilde{\mathbf{Y}}_C \end{pmatrix}^{-1} \begin{bmatrix} I_S^e \\ I_C^e \end{bmatrix} \tag{6.18}$$

$$\begin{bmatrix} I_S^e \\ I_C^e \end{bmatrix} = \begin{bmatrix} I_{S,0} \\ I_{C,0} \end{bmatrix} + \begin{pmatrix} \tilde{\mathbf{F}}_{Q_S} & \tilde{\mathbf{F}}_{Q_{SC}} \\ \tilde{\mathbf{F}}_{Q_{CS}} & \tilde{\mathbf{F}}_{Q_C} \end{pmatrix} \begin{bmatrix} I_S^c \\ I_C^c \end{bmatrix} \tag{6.19}$$

$$I_P = I_{P,0} + \begin{pmatrix} \tilde{\mathbf{F}}_{R_{PS}} & \mathbf{0} \\ \mathbf{0} & \tilde{\mathbf{F}}_{R_{PC}} \end{pmatrix} \begin{bmatrix} I_S^c \\ I_C^c \end{bmatrix} \tag{6.20}$$

where $\tilde{\mathbf{Y}}_S = diag\left(\mathbf{Y}_{S_1} \ \mathbf{Y}_{S_2} \ \cdots \ \mathbf{Y}_{S_K}\right)$, $\tilde{\mathbf{Y}}_C = diag\left(\mathbf{Y}_{C_1} \ \mathbf{Y}_{C_2} \ \cdots \ \mathbf{Y}_{C_K}\right)$,

$\tilde{\mathbf{C}}_S = diag\left(\mathbf{C}_{S_1} \ \mathbf{C}_{S_2} \ \cdots \ \mathbf{C}_{S_K}\right)$, $\tilde{\mathbf{C}}_C = diag\left(\mathbf{C}_{C_1} \ \mathbf{C}_{C_2} \ \cdots \ \mathbf{C}_{C_L}\right)$,

$$\tilde{\mathbf{F}}_{Q_S}=\begin{pmatrix}\mathbf{F}_{Q_{S_1S_1}} & \mathbf{F}_{Q_{S_1S_2}} & \cdots & \mathbf{F}_{Q_{S_1S_K}}\\ \mathbf{F}_{Q_{S_2S_1}} & \mathbf{F}_{Q_{S_2S_2}} & \cdots & \mathbf{F}_{Q_{S_2S_K}}\\ \vdots & \vdots & \ddots & \vdots\\ \mathbf{F}_{Q_{S_KS_1}} & \mathbf{F}_{Q_{S_KS_2}} & \cdots & \mathbf{F}_{Q_{S_KS_K}}\end{pmatrix}_{K\times K},\ \tilde{\mathbf{F}}_{Q_C}=\begin{pmatrix}\mathbf{F}_{Q_{C_1C_1}} & \mathbf{F}_{Q_{C_1C_2}} & \cdots & \mathbf{F}_{Q_{C_1C_L}}\\ \mathbf{F}_{Q_{C_2C_1}} & \mathbf{F}_{Q_{C_2C_2}} & \cdots & \mathbf{F}_{Q_{C_2C_L}}\\ \vdots & \vdots & \ddots & \vdots\\ \mathbf{F}_{Q_{C_LC_1}} & \mathbf{F}_{Q_{C_LC_2}} & \cdots & \mathbf{F}_{Q_{C_LC_L}}\end{pmatrix}_{L\times L},$$

$$\tilde{\mathbf{F}}_{Q_{SC}}=\begin{pmatrix}\mathbf{F}_{Q_{S_1C_1}} & \mathbf{F}_{Q_{S_1C_2}} & \cdots & \mathbf{F}_{Q_{S_1C_L}}\\ \mathbf{F}_{Q_{S_2C_1}} & \mathbf{F}_{Q_{S_2C_2}} & \cdots & \mathbf{F}_{Q_{S_2C_L}}\\ \vdots & \vdots & \ddots & \vdots\\ \mathbf{F}_{Q_{S_KC_1}} & \mathbf{F}_{Q_{S_KC_2}} & \cdots & \mathbf{F}_{Q_{S_KC_L}}\end{pmatrix}_{K\times L},\ \tilde{\mathbf{F}}_{Q_{CS}}=\begin{pmatrix}\mathbf{F}_{Q_{C_1S_1}} & \mathbf{F}_{Q_{C_1S_2}} & \cdots & \mathbf{F}_{Q_{C_1S_K}}\\ \mathbf{F}_{Q_{C_2S_1}} & \mathbf{F}_{Q_{C_2S_2}} & \cdots & \mathbf{F}_{Q_{C_2S_K}}\\ \vdots & \vdots & \ddots & \vdots\\ \mathbf{F}_{Q_{C_LS_1}} & \mathbf{F}_{Q_{C_LS_2}} & \cdots & \mathbf{F}_{Q_{C_LS_K}}\end{pmatrix}_{L\times K},$$

$$\tilde{\mathbf{F}}_{R_{PS}}=\begin{pmatrix}\mathbf{F}_{R_{P_1S_1}} & \mathbf{F}_{R_{P_1S_2}} & \cdots & \mathbf{F}_{R_{P_1S_K}}\\ \mathbf{F}_{R_{P_2S_1}} & \mathbf{F}_{R_{P_2S_2}} & \cdots & \mathbf{F}_{R_{P_2S_K}}\\ \vdots & \vdots & \ddots & \vdots\\ \mathbf{F}_{R_{P_HS_1}} & \mathbf{F}_{R_{P_HS_2}} & \cdots & \mathbf{F}_{R_{P_HS_K}}\end{pmatrix}_{H\times K},\ \text{and}\ \tilde{\mathbf{F}}_{R_{PC}}=\begin{pmatrix}\mathbf{F}_{R_{P_1C_1}} & \mathbf{F}_{R_{P_1C_2}} & \cdots & \mathbf{F}_{R_{P_1C_L}}\\ \mathbf{F}_{R_{P_2C_1}} & \mathbf{F}_{R_{P_2C_2}} & \cdots & \mathbf{F}_{R_{P_2C_L}}\\ \vdots & \vdots & \ddots & \vdots\\ \mathbf{F}_{R_{P_HC_1}} & \mathbf{F}_{R_{P_HC_2}} & \cdots & \mathbf{F}_{R_{C_LC_L}}\end{pmatrix}_{H\times L}.$$

$I_{P,0}$ and $I_{S,0}$ are the circuit response without modulation. When assuming a voltage source U_1 exciting the circuit at Port 1, the non-zero elements in $I_{Ph,0}$, $I_{Sk,0}$, and $I_{Cl,0}$ are:

$$\begin{aligned}\left[i_{P_h,0}\right]_0&=P_{P_h}U_1\\ \left[i_{S_k,0}\right]_0&=P_{S_k}U_1\\ \left[i_{C_l,0}\right]_0&=P_{C_l}U_1\end{aligned}\tag{6.21}$$

Combining Eq. (6.18) and (6.19), $\left[\left(I_S^e\right)^T \quad \left(I_C^e\right)^T\right]^T$ can be readily calculated by

$$\begin{bmatrix}I_S^e\\ I_C^e\end{bmatrix}=\left[\tilde{\mathbf{I}}_d-\begin{pmatrix}\tilde{\mathbf{F}}_{Q_S} & \tilde{\mathbf{F}}_{Q_{SC}}\\ \tilde{\mathbf{F}}_{Q_{CS}} & \tilde{\mathbf{F}}_{Q_C}\end{pmatrix}\begin{pmatrix}\tilde{\mathbf{Y}}_S & \mathbf{0}\\ \mathbf{0} & \tilde{\mathbf{Y}}_C\end{pmatrix}\begin{pmatrix}\tilde{\mathbf{C}}_S & \mathbf{0}\\ \mathbf{0} & \tilde{\mathbf{C}}_C\end{pmatrix}\begin{pmatrix}\tilde{\mathbf{Y}}_S & \mathbf{0}\\ \mathbf{0} & \tilde{\mathbf{Y}}_C\end{pmatrix}^{-1}\right]^{-1}\begin{bmatrix}I_{S,0}\\ I_{C,0}\end{bmatrix}\tag{6.22}$$

where $\tilde{\mathbf{I}}_d$ is a $(K + L)\times(2N + 1)$ order identity matrix. Then the S-parameters for this circuit can be easily obtained by definition. It is worth restating that this model allows the analysis of any circulator topologies based on the parametric modulation (as long as the modulation frequency is the same for all modulating elements).

The rest of the work can be divided into: i) the development of a program that implements the above generalized circulator model, ii) the experimental verification of the above model, and iii) the derivation and generalization of guidelines to design a high-performance circulator, which comes down to the circulator topology, modulation parameters, and filter performance.

APPENDIX A: CIRCULATOR MODELING MATLAB CODE

This appendix contains the MATLAB codes that are used to predict the S-parameters of single-branch and double-branch circulators. Before running the codes, *p*- and *q*-functions over a large enough frequency range, [f_L, f_H], need to be calculated or simulated by SPICE tool, for example, Agilent ADS, as well as the on-admittance of RF switches; and they are saved in two structures: `Net` and `Switch`. As mentioned before, *r*-functions can be derived from *q*-functions via Kirchhoff's Current Law (KCL), hence are not explicitly declared in the codes. Assuming the frequency of interest is [f_1, f_2], the maximum modulation frequency, f_0, and the maximum mixing order, N, then the simulation frequency range must satisfies to avoid singular matrix issue: $f_L \le f_1 - N{\cdot}f_0$, $f_H \ge f_2 + N{\cdot}f_0$. Two algorithms start with loading the structures, followed by the calculation of matrix $\tilde{\mathbf{C}}_s, \tilde{\mathbf{Y}}_s, \tilde{\mathbf{F}}_{Qs}$, and $\tilde{\mathbf{F}}_{Rs}$ (for single-branch circulator) or $\tilde{\mathbf{C}}_d, \tilde{\mathbf{Y}}_d, \tilde{\mathbf{F}}_{Qd}$, and $\tilde{\mathbf{F}}_{Rd}$ (for double-branch circulator). The corresponding circuit steady states, I_S and I_P, are computed by Eq. (5.25), (5.21), (5.23), or (5.36), (5.32), (5.34), and repetition for every frequency of interest. Finally, S-parameters can be obtained via Eq. (5.26). Due to the assumption of 3-fold rotational symmetry, only S_{11}, S_{21}, and S_{31} need to be calculated.

A.1. MATLAB Code for Single-Branch Circulator

```
clear all;
close all;
clc;

%load p- and q-functions, series admittance ys
load('Switch_Net_single.mat');

f_sweep = (linspace(10, 35, 401))'; %sweep frequency in MHz
fm = 0.54; % modulation frequency in MHz
alpha = 0.45; %duty cycle
M_order = 16; %maximum mixing order
```

```
Z0 = 50; %characteristic impedance
theta = (0:2)*2/3*pi; %phase delays in modulation signals
f = @(n,th) exp(-1j*n*th).*(1-exp(-1j*2*alpha*n*pi))./(1j*2*n*pi);
freq_num = 2*M_order + 1; %the number of mixing frequency of interest
index_shift = M_order + 1; %index of carrier frequency

%construction of matrix Cs
C1_matrix = zeros(freq_num);
C2_matrix = zeros(freq_num);
C3_matrix = zeros(freq_num);
for p = 1:size(C1_matrix,2)
    C1_matrix(:,p) = f((0:2*M_order)'-(p-1), theta(1));
    C2_matrix(:,p) = f((0:2*M_order)'-(p-1), theta(2));
    C3_matrix(:,p) = f((0:2*M_order)'-(p-1), theta(3));
end
C1_matrix(eye(freq_num)~=0) = -(1-alpha); %replace the diagonal NAN
C2_matrix(eye(freq_num)~=0) = -(1-alpha); %note the minus sign
C3_matrix(eye(freq_num)~=0) = -(1-alpha);
C_MATRIX = [C1_matrix, zeros(size(C1_matrix)), zeros(size(C1_matrix));
            zeros(size(C2_matrix)), C2_matrix, zeros(size(C2_matrix));
            zeros(size(C3_matrix)), zeros(size(C3_matrix)), C3_matrix];

%interpolation of p- and q-functions, series admittance ys
PI_matrix = zeros(freq_num, length(f_sweep));
PIJ_matrix = zeros(freq_num, length(f_sweep));
QI_matrix = zeros(freq_num, length(f_sweep));
QIJ_matrix = zeros(freq_num, length(f_sweep));
ys_matrix = zeros(freq_num, length(f_sweep));
for i = 1:freq_num
    PI_matrix(i,:) = interp1(Net.f_MHz, Net.PI, f_sweep + (i-
            index_shift)*fm);
    PIJ_matrix(i,:) = interp1(Net.f_MHz, Net.PIJ, f_sweep + (i-
            index_shift)*fm);
    QI_matrix(i,:) = interp1(Net.f_MHz, Net.QI, f_sweep + (i-
            index_shift)*fm);
    QIJ_matrix(i,:) = interp1(Net.f_MHz, Net.QIJ, f_sweep + (i-
            index_shift)*fm);
    ys_matrix(i,:) = interp1(Switch.f_MHz, Switch.ys, f_sweep + (i-
            index_shift)*fm);
end

%port current declaration
curr_port1 = zeros(freq_num, 2, length(f_sweep));
curr_port2 = zeros(freq_num, 2, length(f_sweep));
curr_port3 = zeros(freq_num, 2, length(f_sweep));
%switch current declaration
curr_switch1 = zeros(freq_num, 2, length(f_sweep));
curr_switch2 = zeros(freq_num, 2, length(f_sweep));
curr_switch3 = zeros(freq_num, 2, length(f_sweep));
%the first column: initial current with modulation
%the second column: final current with modulation
%assignment of the first column, Eq. (5.24)
curr_port1(index_shift,1,:) = interp1(Net.f_MHz, Net.PI, f_sweep);
curr_port2(index_shift,1,:) = interp1(Net.f_MHz, Net.PIJ, f_sweep);
curr_port3(index_shift,1,:) = curr_port2(index_shift,1,:);
curr_switch1(index_shift,1,:) = curr_port1(index_shift,1,:);
curr_switch2(index_shift,1,:) = curr_port2(index_shift,1,:);
curr_switch3(index_shift,1,:) = curr_port2(index_shift,1,:);

%calculation of the final current
for r = 1:length(f_sweep) %loop for different frequency
    QI_submatrix = diag(QI_matrix(:,r));
    QIJ_submatrix = diag(QIJ_matrix(:,r));
    Ys_submatrix = diag(ys_matrix(:,r));
    Fs_MATRIX = [QI_submatrix,  QIJ_submatrix, QIJ_submatrix;
                 QIJ_submatrix, QI_submatrix,  QIJ_submatrix;
                 QIJ_submatrix, QIJ_submatrix, QI_submatrix];
```

```
    Ys_MATRIX = [Ys_submatrix, zeros(size(Ys_submatrix)),
            zeros(size(Ys_submatrix));
                zeros(size(Ys_submatrix)), Ys_submatrix,
            zeros(size(Ys_submatrix));
                zeros(size(Ys_submatrix)), zeros(size(Ys_submatrix)),
            Ys_submatrix];
    YCY_MATRIX = (Ys_MATRIX*C_MATRIX)/Ys_MATRIX;
    %Eq. (5.25)
    A_matrix = eye(size(Fs_MATRIX)) - Fs_MATRIX*YCY_MATRIX;
    b_vector = [curr_switch1(:,1,r);
                curr_switch2(:,1,r);
                curr_switch3(:,1,r)];
    Xs_vector = A_matrix\b_vector;
    curr_switch1(:,2,r) = Xs_vector(1:freq_num);
    curr_switch2(:,2,r) = Xs_vector(freq_num+1:2*freq_num);
    curr_switch3(:,2,r) = Xs_vector(2*freq_num+1:3*freq_num);
    p_vector = [curr_port1(:,1,r);
                curr_port2(:,1,r);
                curr_port3(:,1,r)];
    Xp_vector = p_vector + (eye(size(Fs_MATRIX)) +
            Fs_MATRIX)*YCY_MATRIX*Xs_vector;
    curr_port1(:,2,r) = Xp_vector(1:freq_num);
    curr_port2(:,2,r) = Xp_vector(freq_num+1:2*freq_num);
    curr_port3(:,2,r) = Xp_vector(2*freq_num+1:3*freq_num);
end

Ip1 = reshape(curr_port1(index_shift,2,:),1,[]);
Ip2 = reshape(curr_port2(index_shift,2,:),1,[]);
Ip3 = reshape(curr_port3(index_shift,2,:),1,[]);

%calculation of S-parameters
S11 = 1-2*Ip1*Z0;
S21 = -2*Ip2*Z0;
S31 = -2*Ip3*Z0;
```

A.2. MATLAB Code for Double-Branch Circulator

```
clear all;
close all;
clc;

%load p- and q-functions, series admittance ys
load('Switch_Net_double.mat');

f_sweep = (linspace(14, 31, 401))'; %sweep frequency in MHz
fm = 0.8; %modulation frequency in MHz
alpha = 0.5; %duty cycle
M_order = 16; %maximum mixing order
Z0 = 50; %characteristic impedance
theta = (0:2)*2/3*pi; %phase delays in modulation signals
f = @(n,th) exp(-1j*n*th).*(1-exp(-1j*2*alpha*n*pi))./(1j*2*n*pi);
f_bar = @(n,th) exp(-1j*n*(2*alpha*pi+th)).*(1-exp(-1j*2*(1-
   alpha)*n*pi))./(1j*2*n*pi);
freq_num = 2*M_order + 1; %the number of mixing frequency of interest
index_shift = M_order + 1; %index of carrier frequency
freq_num = 2*M_order + 1; %the number of mixing frequency of interest
index_shift = M_order + 1; %index of carrier frequency

%construction of matrix Cs
C1_matrix = zeros(freq_num);
C2_matrix = zeros(freq_num);
C3_matrix = zeros(freq_num);
C1_matrix_bar = zeros(freq_num);
C2_matrix_bar = zeros(freq_num);
```

```
C3_matrix_bar = zeros(freq_num);
for p = 1:size(C1_matrix,2)
    C1_matrix(:,p) = f((0:2*M_order)'-(p-1), theta(1));
    C2_matrix(:,p) = f((0:2*M_order)'-(p-1), theta(2));
    C3_matrix(:,p) = f((0:2*M_order)'-(p-1), theta(3));
    C1_matrix_bar(:,p) = f_bar((0:2*M_order)'-(p-1), theta(1));
    C2_matrix_bar(:,p) = f_bar((0:2*M_order)'-(p-1), theta(2));
    C3_matrix_bar(:,p) = f_bar((0:2*M_order)'-(p-1), theta(3));
end
C1_matrix(eye(freq_num)~=0) = -(1-alpha); %replace the diagonal NAN
C2_matrix(eye(freq_num)~=0) = -(1-alpha); %note the minus sign
C3_matrix(eye(freq_num)~=0) = -(1-alpha);
C1_matrix_bar(eye(freq_num)~=0) = -alpha; %replace the diagonal NAN
C2_matrix_bar(eye(freq_num)~=0) = -alpha; %note the minus sign
C3_matrix_bar(eye(freq_num)~=0) = -alpha;
C_MATRIX = zeros(6*freq_num);
C_MATRIX(1:freq_num,1:freq_num) = C1_matrix;
C_MATRIX((1:freq_num)+freq_num,(1:freq_num)+freq_num) = C1_matrix_bar;
C_MATRIX((1:freq_num)+2*freq_num,(1:freq_num)+2*freq_num) = C2_matrix;
C_MATRIX((1:freq_num)+3*freq_num,(1:freq_num)+3*freq_num)=C2_matrix_bar;
C_MATRIX((1:freq_num)+4*freq_num,(1:freq_num)+4*freq_num) = C3_matrix;
C_MATRIX((1:freq_num)+5*freq_num,(1:freq_num)+5*freq_num)=C3_matrix_bar;

%interpolation of p- and q-functions, series admittance ys
PI_matrix = zeros(freq_num, length(f_sweep));
PIJ_matrix = zeros(freq_num, length(f_sweep));
QI1_matrix = zeros(freq_num, length(f_sweep));
QIJ1_matrix = zeros(freq_num, length(f_sweep));
QI2_matrix = zeros(freq_num, length(f_sweep));
QIJ2_matrix = zeros(freq_num, length(f_sweep));
ys_matrix = zeros(freq_num, length(f_sweep));
for i = 1:freq_num
    PI_matrix(i,:) = interp1(Net.f_MHz, Net.PI, f_sweep + (i-
            index_shift)*fm);
    PIJ_matrix(i,:) = interp1(Net.f_MHz, Net.PIJ, f_sweep + (i-
            index_shift)*fm);
    QI1_matrix(i,:) = interp1(Net.f_MHz, Net.QI1, f_sweep + (i-
            index_shift)*fm);
    QIJ1_matrix(i,:) = interp1(Net.f_MHz, Net.QIJ1, f_sweep + (i-
            index_shift)*fm);
    QI2_matrix(i,:) = interp1(Net.f_MHz, Net.QI2, f_sweep + (i-
            index_shift)*fm);
    QIJ2_matrix(i,:) = interp1(Net.f_MHz, Net.QIJ2, f_sweep + (i-
            index_shift)*fm);
    ys_matrix(i,:) = interp1(Switch.f_MHz, Switch.ys, f_sweep + (i-
            index_shift)*fm);
end

%port current declaration
curr_port1 = zeros(freq_num, 2, length(f_sweep));
curr_port2 = zeros(freq_num, 2, length(f_sweep));
curr_port3 = zeros(freq_num, 2, length(f_sweep));
%switch current declaration
curr_switch11 = zeros(freq_num, 2, length(f_sweep));
curr_switch21 = zeros(freq_num, 2, length(f_sweep));
curr_switch31 = zeros(freq_num, 2, length(f_sweep));
curr_switch12 = zeros(freq_num, 2, length(f_sweep));
curr_switch22 = zeros(freq_num, 2, length(f_sweep));
curr_switch32 = zeros(freq_num, 2, length(f_sweep));
%the first column: initial current with modulation
%the second column: final current with modulation
%assignment of the first column, Eq. (5.35)
curr_port1(index_shift,1,:) = interp1(Net.f_MHz, Net.PI, f_sweep);
curr_port2(index_shift,1,:) = interp1(Net.f_MHz, Net.PIJ, f_sweep);
curr_port3(index_shift,1,:) = curr_port2(index_shift,1,:);
curr_switch11(index_shift,1,:) = curr_port1(index_shift,1,:)/2;
curr_switch21(index_shift,1,:) = curr_port2(index_shift,1,:)/2;
curr_switch31(index_shift,1,:) = curr_port2(index_shift,1,:)/2;
curr_switch12(index_shift,1,:) = curr_port1(index_shift,1,:)/2;
```

```
curr_switch22(index_shift,1,:) = curr_port2(index_shift,1,:)/2;
curr_switch32(index_shift,1,:) = curr_port2(index_shift,1,:)/2;
%calculation of the final current
for r = 1:length(f_sweep) %loop for different frequency
    QI1_submatrix = diag(QI1_matrix(:,r));
    QIJ1_submatrix = diag(QIJ1_matrix(:,r));
    QI2_submatrix = diag(QI2_matrix(:,r));
    QIJ2_submatrix = diag(QIJ2_matrix(:,r));
    Ys_submatrix = diag(ys_matrix(:,r));
    QI_submatrix = [QI1_submatrix,  QI2_submatrix;
                    QI2_submatrix,  QI1_submatrix];
    QIJ_submatrix = [QIJ1_submatrix,  QIJ2_submatrix;
                     QIJ2_submatrix,  QIJ1_submatrix];
    Fd_MATRIX = [QI_submatrix,  QIJ_submatrix, QIJ_submatrix;
                 QIJ_submatrix, QI_submatrix,  QIJ_submatrix;
                 QIJ_submatrix, QIJ_submatrix, QI_submatrix];
    Yd_MATRIX = zeros(6*freq_num);
    for count = 1:6
        Yd_MATRIX((1:freq_num)+(count-1)*freq_num,(1:freq_num)+(count-
            1)*freq_num) = Yd_submatrix;
    end
    F_star = zeros(3*freq_num, 6*freq_num);
    Q_MATRIX_EYE = eye(6*freq_num) + Fd_MATRIX;
    F_star(1:freq_num,:) = Q_MATRIX_EYE(1:freq_num,:) +
            Q_MATRIX_EYE((1:freq_num)+freq_num,:);
    F_star((1:freq_num)+freq_num,:) =
            Q_MATRIX_EYE((1:freq_num)+2*freq_num,:) +
            Q_MATRIX_EYE((1:freq_num)+3*freq_num,:);
    F_star((1:freq_num)+2*freq_num,:) =
            Q_MATRIX_EYE((1:freq_num)+4*freq_num,:) +
            Q_MATRIX_EYE((1:freq_num)+5*freq_num,:);
    YCY_MATRIX = (Yd_MATRIX*C_MATRIX)/Yd_MATRIX;
    %Eq. (5.36)
    A_matrix = eye(size(Fd_MATRIX)) - Fd_MATRIX*YCY_MATRIX;
    b_vector = [curr_switch11(:,1,r);
                curr_switch12(:,1,r);
                curr_switch21(:,1,r);
                curr_switch22(:,1,r);
                curr_switch31(:,1,r);
                curr_switch32(:,1,r)];
    Xd_vector = A_matrix\b_vector;
    curr_switch11(:,2,r) = Xd_vector(1:freq_num);
    curr_switch12(:,2,r) = Xd_vector(freq_num+1:2*freq_num);
    curr_switch21(:,2,r) = Xd_vector(2*freq_num+1:3*freq_num);
    curr_switch22(:,2,r) = Xd_vector(3*freq_num+1:4*freq_num);
    curr_switch31(:,2,r) = Xd_vector(4*freq_num+1:5*freq_num);
    curr_switch32(:,2,r) = Xd_vector(5*freq_num+1:6*freq_num);
    p_vector = [curr_port1(:,1,r);
                curr_port2(:,1,r);
                curr_port3(:,1,r)];
    Xp_vector = p_vector + F_star*YCY_MATRIX*Xd_vector;
    curr_port1(:,2,r) = Xp_vector(1:freq_num);
    curr_port2(:,2,r) = Xp_vector(freq_num+1:2*freq_num);
    curr_port3(:,2,r) = Xp_vector(2*freq_num+1:3*freq_num);
end

Ip1 = reshape(curr_port1(index_shift,2,:),1,[]);
Ip2 = reshape(curr_port2(index_shift,2,:),1,[]);
Ip3 = reshape(curr_port3(index_shift,2,:),1,[]);

%calculation of S-parameters
S11 = 1-2*Ip1*Z0;
S21 = -2*Ip2*Z0;
S31 = -2*Ip3*Z0;
```

REFERENCES

[1] P. Gautam, S. Kaur, R. Kaur, S. Kaur, and H. Kundra, "Review Paper on 4G Wireless Technology."

[2] G. Singh and S. Kumar, "A Review Study on 4g Technologies," *International Journal of Software and Computer Science Engineering,* vol. 1, 2017.

[3] E. A. Klumperink and B. Nauta, "Software defined radio receivers exploiting noise cancelling: a tutorial review," *IEEE communications magazine,* vol. 52, pp. 111-117, 2014.

[4] A. A. Abidi, "The path to the software-defined radio receiver," *IEEE Journal of Solid-State Circuits,* vol. 42, pp. 954-966, 2007.

[5] T. Ulversoy, "Software defined radio: Challenges and opportunities," *IEEE Communications Surveys & Tutorials,* vol. 12, pp. 531-550, 2010.

[6] M. Calabrese, "The End of Spectrum 'Scarcity': Building on the TV Bands Database to Access Unused Public Airwaves," *New America Foundation June,* 2009.

[7] P.-I. Mak, S.-P. U, and R. P. Martins, "Transceiver architecture selection–review, state-of-the-art survey and case study," *Analog-Baseband Architectures And Circuits For Multistandard And Lowvoltage Wireless Transceivers,* pp. 9-40, 2007.

[8] B. Razavi and R. Behzad, *RF microelectronics* vol. 1: Prentice Hall New Jersey, 1998.

[9] (2017). *Cisco Visual Networking Index: Global Mobile Data Traffic Forecast Update, 2016–2021 White Paper*. Available: https://www.cisco.com/c/en/us/solutions/collateral/service-provider/visual-networking-index-vni/mobile-white-paper-c11-520862.html

[10] G. R. Maccartney, T. S. Rappaport, S. Sun, and S. Deng, "Indoor office wideband millimeter-wave propagation measurements and channel models at 28 and 73 GHz for ultra-dense 5G wireless networks," *IEEE Access,* vol. 3, pp. 2388-2424, 2015.

[11] T. S. Rappaport, S. Sun, R. Mayzus, H. Zhao, Y. Azar, K. Wang, *et al.*, "Millimeter wave mobile communications for 5G cellular: It will work!," *IEEE access,* vol. 1, pp. 335-349, 2013.

[12] S. Rangan, T. S. Rappaport, and E. Erkip, "Millimeter-wave cellular wireless networks: Potentials and challenges," *Proceedings of the IEEE,* vol. 102, pp. 366-385, 2014.

[13] N. Al-Falahy and O. Y. Alani, "Technologies for 5G networks: challenges and opportunities," *IT Professional,* vol. 19, pp. 12-20, 2017.

[14] A. Sabharwal, P. Schniter, D. Guo, D. W. Bliss, S. Rangarajan, and R. Wichman, "In-band full-duplex wireless: Challenges and opportunities," *IEEE Journal on Selected Areas in Communications,* vol. 32, pp. 1637-1652, 2014.

[15] D. Bharadia, E. McMilin, and S. Katti, "Full duplex radios," *ACM SIGCOMM Computer Communication Review,* vol. 43, pp. 375-386, 2013.

[16] M. José, R. Castro-López, A. Morgado, E. C. Becerra-Alvarez, R. del Río, F. V. Fernández, *et al.*, "Adaptive CMOS analog circuits for 4G mobile terminals—Review and state-of-the-art survey," *Microelectronics Journal,* vol. 40, pp. 156-176, 2009.

[17] R. Ruby, "A snapshot in time: the future in filters for cell phones," *IEEE Microwave Magazine,* vol. 16, pp. 46-59, 2015.

[18] R. H. O. III, "Microresonator Filters and Frequency Reference," 2011.

[19] J. Van Beek and R. Puers, "A review of MEMS oscillators for frequency reference and timing applications," *Journal of Micromechanics and Microengineering,* vol. 22, p. 013001, 2011.

[20] C. T.-C. Nguyen, "MEMS technology for timing and frequency control," *IEEE transactions on ultrasonics, ferroelectrics, and frequency control,* vol. 54, 2007.

[21] R. Abdolvand, B. Bahreyni, J. E.-Y. Lee, and F. Nabki, "Micromachined resonators: A review," *Micromachines*, vol. 7, p. 160, 2016.

[22] M. Lutz, A. Partridge, P. Gupta, N. Buchan, E. Klaassen, J. McDonald, *et al.*, "MEMS oscillators for high volume commercial applications," in *Solid-State Sensors, Actuators and Microsystems Conference, 2007. TRANSDUCERS 2007. International*, 2007, pp. 49-52.

[23] *SiTime Products Overview*. Available: https://www.sitime.com/products/products-overview-mems-oscillators

[24] S. Trolier-McKinstry and P. Muralt, "Thin film piezoelectrics for MEMS," *Journal of Electroceramics*, vol. 12, pp. 7-17, 2004.

[25] R. Ruby, "11E-2 Review and comparison of bulk acoustic wave FBAR, SMR Technology," in *Ultrasonics Symposium, 2007. IEEE*, 2007, pp. 1029-1040.

[26] *BROADCOM FBAR DEVICES*. Available: https://www.broadcom.com/products/wireless/fbar/

[27] R. C. Ruby, P. D. Bradley, and J. D. Larson III, "Method of mass loading of thin film bulk acoustic resonators (FBAR) for creating resonators of different frequencies and apparatus embodying the method," ed: Google Patents, 2002.

[28] G. Piazza, P. J. Stephanou, and A. P. Pisano, "Piezoelectric aluminum nitride vibrating contour-mode MEMS resonators," *Journal of Microelectromechanical Systems*, vol. 15, pp. 1406-1418, 2006.

[29] G. Piazza, P. J. Stephanou, and A. P. Pisano, "One and two port piezoelectric higher order contour-mode MEMS resonators for mechanical signal processing," *Solid-State Electronics*, vol. 51, pp. 1596-1608, 2007.

[30] M. Rinaldi, C. Zuniga, C. Zuo, and G. Piazza, "Super-high-frequency two-port AlN contour-mode resonators for RF applications," *IEEE transactions on ultrasonics, ferroelectrics, and frequency control*, vol. 57, 2010.

[31] M. Rinaldi, C. Zuniga, and G. Piazza, "5-10 GHz AlN contour-mode nanoelectromechanical resonators," in *Micro Electro Mechanical Systems, 2009. MEMS 2009. IEEE 22nd International Conference on*, 2009, pp. 916-919.

[32] J.-Q. Liu, H.-B. Fang, Z.-Y. Xu, X.-H. Mao, X.-C. Shen, D. Chen, *et al.*, "A MEMS-based piezoelectric power generator array for vibration energy harvesting," *Microelectronics Journal*, vol. 39, pp. 802-806, 2008.

[33] A. Konno, M. Sumisaka, A. Teshigahara, K. Kano, K.-y. Hashimo, H. Hirano, *et al.*, "ScAlN Lamb wave resonator in GHz range released by XeF 2 etching," in *Ultrasonics Symposium (IUS), 2013 IEEE International*, 2013, pp. 1378-1381.

[34] L. Colombo, A. Kochhar, C. Xu, G. Piazza, S. Mishin, and Y. Oshmyansky, "Investigation of 20% scandium-doped aluminum nitride films for MEMS laterally vibrating resonators," in *Ultrasonics Symposium (IUS), 2017 IEEE International*, 2017, pp. 1-4.

[35] Y. Xie, S.-S. Li, Y.-W. Lin, Z. Ren, and C. T.-C. Nguyen, "1.52-GHz micromechanical extensional wine-glass mode ring resonators," *ieee transactions on ultrasonics, ferroelectrics, and frequency control*, vol. 55, pp. 890-907, 2008.

[36] S. Gevorgian, A. K. Tagantsev, and A. Vorobiev, "Dielectric, mechanical, and electromechanical properties of ferroelectrics and piezoelectrics," in *Tuneable Film Bulk Acoustic Wave Resonators*, ed: Springer, 2013, pp. 17-54.

[37] J. Zou, C.-M. Lin, Y.-Y. Chen, and A. P. Pisano, "Theoretical study of thermally stable SiO2/AlN/SiO2 Lamb wave resonators at high temperatures," *Journal of Applied Physics*, vol. 115, p. 094510, 2014.

[38] H. J. Kim, S. Wang, C. Xu, D. Laughlin, J. Zhu, and G. Piazza, "Piezoelectric/magnetostrictive MEMS resonant sensor array for in-plane multi-axis magnetic field detection," in *Micro Electro Mechanical Systems (MEMS), 2017 IEEE 30th International Conference on*, 2017, pp. 109-112.

[39] G. Piazza, "Contour-mode aluminum nitride piezoelectric MEMS resonators and filters," in *MEMS-based Circuits and Systems for Wireless Communication*, ed: Springer, 2013, pp. 29-54.

[40] J. Segovia-Fernandez, M. Cremonesi, C. Cassella, A. Frangi, and G. Piazza, "Anchor losses in AlN contour mode resonators," *Journal of microelectromechanical systems,* vol. 24, pp. 265-275, 2015.
[41] C. Cassella and G. Piazza, "AlN two-dimensional-mode resonators for ultra-high frequency applications," *IEEE Electron Device Letters,* vol. 36, pp. 1192-1194, 2015.
[42] J. Segovia-Fernandez, M. Cremonesi, C. Cassella, A. Frangi, and G. Piazza, "Experimental study on the impact of anchor losses on the quality factor of contour mode AlN resonators," in *Solid-State Sensors, Actuators and Microsystems (TRANSDUCERS & EUROSENSORS XXVII), 2013 Transducers & Eurosensors XXVII: The 17th International Conference on*, 2013, pp. 2473-2476.
[43] H. Yunhong, Z. Meng, H. Guowei, S. Chaowei, Z. Yongmei, and N. Jin, "A review: aluminum nitride MEMS contour-mode resonator," *Journal of Semiconductors,* vol. 37, p. 101001, 2016.
[44] D. A. Frickey, "Conversions between S, Z, Y, H, ABCD, and T parameters which are valid for complex source and load impedances," *IEEE Transactions on microwave theory and techniques,* vol. 42, pp. 205-211, 1994.
[45] J. D. Larson, P. D. Bradley, S. Wartenberg, and R. C. Ruby, "Modified Butterworth-Van Dyke circuit for FBAR resonators and automated measurement system," in *Ultrasonics Symposium, 2000 IEEE*, 2000, pp. 863-868.
[46] C. Zuo, N. Sinha, J. Van der Spiegel, and G. Piazza, "Multifrequency pierce oscillators based on piezoelectric AlN contour-mode MEMS technology," *Journal of Microelectromechanical Systems,* vol. 19, pp. 570-580, 2010.
[47] K. Lakin, G. Kline, and K. McCarron, "Thin film bulk acoustic wave filters for GPS," in *Ultrasonics Symposium, 1992. Proceedings., IEEE 1992*, 1992, pp. 471-476.
[48] G. Piazza, P. J. Stephanou, and A. P. Pisano, "Single-chip multiple-frequency ALN MEMS filters based on contour-mode piezoelectric resonators," *Journal of MicroElectroMechanical Systems,* vol. 16, pp. 319-328, 2007.
[49] K. M. Lakin, "Thin film resonators and filters," in *Ultrasonics Symposium, 1999. Proceedings. 1999 IEEE*, 1999, pp. 895-906.
[50] K. M. Lakin, "Thin film resonator technology," *IEEE transactions on ultrasonics, ferroelectrics, and frequency control,* vol. 52, pp. 707-716, 2005.
[51] T.-T. Yen, C.-M. Lin, M. A. Hopcroft, J. H. Kuypers, D. G. Senesky, and A. P. Pisano, "Synthesis of narrowband AlN Lamb wave ladder-type filters based on overhang adjustment," in *Ultrasonics Symposium (IUS), 2010 IEEE*, 2010, pp. 970-973.
[52] J. Zou, "High Quality Factor Lamb Wave Resonators," Research Report, University of California, Berkeley2014.
[53] C. Zuo, N. Sinha, and G. Piazza, "Very high frequency channel-select MEMS filters based on self-coupled piezoelectric AlN contour-mode resonators," *Sensors and Actuators A: Physical,* vol. 160, pp. 132-140, 2010.
[54] G. Bu, D. Ciplys, M. Shur, L. Schowalter, S. Schujman, and R. Gaska, "Temperature coefficient of SAW frequency in single crystal bulk AlN," *Electronics letters,* vol. 39, pp. 755-757, 2003.
[55] A. Tazzoli and G. Piazza, "UHF clocks based on ovenized AlN MEMS resonators," in *Frequency References, Power Management for SoC, and Smart Wireless Interfaces*, ed: Springer, 2014, pp. 71-81.
[56] M. Rinaldi, Y. Hui, C. Zuniga, A. Tazzoli, and G. Piazza, "High frequency AlN MEMS resonators with integrated nano hot plate for temperature controlled operation," in *Frequency Control Symposium (FCS), 2012 IEEE International*, 2012, pp. 1-5.
[57] A. K. Samarao and F. Ayazi, "Temperature compensation of silicon micromechanical resonators via degenerate doping," in *Electron Devices Meeting (IEDM), 2009 IEEE International*, 2009, pp. 1-4.
[58] A. K. Samarao and F. Ayazi, "Intrinsic temperature compensation of highly resistive high-Q silicon microresonators via charge carrier depletion," in *Frequency Control Symposium (FCS), 2010 IEEE International*, 2010, pp. 334-339.

[59] R. Melamud, M. Hopcroft, C. Jha, B. Kim, S. Chandorkar, R. Candler, *et al.*, "Effects of stress on the temperature coefficient of frequency in double clamped resonators," in *Solid-State Sensors, Actuators and Microsystems, 2005. Digest of Technical Papers. TRANSDUCERS'05. The 13th International Conference on*, 2005, pp. 392-395.
[60] R. Melamud, B. Kim, M. A. Hopcroft, S. Chandorkar, M. Agarwal, C. Jha, *et al.*, "Composite flexural-mode resonator with controllable turnover temperature," in *Micro Electro Mechanical Systems, 2007. MEMS. IEEE 20th International Conference on*, 2007, pp. 199-202.
[61] R. Melamud, S. A. Chandorkar, B. Kim, H. K. Lee, J. C. Salvia, G. Bahl, *et al.*, "Temperature-insensitive composite micromechanical resonators," *Journal of Microelectromechanical Systems*, vol. 18, pp. 1409-1419, 2009.
[62] C.-M. Lin, T.-T. Yen, Y.-J. Lai, V. V. Felmetsger, M. A. Hopcroft, J. H. Kuypers, *et al.*, "Temperature-compensated aluminum nitride Lamb wave resonators," *IEEE transactions on ultrasonics, ferroelectrics, and frequency control*, vol. 57, 2010.
[63] S. Pourkamali, A. Hashimura, R. Abdolvand, G. K. Ho, A. Erbil, and F. Ayazi, "High-Q single crystal silicon HARPSS capacitive beam resonators with self-aligned sub-100-nm transduction gaps," *Journal of Microelectromechanical Systems*, vol. 12, pp. 487-496, 2003.
[64] C. T. Nguyen and R. T. Howe, "Microresonator frequency control and stabilization using an integrated micro oven," *Digest of Technical Papers*, pp. 1040-1043, 1993.
[65] C. M. Jha, M. A. Hopcroft, S. A. Chandorkar, J. C. Salvia, M. Agarwal, R. N. Candler, *et al.*, "Thermal isolation of encapsulated MEMS resonators," *Journal of Microelectromechanical Systems*, vol. 17, pp. 175-184, 2008.
[66] H. M. Lavasani, W. Pan, and F. Ayazi, "An electronically temperature-compensated 427MHz low phase-noise AlN-on-Si micromechanical reference oscillator," in *Radio Frequency Integrated Circuits Symposium (RFIC), 2010 IEEE*, 2010, pp. 329-332.
[67] H. M. Lavasani, W. Pan, B. P. Harrington, R. Abdolvand, and F. Ayazi, "Electronic temperature compensation of lateral bulk acoustic resonator reference oscillators using enhanced series tuning technique," *IEEE Journal of Solid-State Circuits*, vol. 47, pp. 1381-1393, 2012.
[68] F. Ayazi, R. Tabrizian, and L. Sorenson, "Compensation, tuning, and trimming of MEMS resonators," in *Frequency Control Symposium (FCS), 2012 IEEE International*, 2012, pp. 1-7.
[69] X. Wu, C. Zuo, M. Zhang, J. Van der Spiegel, and G. Piazza, "A 47μW 204MHz AlN Contour-Mode MEMS based tunable oscillator in 65nm CMOS," in *Circuits and Systems (ISCAS), 2013 IEEE International Symposium on*, 2013, pp. 1757-1760.
[70] B. Kim, M. A. Hopcroft, R. N. Candler, C. M. Jha, M. Agarwal, R. Melamud, *et al.*, "Temperature dependence of quality factor in MEMS resonators," *Journal of Microelectromechanical systems*, vol. 17, pp. 755-766, 2008.
[71] M. Hopcroft, M. Agarwal, K. Park, B. Kim, C. Jha, R. Candler, *et al.*, "Temperature compensation of a MEMS resonator using quality factor as a thermometer," in *Micro Electro Mechanical Systems, 2006. MEMS 2006 Istanbul. 19th IEEE International Conference on*, 2006, pp. 222-225.
[72] J. C. Salvia, R. Melamud, S. A. Chandorkar, S. F. Lord, and T. W. Kenny, "Real-time temperature compensation of MEMS oscillators using an integrated micro-oven and a phase-locked loop," *Journal of Microelectromechanical Systems*, vol. 19, pp. 192-201, 2010.
[73] A. Tazzoli, M. Rinaldi, and G. Piazza, "Ovenized high frequency oscillators based on aluminum nitride contour-mode MEMS resonators," in *Electron Devices Meeting (IEDM), 2011 IEEE International*, 2011, pp. 20.2. 1-20.2. 4.
[74] B. Kim, J. Nguyen, K. E. Wojciechowski, and R. H. Olsson, "Oven-based thermally tunable aluminum nitride microresonators," *Journal of microelectromechanical systems*, vol. 22, pp. 265-275, 2013.

[75] M.-H. Li, C.-Y. Chen, C.-S. Li, C.-H. Chin, and S.-S. Li, "A monolithic CMOS-MEMS oscillator based on an ultra-low-power ovenized micromechanical resonator," *Journal of Microelectromechanical Systems,* vol. 24, pp. 360-372, 2015.
[76] K. E. Wojciechowski, M. S. Baker, P. J. Clews, and R. H. Olsson, "A fully integrated oven controlled microelectromechanical oscillator—Part I: Design and fabrication," *Journal of Microelectromechanical Systems,* vol. 24, pp. 1782-1794, 2015.
[77] Z. Wu, A. Peczalski, and M. Rais-Zadeh, "Low-power ovenization of fused silica resonators for temperature-stable oscillators," in *Frequency Control Symposium (FCS), 2014 IEEE International*, 2014, pp. 1-5.
[78] C. Xu, J. Segovia-Fernandez, H. J. Kim, and G. Piazza, "Temperature-Stable Piezoelectric MEMS Resonators Using Integrated Ovens and Simple Resistive Feedback Circuits," *Journal of Microelectromechanical Systems,* vol. 26, pp. 187-195, 2017.
[79] A. Tazzoli, G. Piazza, and M. Rinaldi, "Ultra-high-frequency temperature-compensated oscillators based on ovenized AlN contour-mode MEMS resonators," in *Frequency Control Symposium (FCS), 2012 IEEE International*, 2012, pp. 1-5.
[80] Z. Wu and M. Rais-Zadeh, "A temperature-stable MEMS oscillator on an ovenized micro-platform using a PLL-based heater control system," in *Micro Electro Mechanical Systems (MEMS), 2015 28th IEEE International Conference on*, 2015, pp. 793-796.
[81] A. Tazzoli, N.-K. Kuo, M. Rinaldi, H. Pak, D. Fry, D. Bail*, et al.*, "A 586 MHz microcontroller compensated MEMS oscillator based on ovenized aluminum nitride contour-mode resonators," in *Ultrasonics Symposium (IUS), 2012 IEEE International*, 2012, pp. 1055-1058.
[82] B. Kim, R. H. Olsson, and K. E. Wojciechowski, "Ovenized and thermally tunable aluminum nitride microresonators," in *Ultrasonics Symposium (IUS), 2010 IEEE*, 2010, pp. 974-978.
[83] S. Gong and G. Piazza, "Monolithic multi-frequency wideband RF filters using two-port laterally vibrating lithium niobate MEMS resonators," *Journal of Microelectromechanical Systems,* vol. 23, pp. 1188-1197, 2014.
[84] K. E. Wojciechowski and R. H. Olsson, "A fully integrated oven controlled microelectromechanical oscillator—part II: characterization and measurement," *Journal of Microelectromechanical Systems,* vol. 24, pp. 1795-1802, 2015.
[85] C. Xu, E. Calayir, G. Piazza, M. Li, and S. Zhao, "Fast and accurate prediction of spurious modes in aluminum nitride MEMS resonators using artificial neural network algorithm," in *Ultrasonics Symposium (IUS), 2017 IEEE International*, 2017, pp. 1-4.
[86] T. M. Mitchell, "Machine learning. WCB," ed: McGraw-Hill Boston, MA:, 1997.
[87] *Bayesian regularization backpropagation - MATLAB trainbr - MathWorks*. Available: https://www.mathworks.com/help/nnet/ref/trainbr.htm
[88] C. Cassella, J. Segovia-Fernandez, G. Piazza, M. Cremonesi, and A. Frangi, "Reduction of anchor losses by etched slots in aluminum nitride contour mode resonators," in *European Frequency and Time Forum & International Frequency Control Symposium (EFTF/IFC), 2013 Joint*, 2013, pp. 926-929.
[89] C. Cassella, N. Singh, B. W. Soon, and G. Piazza, "Quality factor dependence on the inactive regions in AlN contour-mode resonators," *Journal of Microelectromechanical Systems,* vol. 24, pp. 1575-1582, 2015.
[90] J. Zou, C.-M. Lin, and A. P. Pisano, "Quality factor enhancement in Lamb wave resonators utilizing butterfly-shaped AlN plates," in *Ultrasonics Symposium (IUS), 2014 IEEE International*, 2014, pp. 81-84.
[91] C.-M. Lin, J.-C. Hsu, D. G. Senesky, and A. P. Pisano, "Anchor loss reduction in AlN Lamb wave resonators using phononic crystal strip tethers," in *Frequency Control Symposium (FCS), 2014 IEEE International*, 2014, pp. 1-5.
[92] J. Segovia-Fernandez, C. Xu, C. Cassella, and G. Piazza, "An alternative technique to Perfectly Matched Layers to model anchor losses in MEMS resonators with undercut suspensions," in *Solid-State Sensors, Actuators and Microsystems (TRANSDUCERS), 2015 Transducers-2015 18th International Conference on*, 2015, pp. 985-988.

[93] J. Segovia-Fernandez and G. Piazza, "Damping in 1 GHz laterally-vibrating composite piezoelectric resonators," in *Micro Electro Mechanical Systems (MEMS), 2015 28th IEEE International Conference on*, 2015, pp. 1000-1003.
[94] H. M. Lavasani, A. K. Samarao, G. Casinovi, and F. Ayazi, "A 145MHz low phase-noise capacitive silicon micromechanical oscillator," in *Electron Devices Meeting, 2008. IEDM 2008. IEEE International*, 2008, pp. 1-4.
[95] R. Abdolvand, H. M. Lavasani, G. K. Ho, and F. Ayazi, "Thin-film piezoelectric-on-silicon resonators for high-frequency reference oscillator applications," *IEEE transactions on ultrasonics, ferroelectrics, and frequency control*, vol. 55, pp. 2596-2606, 2008.
[96] S. Lee and C.-C. Nguyen, "Mechanically-coupled micromechanical resonator arrays for improved phase noise," in *Frequency Control Symposium and Exposition, 2004. Proceedings of the 2004 IEEE International*, 2004, pp. 144-150.
[97] C. D. Nordquist and R. H. Olsson, "Radio frequency microelectromechanical systems (RF MEMS)," *Wiley Encyclopedia of Electrical and Electronics Engineering*, 2014.
[98] D. Stuart-Watson, "A simple force feedback accelerometer based on a tuning fork displacement sensor," Ph. D. dissertation, University of Cape Town, South Africa, 2006.
[99] C. D. Ezekwe, *Readout techniques for High-Q micromachined vibratory rate gyroscopes*: University of California, Berkeley, 2007.
[100] Y. Liu, X. Liu, Y. Wang, and W. Chen, "A sigma–delta interface ASIC for force-feedback micromachined capacitive accelerometer," *Analog Integrated Circuits and Signal Processing*, vol. 72, pp. 27-35, 2012.
[101] A. Norouzpour-Shirazi, M. Hodjat-Shamami, R. Tabrizian, and F. Ayazi, "Dynamic tuning of MEMS resonators via electromechanical feedback," *IEEE transactions on ultrasonics, ferroelectrics, and frequency control*, vol. 62, pp. 129-137, 2015.
[102] M. Field and C. Chen, "Surface Acoustic Wave Regenerative Active Resonator," in *Ultrasonics Symposium, 1977*, 1977, pp. 909-912.
[103] Y. Dong, M. Kraft, C. Gollasch, and W. Redman-White, "A high-performance accelerometer with a fifth-order sigma–delta modulator," *Journal of micromechanics and microengineering*, vol. 15, p. S22, 2005.
[104] J. Raman, E. Cretu, P. Rombouts, and L. Weyten, "A closed-loop digitally controlled MEMS gyroscope with unconstrained sigma-delta force-feedback," *IEEE Sensors journal*, vol. 9, pp. 297-305, 2009.
[105] E. D. McCloskey, "Q-Enhanced LC Resonators for Monolithic, Low-Loss Filters in Gallium Arsenide Technology," 2001.
[106] T. Kodera, D. L. Sounas, and C. Caloz, "Magnetless nonreciprocal metamaterial (MNM) technology: application to microwave components," *IEEE Transactions on Microwave Theory and Techniques*, vol. 61, pp. 1030-1042, 2013.
[107] N. A. Estep, D. L. Sounas, J. Soric, and A. Alù, "Magnetic-free non-reciprocity and isolation based on parametrically modulated coupled-resonator loops," *Nature Physics*, vol. 10, pp. 923-927, 2014.
[108] N. Reiskarimian and H. Krishnaswamy, "Magnetic-free non-reciprocity based on staggered commutation," *Nature communications*, vol. 7, 2016.
[109] R. Fleury, D. L. Sounas, and A. Alù, "Subwavelength ultrasonic circulator based on spatiotemporal modulation," *Physical Review B*, vol. 91, p. 174306, 2015.
[110] A. Kord, D. L. Sounas, and A. Alù, "Pseudo-Linear-Time-Invariant Magnet-less Circulators Based on Differential Spatio-Temporal Modulation of Resonant Junctions," *arXiv preprint arXiv:1709.08133*, 2017.
[111] *Simulation and Analysis Guide: Chapter 6. Harmonic Balance Analysis*. Available: https://awrcorp.com/download/faq/english/docs/simulation/hb_analysis.html
[112] A. Patterson, E. Calayir, G. K. Fedder, G. Piazza, B. W. Soon, and N. Singh, "Application of statistical element selection to 3D integrated AlN MEMS filters for performance correction and yield enhancement," in *Micro Electro Mechanical Systems (MEMS), 2015 28th IEEE International Conference on*, 2015, pp. 996-999.
[113] E. Calayir, "Heterogeneous Integration of AlN MEMS Contour-Mode Resonators and CMOS Circuits," 2017.

[114] C. D. Nordquist and R. H. Olsson, "Power handling and intermodulation distortion of contour-mode AlN MEMS resonators and filters," in *Microwave Symposium Digest (MTT), 2011 IEEE MTT-S International*, 2011, pp. 1-4.

[115] C. Xu, J. Segovia-Fernandez, and G. Piazza, "Sub-milliwatt integrated oven for temperature stable laterally vibrating piezoelectric MEMS resonators," in *Solid-State Sensors, Actuators and Microsystems (TRANSDUCERS), 2015 Transducers-2015 18th International Conference on*, 2015, pp. 977-980.

[116] C. Xu and G. Piazza, "Artificial neural network based digital temperature compensation method for aluminum nitride MEMS resonators," in *Ultrasonics Symposium (IUS), 2017 IEEE International*, 2017, pp. 1-4.

[117] C. Xu, E. Calayir, and G. Piazza, “Magnetic-Free Electrical Circulator Based On AlN MEMS Filters and CMOS RF Switches,” in *Micro Electro Mechanical Systems (MEMS), 2018 IEEE 31th International Conference on*, 2018, pp. 755-758.